Surface Modification and Electronic Structure Characterisation of Carbon-based and Iron-based Materials

Di Hu

Department of Physics

Aberystwyth University

This dissertation is submitted for the degree of

Doctor of Philosophy

January 2017

PRIFYSGOL ABERYSTWYTH UNIVERSITY

Mandatory Layout of Declaration/Statements

Word Count of thesis: DECLARATION	31318
This work has not previously been accepted in substance for any degree and is not concurrently submitted in candidature for any degree.	
Candidate name	Di Hu
Signature:	胡迪 Di Hu
Date	2017. 08. 18

STATEMENT 1

This thesis is the result of my own investigations, except where otherwise stated. Where ***correction services** have been used, the extent and nature of the correction is clearly marked in a footnote(s).

Other sources are acknowledged by footnotes giving explicit references. A bibliography is appended.

Signature:	胡迪 Di Hu
Date	2017. 08. 18

[*this refers to the extent to which the text has been corrected by others]

STATEMENT 2

I hereby give consent for my thesis, if accepted, to be available for photocopying and for inter-library loan, and for the title and summary to be made available to outside organisations.

Signature:	胡迪 Di Hu
Date	2017. 08. 18

NB: *Candidates on whose behalf a bar on access (hard copy) has been approved by the University should use the following version of Statement 2:*

I hereby give consent for my thesis, if accepted, to be available for photocopying and for inter-library loans after expiry of a bar on access approved by Aberystwyth University.

Signature:	
Date	

This thesis is dedicated

to my grandparents, Shuying and Jun, my parents, Lihui and Wenfu,

for their unconditional support and love.

ACKNOWLEDGEMENTS

I would like to take this opportunity to express my sincere acknowledgement to all the amazing people that I met during the last 4 years. The first is my supervisor Professor Andrew Evans, who took me into my PhD research field and gave me lots of invaluable discussions on my project. I must also thank to my second supervisor Professor Zhongfu Zhou, who offered me this PhD opportunity and brought me to a broader stage.

Dr Simon Cooil, as my mentor and elder brother, are to be acknowledged for the helping during my whole PhD study. I would never forget the long days and nights we have worked at each part around Europe, also the entertaining and insightful talks about science, music and life.

Meanwhile the technicians and other staffs, Mr Les Dean and Mr David Lewis of the electronic workshop, Dr David Langstaff, Dr Rachel Cross, Dr Matthew Gun, my research wouldn't be accomplished without the unselfish help from you. In addition, all my colleagues and collaborators, Professor Chun Feng, Dr Wenlin Chen, Dr Morgan Jones, Mr Nathan Davies, Mr Benjamin Reed, who made my study more enjoyable and animated. I would like to appreciate all of you.

Lastly, I would thank to all my friends I've met in Aberystwyth, Dr Pan Su, Mr Tianhua Chen, Mr Simon Masuch, Miss Alessia Lacedelli and so many names from Aberystwyth Man Basketball Club, especially our coach Dr Jan Ruzicka and our chairman Mr Qiuming Hu. Each and every of you have played such an important part in my life and made this town as the second home of mine.

ABSTRACT

This thesis provides an important basis for understanding the surface modulation mechanism and electronic structure variation on semiconducting surfaces and metallic thin films. The use of real-time photoelectron spectroscopy (REES) makes it possible to monitor the solid surfaces during *in situ* processing. The surfaces that have been investigated were (100) facet boron-doped diamond surfaces and iron thin films. The surface processing treatments include annealing, thin film coating and exposure to oxygen and hydrogen microwave plasma sources.

The oxygen-terminated (100) facet diamond was annealed up to 1000℃ while monitoring with REES. The oxygen desorption process on the surface can be divided into four distinct stages according the oxygen concentration on the diamond (100) surface during the heating cycle. The ratio of ketone/ether groups has been investigated. Moreover, the true band bending on O-terminated (100) has been investigated with real-time characterization, which has a maximum difference of +1.0 eV comparing with the room temperature XPS spectra data.

Fluorouracil (5-FU), as a drug widely used in leukaemia and bowel cancer treatment, which is demonstrated to degrade on silver coated catheter surfaces, producing hydrofluoric acid and therefor leading to adverse effects on patients. In order to compare diamond as coating material, the adsorption of 5-FU on the oxygen and hydrogen terminated diamond (100) surfaces has been studied with x-ray photoelectron spectroscopy (XPS), showing extremely different behaviours.

Utilising the shape memory alloy (SMA) substrate, the continuously mediated strain was transferred from the substrate to Fe films through a thermally controlled shape memory effect. The pure strain modulated electronic structure in the Fe thin films was studied using *in situ* XPS and first-principle calculations. The result demonstrates that the compressive strain increases the overlap of outer orbits and enhances the shielding effect to core electrons, resulting in significant tunability on the binding energy of core electrons and related magnetic anisotropy.

PUBLICATIONS

Feng, C., **Hu, D.**, Gong, K., Jiang, X., Yin, J., Cao, Y., Tang X., Yang F., Zhou Z., Yu G., Andrew Evans, D. *Thickness-dependent electronic structure modulation of ferromagnetic films on shape memory alloy substrates based on a pure strain effect.* Applied Physics Letters, 109(21), 212401.

Feng, C.; Zhao, J.; Yang, F.; Hao, S.; Gong, K.; **Hu, D.**; Cao, Y.; Jiang, X.; Wang, Z.; Chen, L.; Li, S.; Sun, L.; Cui, L.; Yu, G., *Reversible and Nonvolatile Modulations of Magnetization Switching Characteristic and Domain Configuration in L10-FePt Films via Nonelectrically Controlled Strain Engineering*. ACS Applied Materials & Interfaces **2016**, 8 (11), 7545-7552.

Cooil, S. P.; Wells, J. W.; **Hu, D.**; Niu, Y. R.; Zakharov, A. A.; Bianchi, M.; Evans, D. A., *Controlling the growth of epitaxial graphene on metalized diamond (111) surface*. Applied Physics Letters **2015,** *107* (18), 181603.

CONTENTS

CHAPTER 1 – INTRODUCTION

1.1 Introduction

Surface science, as a multi-field research of materials, physics and chemistry, has gained more attention from materials scientist worldwide during the past few decades. It has evolved from the characterisation of surface chemical composition, to the modulation of the atomic structure and to the synthetic production of low-dimensional composite materials[1-3]. Its wide applicability has significant influence both on scientific research and industrial application.

Surface science is dependent on making sure the sample characteristics do not change between experiments and measurement, due to adsorbates. As such, surface scientists require extremely clean environments and specialised techniques in which to conduct their experiments. As a consequence of all these constraints, the development of relevant technologies has played a great role in promoting the research of this field, such as ultra-high vacuum (UHV), the magnetic transfer arm, in-vacuum heating stage and so on[4]. These technologies help material engineers to improve thin film materials or surfaces by special surface processing, which include annealing the material, doping of semiconductors, alloying of metals, reaction of surface with ionised gas molecules or depositing of thin film overlayers. More advanced methods include performing the treatment *in situ*, without exposure to the ambient pressure, and even measuring the

surface in real-time during the surface processing.

The phenomenon of photoemission was firstly discovered by Hertz in 1887[5]. The German physicist, Albert Einstein, successfully explained this experiment by invoking the quantum nature of light and was awarded with the Nobel prize for establishing the theory of photoelectric effect[6]. This eventually led to the first photoelectron spectroscopy (PES) system which was developed in the late 1960s[7]. Since that time PES has become a powerful tool for measuring the chemical composition and evolving the electronic structure of clean surfaces and interfaces for a long time.

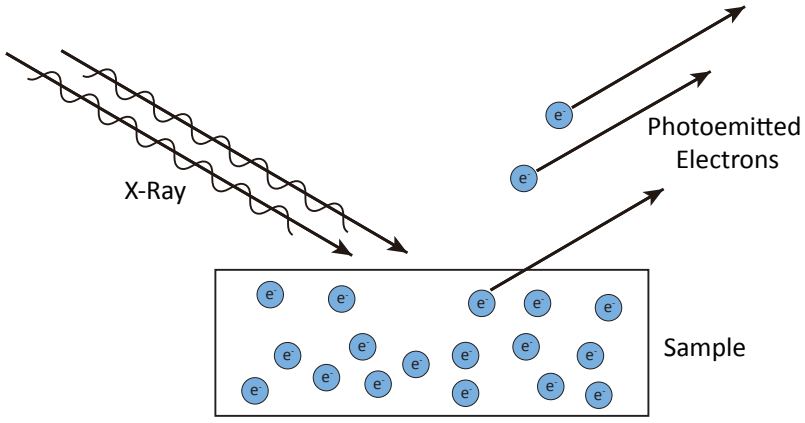

Figure 1.1 Schematic of photoelectric effect: photons (curve lines) bombard on the metal surface and electrons are excited (moving with the straight lines).

Like the majority of surface sensitive techniques, XPS can involve long measurement times, during which the surface needs to remain unchanged and fixed. However, the recent improvements in position sensitive electron detectors has allowed the implementation of real-time measurement on the materials during *in situ* surface

processing[8-10].

Here at Aberystwyth University, a custom made multi-channel electron detector was applied on the photoelectron spectroscopy system by Langstaff and Evans which enables monitoring of a surface with XPS in the sub-second regime. It has been increased from 198 channels to a staggering 1526 channel detector (currently being characterised) since it was built[11-13]. Combined with the *in situ* surface processing techniques of the system, its application in real-time has led to further understanding on the electronic properties of carbon-base materials, especially diamond surfaces. Real-time measurements were performed on different facet diamond samples with treatments such as temperature annealing cycles, contacts with metal interfaces and epitaxial graphene growth[14-16].

Diamond research has successfully drawn the attention of materials scientists worldwide for the past sixty-five years. The superior hardness, chemical stability and thermodynamic properties are all well understood. However advances in perfecting the growth of synthetic diamond have seen a renewed interest in the material as a semiconducting substrate for electronic applications [17] and as a coating for biomedical implants [18]. In this work, surface composition and electronic structure variations of O-terminated diamond (100) surface have been investigated with high temperature annealing at 1000℃. The experimental data indicates the initial and final

temperature of oxygen desorption. The surface band bending on the O-terminated semiconducting diamond surface was shifted by around 1eV during the heating process. Furthermore, the transition of the surface structure from a C(100)-(1×1):O surface to a C(100)-(2×1):H surface has been demonstrated.

Fluorouracil (5-FU) is a widely used drug in the treatment of conditions such as leukemia and bowel cancer. It is usually delivered through catheters that are often coated with anti-bacterial films such as silver. The interaction between the molecule and the catheter surface is not normally considered, but it has been recently shown by x-ray photoelectron spectroscopy (XPS) that a silver surface can catalyse the dissociation of the 5-FU molecule to release HF, while the carbon-based surfaces are normally chemically inert. Therefore, in order to compare diamond as coating material, the adsorption of 5-FU on the oxygen and hydrogen terminated diamond (100) surfaces has been studied. The result shows 5-FU attaches to the O-terminated diamond (100) and silver surfaces but not to the H-terminated diamond (100) surface, which could be a surface termination effect with diamond and related to the surface properties, such as chemical bond, electron affinity and dipole moment, of the diamond surface.

Another important part in this thesis is the project about pure-strain effect on the thickness-dependent iron thin film. In this experiment, the non-electronically controlled NiTi(Nb) shape memory alloy was utilized as the strain output substrate for Fe

ferromagnetic films, where the continuously mediated strain was transferred from the substrate to the Fe film. Based on the structure, the pure strain modulated electronic structure in the Fe thin films was studied with real-time photoelectron spectroscopy. The result demonstrates that the compressive strain increases the overlap of outer orbits and enhances the shielding effect to core electrons, resulting in significant tunability of the binding energy of core electrons. Meanwhile, the lattice strain modifies the density of state and spin distribution of outer *d* orbits, leading to the evolutions of bandwidth, spin-orbit coupling strength, and related magnetic anisotropy.

1.2 Layout of Thesis and Contribution

All figures, tables, diagrams, images and data are the work of the author unless stated. Following this introduction, the techniques and instrumentation will be introduced in chapter 2 and chapter 3, whilst the detail and discussion of the main experimental results will be presented in chapter 4-6, and finally chapter 7 summarises the main conclusion and introduces the further plans of this work.

Chapter 4 presents the data obtained with Real-time Electron Emission Spectroscopy (REES) system, combined with supporting AFM data and LEED data. All data in this chapter was obtained in the Materials Laboratory at Department of Physics,

Aberystwyth University.

Chapter 5 shows the data of 5-FU/diamond interfaces. Near edge x-ray absorption fine structure (NEXAFS) data was collected at D1011 beamline, MAX Lab, Lund University, Sweden, with assistance of Dr Simon Cooil.

Chapter 6 introduces the investigation of the pure strain effect on the ferromagnetic thin films. The Density Functional Theory (DFT) calculations were done by Dr Kui Gong, Center for the Physics of Materials and Department of Physics, McGill University. The magnetic measurements were performed at National Center for Nanoscience and Technolgy, China Academy of Sciences, with assistance of Mr Dongwei Wang.

CHAPTER 2 – TECHNIQUES

The essential theory of the techniques underpinning this work are presented in this chapter. The ultra-high vacuum created by the pumping system isolates the materials from ambient pressure, and ensures the processing and monitoring was completed on a "clean" surface. The *in situ* surface processing used for this work will also be discussed. Photoelectron spectroscopy (PES) is well acknowledged as one of the most revolutionary achievement in understanding the chemical constitution and electronic structure of materials. Combined with other techniques such as low energy electron diffraction and first principle calculations, it has become a routine method for scientists to investigate surface properties in material science.

2.1 Ultra-High Vacuum (UHV)

UHV is essential to create a clean environment for surface science investigations. It is a basic requirement for two reasons; to prepare and maintain a clean environment which allows for the desorption of contaminants and preservation of clean surfaces; and to increase the mean free path for the photo and low energy electrons. However, UHV only provides an environment with very low pressure instead of an absolute vacuum. This means the sample surface is able to remain contaminant free (or a low percentage of a monolayer coverage) for a certain period of time (usually the duration of the experiment).

Vacuum is measured in terms of the amount of material present in the form of residual gas molecules with a certain volume. According to Avogadro's law, equal volumes of all gases have the same number of molecules at the same temperature and pressure. This is shown by the ideal gas law as :

$$\rho = \frac{N}{V} = \frac{P}{k_B T}$$

(Eqn. 2.1.1)

where ρ is the gas density, N the number of gas molecules, V the volume, P the pressure, k_B the Boltzmann constant, and T the absolute temperature.

Pressure is measured in Pascals however the non-SI unit mbar is usually used for vacuum gauges where 100 Pa=1 mbar. By applying kinetic gas theory (where gas molecules are modelled as spheres of finite diameter within a finite volume), the necessity for vacuum can be demonstrated by considering the distances molecules can travel without colliding with each other and the number of molecules colliding with a surface per unit time. The flux of molecules to a surface determines the rate at which the sample surface would be completely covered. The rate at which gas molecules arrive at the surface can be given as:

$$\phi = \frac{1}{4} \rho c_a$$

(Eqn. 2.1.2)

where ϕ is the flux of molecules, c_a is the average velocity. The root mean squared

velocity can be related to the kinetic energy of the particles mass with respect to their thermodynamic temperature by,

$$\mathrm{c_{rms}}^2 = \frac{3k_B\mathrm{T}}{\mathrm{m}}$$

(Eqn. 2.1.3)

where m is mass of the molecule. The relation between two velocities, c_a and c_{rms}, is given by $c_a = (8/3\pi)^{1/2}c_{rms}$, therefore the flux of molecules colliding with a surface, known as the Hertz-Knudsen equation, is given by:

$$\phi = \frac{\mathrm{P}}{\sqrt{2\pi\mathrm{m}k_B\mathrm{T}}}$$

(*Eqn. 2.1.4*)

and has units of $n_{molecules}/m^2s^1$ as derived in *Ref.* [19].

The average distance between gas molecule collisions, or the mean free path is given as:

$$\mathrm{P}\bar{\lambda} = \frac{1}{\sqrt{2}\sigma}k_B\mathrm{T}$$

(Eqn. 2.1.5)

where $\bar{\lambda}$ is the mean free path and σ the collision cross-section. The mean free path provides an absolute minimum value for a given gas pressure for particles to travel from a sample to a measuring device without being scattered by the residual gas molecules. For typical distances of 1 m the required pressure would be less than 10^{-4} mbar.

The molecular flux on a surface can be used to estimate the time taken for a monolayer of residual gas to form on a surface,

$$t_{ML} = \frac{10^{19}}{\phi}$$

(Eqn. 2.1.6)

where t_{ML} is the formation time of a monolayer coverage contaminants and has a unit of s. From *Eqn. 2.1.4* and *Eqn. 2.1.6*, it shows for a pressure of 10^{-6} mbar, a monolayer of contamination would cover the surface in 1 s if all gas molecules stick to the surface (sticking coefficient of unity). Table 2.1 lists the properties of four vacuum regimes commonly encountered. For performing surface science experiments the ultra high vacuum regime is normally considered a minimum. At base pressure of 10^{-10} mbar a sample could expect to be free from residual contamination for 10^4 s, or approximately 3 hours, allowing ample time for measuring clean surfaces after preparation.

Vacuum Regime	**Pressure 10^x (mbar)**	**Molecule density 10^x (cm^{-3})**	**Mean free path 10^x (m)**	**ML time 10^x (s)**
Atmospheric	3	25	-8	-9
Low	1	22	-5	-6
Medium	-3	19	-2	-3
High	-6	16	2	1
Ultra-high	-10	12	5	4

Table 2.1 Pressure regimes with typical values for the particle density, mean free path and monolayer formation time.

2.2 Surface *In Situ* Processing

In experimental physics, *in situ* typically refers to a method of data collection or manipulation of a sample without exposure to an external environment. For example, real-time *in situ* XPS was used to study the thermal stability of the hydroxyl termination and downward band bending on the polar surfaces of ZnO single crystals[20]. In this work three methods of *in situ* processing were used, which include thin film deposition, active gas plasma and *in vacuo* annealing.

2.2.1 Thin Film Growth

Depositing one material onto another is a common surface processing method for the manufacture of integrated structures in a single device[21]. Normally the overlayer (material A) is evaporated from a molecular beam source onto the substrate (material B). The flux from the beam source, as given in *Eqn. 2.1.4*, provides a number of molecules per unit time that adsorb onto the surface of the substrate. The single molecules may remain at their adsorption site or diffuse along the surface, which is determined by the bonding strength between the molecules and the substrate, but they may also be lost from the surface through several mechanisms including re-evaporation, diffusion into the substrate and capture by other single molecules or by defects[22]. On the other hand, the properties of the thin films such as conductivity, thermodynamic and chemical reactivity vary with the film thickness. This made investigation on the thin films

materials as an important subject in material science.

In such cases, the dynamics of the single molecule beam determines the property of the thin film, in particular the growth mode of the film on the substrate. In 1958 Ernst Bauer identified the interaction and nucleation of materials deposited onto substrates in the literature and proposed three different modes for thin film growth as illustrated in Figure 2.1 [23]. The first situation is Frank-van der Merwe 'layer-by-layer' (Figure 2.1a) in which the material forms complete layers because of the strong bonding between the molecules and the substrate. The second is Volmer-Weber 'island growth' (Figure 2.1b) in which no complete layers are formed instead the material clusters on the substrate due to weak bonding between the molecules and the substrate. Finally, the third is the Stranski-Krastanov growth mode in which layer-by-layer growth proceeds for a few monolayers at the interface followed by cluster growth (Figure 2.1c).

The formation of the thin film growth mode is determined predominately by the difference in surface energies of the materials, where the surface energy of the substrate is given as Υ_B, the overlayer as Υ_A and the interface as Υ^* [22]. Volmer-Weber growth occurs if the surface energy of the overlayer and interface are less than that of the substrate (given by *Eqn 2.2.1*). Layer by layer growth occurs if the combined energies are larger than that of the substrate (given by *Eqn. 2.2.2*). However, Stranski-Krastanov growth is the transition from layered growth to island growth, which

is due to the interface energy increasing as the number of layers increases during the growth. This could be influenced by factors such as strain and molecular orientation of the overlayer.

$$\Upsilon_B > \Upsilon_A + \Upsilon^*$$

(Eqn. 2.2.1)

$$\Upsilon_B < \Upsilon_A + \Upsilon^*$$

(Eqn. 2.2.2)

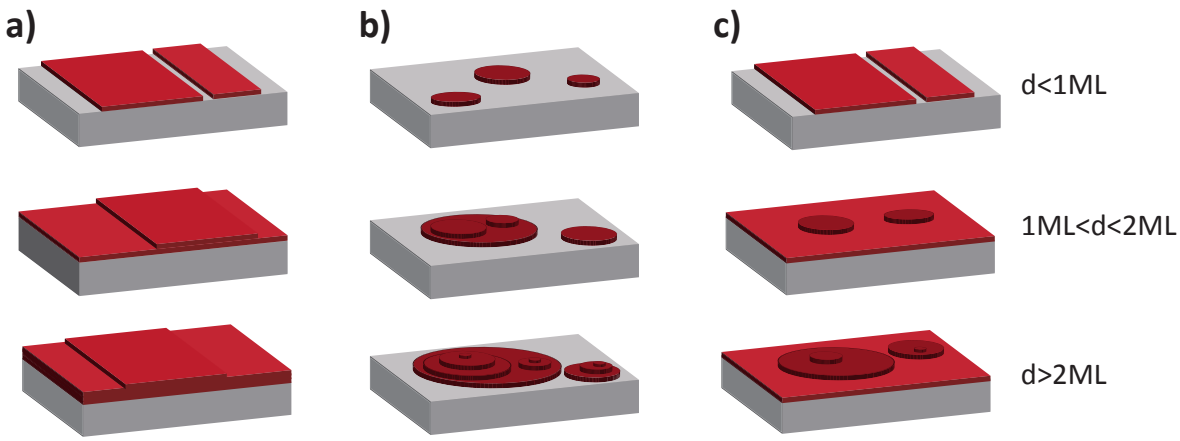

Figure 2.1 The three different thin film growth modes identified by E. Bauer: Frank-van der Merwe (a) Volmer-Webber (b) and Stranksi-Krastanov (c), where 'd' is the thickness of the thin film.

2.2.2 Surface Termination with Plasma Source

Plasma source treatment with different gas species is able to modify and terminate the surface of substrates with selected functional groups, which have been shown to have interesting effects on the electronic structure, surface dipole and conductivity of the

interface[3, 24]. For example on the diamond surface, the oxygen-terminated surface has a positive electron affinity whilst the hydrogen-terminated surface has a unique negative electron affinity[25]. For surface termination of surfaces with specific ad-atoms, chemically active ionised atoms are usually preferred. Low pressure ground state gases are normally too un-reactive, however, exposure to ionised gases is much more reactive due to the presence of atomic and excited species.

Processing with ionised gases has been used extensively in both research and application. Examples in the literature include hydrogen [26, 27], oxygen [28, 29] and fluorine[30, 31]. There is also the entire field of Chemical Vapour Deposition (CVD) of materials [32, 33]. The advantage of performing gaseous processing *in situ* is that it produces an ultra-clean surfaces with ad-atoms.

In this case, a method of promoting molecules into their excited states and forming active species is therefore required, and one way of achieving this is with low-pressure, non-thermal plasma sources. Plasma is a state of matter composed of ions and free electrons. Plasma sources are categorised into two primary types: thermal or non-thermal sources depending on the energies (temperature) of the ions. In thermal plasmas, the ions have energies equivalent to several thousand degrees Kelvin while in non-thermal plasmas the ions have negligible energies. For both types the free electrons have high energies. The two most common cases of electron recombination in

non-thermal plasma are radiative and dissociative recombination[34]. In radiative recombination an energetic electron e^- is captured by an ion X^+, to produce a neutral excited species X^*, given by *Eqn. 2.2.3*. While in dissociative recombination a diatomic ion XY^+ is dissociated into its two constituent atoms, X and Y, by the capture of an energetic electron e^-, given by *Eqn. 2.2.4*. Plasmas therefore contain excited and dissociated species.

$$X^+ + e^- \rightarrow X^*$$

(Eqn. 2.2.3)

$$XY^+ + e^- \rightarrow X + Y$$

(Eqn. 2.2.4)

2.3 Photoelectron Spectroscopy

In the late 1960s, K. Seigbahn from Uppsala University developed the first system which was based on the photoelectric effect for measuring the subshell electron binding energy of a material accurately[35, 36]. From that time, PES has become one of the most powerful and revolutionary techniques to determine orbital ionisation energies, chemical composition, compound stoichiometry, work function, overlayer thickness and morphology. The conventional PES techniques are normally classified into two types, x-ray photoelectron spectroscopy (XPS) and ultraviolet photoelectron spectroscopy (UPS), depending on the incident photon source used for measurement.

2.3.1 The Principles of PES

In order to determine the electronic energy levels of the material, PES obtains a spectrum by measuring the kinetic energy of photoelectrons escaping from a material due to the photoelectric effect. Several theoretical models have been presented for interpreting the photoemission process; these are discussed at length in S. Hüfner's work[37, 38]. One of the earliest descriptions of the measured photoemission intensity is given in Berglund and Spicer's early work[39]. The classic three-step model makes the photoemission process quite comprehensible, separating the process involved in the initial excitation and movement of the excited electron to the surface of the material as follows:

Step 1. The electron is excited into a higher state through absorbing the energy of the incident photons.

Step 2. The electron travels through the crystal to the surface/vacuum interface.

Step 3. The electron escapes from the material and into vacuum.

The three steps of photoemission process are illustrated in Figure 2.2, where core level binding energy can be considered as the total energy of the atom before and after absorption. A ground state neutral atom in an initial state and has a total energy equal to the initial state energy $E_{initial}$ (shown as Figure 2.3a). After absorption of a photon, the total energy of the atom increases as the summation of initial state energy plus the photon energy, $E_{initial}$ +hv. Following the emission of a photoelectron (which carries away

energy as kinetic energy, E_k), the atom is ionised into the final state with a total energy known as the final state energy, E_{final}. The total energy of the ion and the photoelectron may be written as $E_{final}+E_k$, and equals the total energy before emission. The binding energy of the core level electron is described as the amount of energy that is required to be given to the electron to pull it away from this attractive (Coulombic) force. In this situation, it is then understood as being the difference between the initial and final state energies. The electron binding energy is determined as the energetic difference between the photon source and the kinetic energy of the photoelectron. This expression may be written as:

$$E_b = E_{final} - E_{initial} = h\nu - E_k$$

(Eqn. 2.3.1)

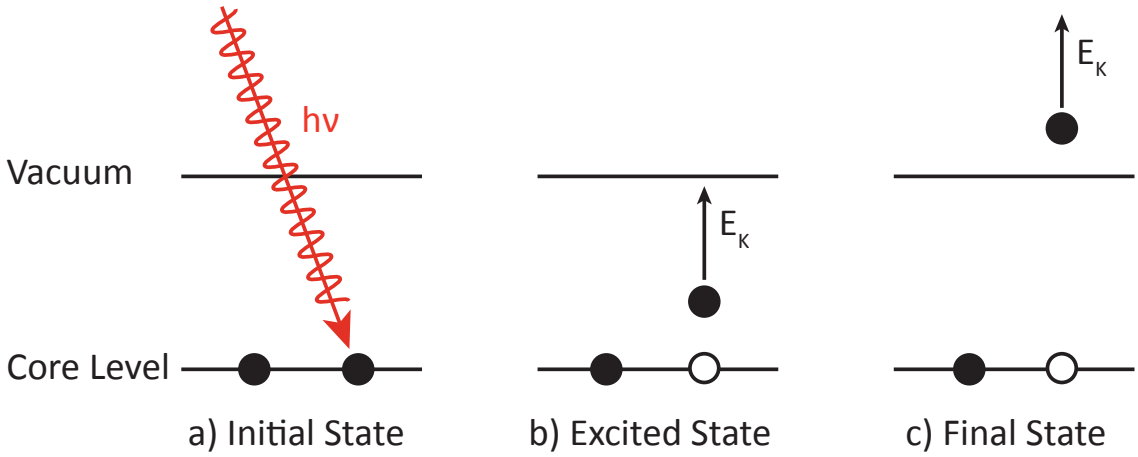

Figure 2.2 The photoemission process with in three steps; a) neutral atom with photon adsorption; b) excited neutral atom after photon adsorption; c) ionised atom and the photoelectron.

Photoelectrons may be emitted from open electron shells (valence electrons) or from closed electron shells (core-level electrons). Core-levels appear in a photoelectron spectrum as discrete lines the position and intensity of which are of interest. The lines exhibit an energy shift, known as a chemical shift, which is related to the chemical environment of the atom, giving additional lines at higher and lower energy to the main line.

The photon-excited electrons normally have a mean-free path length of a few nanometers within the materials, however if the photoelectrons escape into vacuum they are able to travel with enormous distances in comparison. This allows hemispherical electron analysers (HSA) that have large internal path lengths (typically in the region of 1-2 m) to be used for dispersing the electrons according to kinetic energy, as a requirement of imaging the emitted electrons with high energy resolution.

However in practical applications, the sample work function and analyser work function need to be taken into account as shown in *Eqn. 2.3.1*. Figure 2.3 shows the energy alignment between the material and electron analyser, which including a material with a core level, Fermi level E_F and vacuum level E_{VAC} and a spectrometer with a Fermi level E_F and vacuum level E_{VAC} in electrical contact with the sample. In this case, considering the work function of the material ϕ_M, *Eqn. 2.3.1* is derived as *Eqn. 2.3.2.*

$$E_k = h\nu - E_b - \phi_M$$

(Eqn. 2.3.2)

As the Fermi level is aligned between the sample material and analyser, the work function of analyser ϕ_A and a contact potential $\phi_{M-}\phi_A$ exist between the sample and analyser, shown as *Eqn. 2.3.3*. Combining *Eqn. 2.3.2* and *Eqn. 2.3.3,* an expression for the measured binding energy of the core level can be written as *Eqn 2.3.4*, which is independent of the material work function. By measuring the kinetic energy of the photoelectrons reaching the analyser E_k', the core-level binding energies may be directly measured.

$$E_k' - E_k = \phi_M - \phi_A$$

(Eqn. 2.3.3)

$$E_b = h\nu - E_k' - \phi_A$$

(Eqn. 2.3.4)

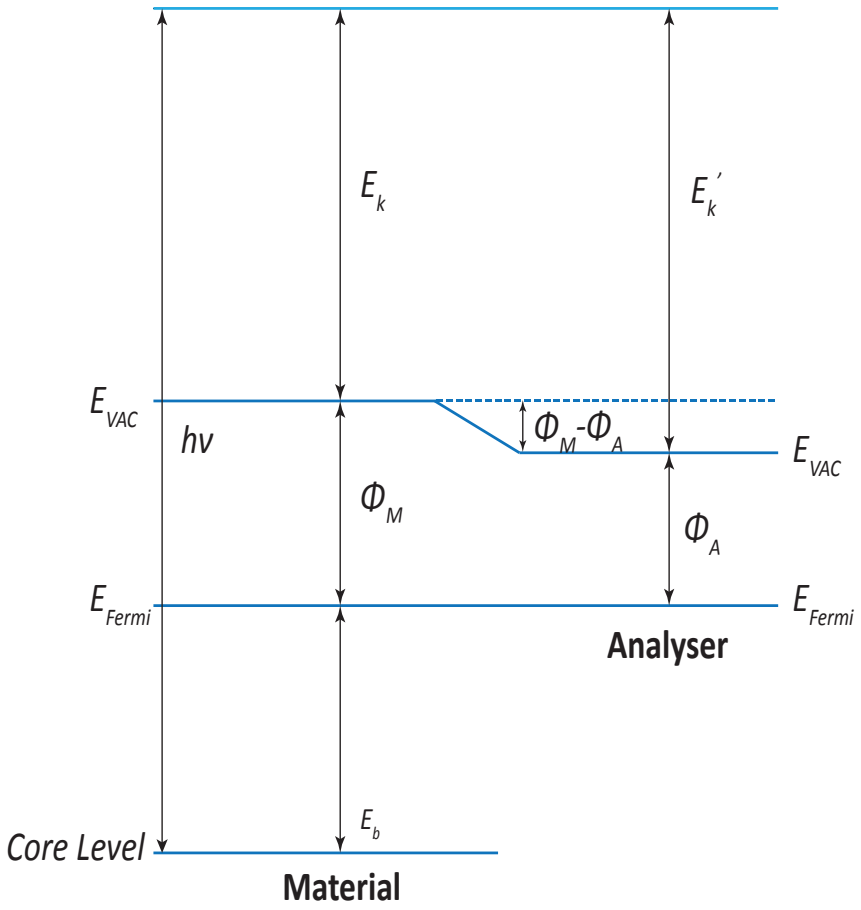

Figure 2.3 Energy level alignment between a material and electron analyser. The material has a work function ϕ_M and a core level in a sample has a binding energy of E_b relative to the Fermi level. The analyser has a work function of Φ_A. A photon of energy *hv* has removed an electron from the core level into the vacuum where is has a kinetic energy E_k in the sample and E_k' in the spectrometer.

2.3.2 Auger Effect

After the primary photoemission process, the ion (with a core-hole) is energetically unstable. In this situation the ion will re-equilibrate the materials electronic structure through either x-ray fluorescence or through the Auger emission. Fluorescence is simply the filling of a core-hole with an electron from a higher energy shell with the emission of

a photon. In the Auger emission, an electron from a higher shell fills the core-hole and releases energy by the emission of a second electron from the same or higher shell, illustrated as in Figure 2.4. The ejected electron is known as an Auger electron and its kinetic energy is given by,

$$E_{kin} = E_{1s} - E_{2s} - E_{2p}$$

(Eqn. 2.3.5)

where E_{kin} is the kinetic energy, E_{1s} the binding energy of 1s shell (core-hole level), E_{2s} the binding energy of 2s shell (transiting electron level), and E_{2p} the binding energy of 2p shell (the Auger electron level). The distinguishing feature of the Auger emission process is that the emitted electrons have constant kinetic energy, which is independent of the incident photon energy.

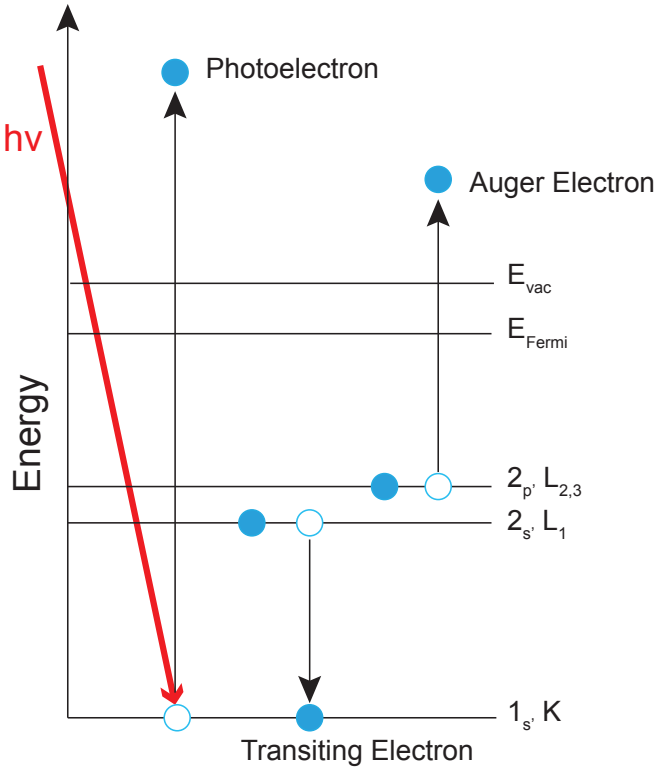

Figure 2.4 Schematic diagram of KLL Auger emission process.

When labeling Auger electrons the convention is to use x-ray notation; first noting the core-hole level, then noting the transiting electron level, and last noting the Auger level. For example, the Auger process in Figure 2.4 should be labeled as $KL_1L_{2,3}$ which refers to a transition where a core-hole was created in the K shell, an electron from the L_1 shell filled the core-hole, and an Auger electron was emitted from the $L_{2,3}$ shell. Coster-Kronig transitions are observed when the Auger electron is emitted from a sub-shell that has the same principal quantum number as the core-hole. (such as $L_1L_{2,3}M_1$ transitions) [40]. The photon emission and Auger emission are competitive processes and the Auger yield is dependent on the atomic number; Auger emission preferentially occurs in the lighter element atoms while photon emission mostly occurs on the heavier elements.

2.3.3 Spin-orbit Splitting, Plasmon and Satellite Peaks

The photoemission process is a multi-electron system. Therefore excitation of the core level electrons must result in the re-equilibration of electronic configuration due to the Coulombic interaction. The interaction of the excited electrons with the electronic structure gives rise to further peaks, these include; plasmon peaks, satellite peaks and spin orbit splitting (shown in Figure 2.5).

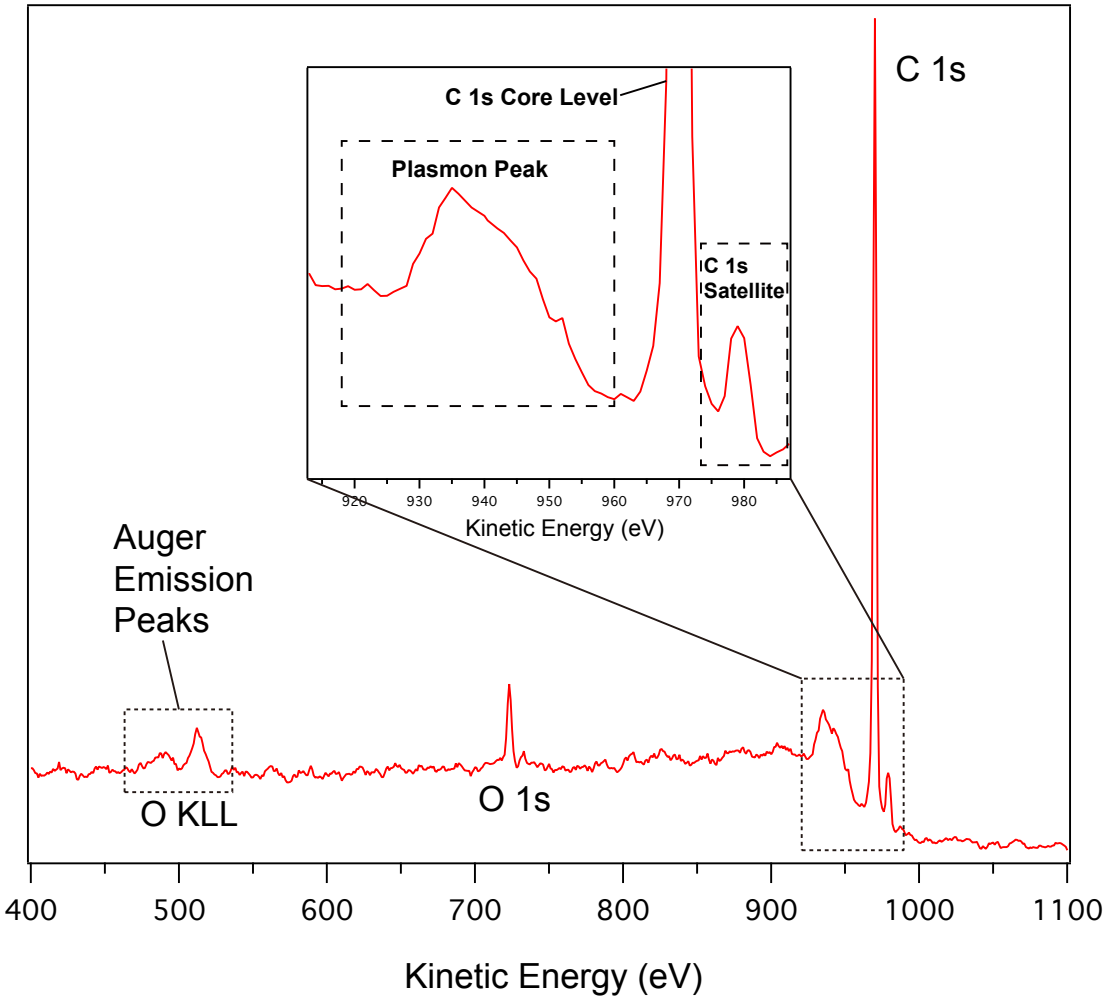

Figure 2.5 A PES widescan of an Oxygen-terminated (100) single crystal diamond taken with a *Mg Ka* photon Source. Core level peak (C 1s, O 1s), Auger emission peaks (O KLL), plasmon and satellite peaks are labelled in the spectrum.

Plasmon peaks are formed due to quantised oscillations in the valence electrons in semiconductors or free electrons in metals. Intrinsic and extrinsic effects lead to these peaks as follows; the intrinsic effect is a consequence of the coupling between the positive core-hole (formed during the photoemission process) and the oscillations of the valence states[41, 42]. The photoelectron is excited with less energy since this process happens simultaneously with the PES process. The frequency ω_p of these oscillations is

different within the bulk than at the surface of the material. The emitted photoelectron will therefore be detected with an energy loss corresponding with the energies of $\hbar\omega_{pb}$ or $\hbar\omega_{ps}$ (or multiples for the higher harmonics) for the bulk and surface plasmon respectively. Extrinsic effects relate to the coupling of the electric field of the excited photoelectron with the valence (free) electrons as it reaches to the material surface [42]. As before the electron loses energy relating to $\hbar\omega_{pb}$ or $\hbar\omega_{ps}$ (or multiples) for the bulk plasmon and surface plasmon respectively, however the process dislocated the initial photoemission site. For example, diamond the bulk and surface plasmon peaks usually arise at 34-36 eV from the main C 1s peak.

Satellite peaks are generated by the non-monochromatic nature of x-ray generation in lab sources. Usually an aluminium window is used to purify the x-ray radiations for magnesium anode, however small amounts of non-preferential x-rays still make it through and generate their own photoelectrons. However the intensity of these satellite peaks is weak in comparison to the main spectral features generated by the main x-ray source. In a photoelectron spectrum the satellite peaks can be removed by the software during the data analysis process. Otherwise by measuring with a monochromatic x-rays radiation source, such as with the synchrotron radiation, the satellite peaks are removed completely.

Spin-orbit splitting is a consequence of the interaction between the spin magnetic dipole moment, s, and the orbital angular momentum, l, of the electron orbiting within the atom. The result is a splitting of the electronic state where the total angular momentum is given by

$$j = |l \pm s| \ \ where\ s = \frac{1}{2}$$

(Eqn. 2.3.6)

For light elements (only having s-orbital electrons) the orbital angular momentum is zero and the orbital remains as a single peak. However, for large atomic number atoms (such as transition metals), the p, d and f orbitals have non-zero orbital angular momentum, and the total angular momentum has more than one value, e.g. for the 2p orbital, $j =$ 1/2 or 3/2 which will give rise to two peaks in the photoelectron spectrum. The number of electrons which contribute to the degeneracy of the energy level is given by $2j + 1$ and the intensity of the core level peak will broadly be proportional to the number of electrons present in that energy level. The relative intensity of the spin-orbit split peaks is called the branching ratio, R and is dependent on the value of l, given as:

$$R = \frac{2j_+ + 1}{2j_- + 1}$$

(Eqn. 2.3.7)

where j_+ and j_- correspond to the angular momentum determined by the positive or negative addition of the spin moment of electron respectively as shown in *Eqn. 2.3.6.*

Subshell	j values	Area Ratio
s	1/2	N/A
P	1/2 3/2	1:2
d	3/2 5/2	2:3
f	5/2 7/2	3:4

Table 2.2 Spin-orbit splitting j values and respective area ration for s, p, d, f orbitals.

2.3.4 Electron Attenuation Length

Normally the lower kinetic energy end of the photoelectron spectrum would have additional intensity. This is due to photoelectrons with low energy scattered when travelling in the crystal. The electron attenuation length (EAL), is a characteristic length defined as the point where the probability of scattering drops by e^{-1} [38]. The EAL value, typically on the order of nanometers, is dependent on the photoelectron energy and on the properties of the material.

The intensity of a photoelectron spectrum is defined as a function of the depth from the surface to where it was generated. For the normal emission, the function is given by:

$$I = I_0 e^{(\frac{-d}{\lambda})}$$

(Eqn. 2.3.8)

where *I* is the measured intensity, I_0 the intensity for an infinitely thick sample, d the depth and λ the EAL. From *Eqn. 2.3.8* the analysis depth of XPS may be evaluated; 65% of the photoelectron intensity will originate within λ of the surface, 85% from < 2λ, and 95% from < 3λ [7]. 3λ is therefore considered the standard analysis depth for photoelectron spectroscopy and is also in the nanometer range, resulting in high surface sensitivity.

From *Eqn. 2.3.8*, calculation of the EAL is usually determined by the 'overlayer method', in which the intensity of the substrate core-level is measured on the clean surface and attenuated on the surface with a known thickness overlayer. In addition, by collecting experimental data and calculating EALs values across a range of kinetic energy values, a database of EALs for a variety materials has been built, and makes the use of XPS for quantitative analysis[43].

2.3.5 Peak Shift and Line Shape

The peak profile of the photoelectron spectrum can be as informative as the recorded peak intensity and position. One of the most useful advantages of PES is its ability to distinguish the difference between the chemical species of a single element present on the material surface through the analysis of its peak profile. The peak profile is a convolution of the incident photon line shape and contributions from the material such as, the core-hole lifetime and broadening due to atomic vibrations. When multiple

species of the same element are presented on the sample surface, multiple peaks will be observed with small shifts between each other, which are of the order of the experimental resolution, and result in a change in the peak lineshapes. In this case, a peak fitting profile can be employed; the Voigt function line shape is often chosen to fit the photoelectron peak profile of semiconductor material, whilst the Doniach-Sunjic lineshape is usually used for fitting the peak profile of metallic materials.

The Voigt function is a convolution of Gaussian and Lorentzian components and depends on a number of factors, including excitation source (e.g. Kα x-rays have a Lorentzian nature and synchrotron radiation through an undulator having a Gaussian profile), and the intrinsic core-hole lifetime (which is assumed to be Lorentzian in nature) [7]. Some debate has been established in order to determine whether a sum of the two peak-shapes, or the product of each matches the lineshape of a Voigt function [44].

The Doniach-Sunjic (DS) lineshape is a Gaussian-Lorentzian peak with a modified tail on the higher binding energy side of the peak [45, 46], as a consequence of the attenuation of the photoelectrons' energy travelling through the materials. This profile is commonly used for photoelectrons that originate within the atoms of a metallic layer. However the rich density of states at the Fermi-level for some metals (low-Z metals do not show this) means that the electron must travel through this large 'Fermi-sea'

and therefore the photoelectron loses energy due to Coulombic interaction, depending on the core-hole lifetime. The result is an asymmetry in the photoelectron peak where the DS lineshape takes into consideration the many possibilities for energy loss and provides a suitable fit for peak profiles.

2.3.6 Photoionisation Cross-Section

The core level peaks in the photoelectron spectrum are due to the elemental composition of the sample, and the intensity of the peaks can be used to analyse the components quantitatively. An important parameter for the quantification of a XPS spectrum is the photoionisation cross-section σ. It is defined as the number of electrons excited per unit time divided by the number of incident photons per unit time per unit area. It is dependent on the photon energy and is the total probability of all individual ionisation of each orbital in the material. The transition probability per unit time from an initial state to a final state can be calculated using Fermi's Golden Rule, which is expressed as*:*

$$P_{if} = \frac{2\pi}{\hbar} \left| M_{if} \right|^2 \rho_f(E)$$

(Eqn. 2.3.9)

where M_{if} is the matrix element for the interaction and $\rho_f(E)$ is the density of final states. In this approach the cross-section is considered as the probability of transition per unit time from one eigenstate (initial energy state) in a quantum system into a

continuum of eigenstates (final state) which is expressed as a function of energy. The validity of this rule depends on the initial state not having been significantly depleted by transition of electron to final states. The Hamiltonian is the operator that corresponds to the total energy of the system and the electromagnetic wave (e.g. x-ray in XPS), it is considered as a time-dependent perturbing Hamiltonian which affects the quantum system. The matrix element for this interaction is derived from this Hamiltonian. Therefore, the matrix element represents the strength of the coupling between the initial and final state upon which the transition rate depends. In this situation, a strong coupling combined with a high density of final states will yield a high intensity photoelectron peak in the PES spectrum.

In order to obtain the correct result, it is critical that this factor is applied when measuring quantitative analysis of PES spectra. For the fixed photon sources the cross section values remain constant for each core level, but for tuneable sources (e.g. synchrotron radiation source) this value varies with the photon energies used. The cross section can be measured or calculated and values are widely available for standard sources, such as the *Mg Ka* x-ray source. Scofield's early work has provided a useful quantitative tool for analysis of XPS spectra by applying a relativistic Hartee-Slater model to calculate the absorption cross sections for most elements (Z= 1-92) at a number of incident photon energies[47, 48]. An additional consideration when calculating the elemental composition of a sample is the analyser transmission function.

This quantity is important since at different kinetic energies the efficiency of the analyser at transmitting electrons changes and can be experimentally determined from test sample data for each analyser. Therefore both these corrections must be applied to any spectra before quantification of the elemental composition.

2.3.7 Charging Effect

Since photoelectron spectroscopy is a charge-oriented technique, electrostatic charging effects may be observed on insulating or semiconducting samples. The insulating nature of the sample determines that no electrons can travel through the bulk to refill the core-hole as electrons are emitted from the surface. This results in the accumulation of a positive charge in the near surface region which increases the barrier encountered by the photo-excited electrons as they leave the surface. As a result, more energy is lost by the electrons as they are transmitted into the vacuum and they are hence observed to have a lower kinetic energy (or higher apparent binding energy) than expected, causing the photoelectron peak to shift. This problem can be fixed by supplying an Ohmic contact with ground to allow a flow of low energy electrons to the surface through photoemission. Samples with poor Ohmic contacts (rectifying contacts), low-doped semiconductors, and insulators, are prone to charging.

Surface photovoltage charging of semiconductors is a less common phenomenon. This

effect is due to the dissociation of electron-hole pairs in the semiconductor depletion region and the accumulation of either electrons or holes at the sample surface, with the reduction of surface band bending and an apparent flat band surface. For p-type semiconductors an accumulation of electrons at the surface gives rise to erroneously low binding energies being observed. For n-type semiconductors an accumulation of holes at the surface results in erroneously high binding energies being observed. The effect is proportional to both the number of electron-hole pairs that are dissociated, and also the number of photons irradiating the sample. High flux sources (synchrotron or flood x-ray sources) are therefore likely to produce this effect.

Several semiconductor systems have been reported to exhibit a surface photovoltage effect. Synchrotron radiation measurements of gallium phosphide [49], zinc selenide [50] and zinc sulphide [51], ultraviolet radiation measurements on silicon [52] and diamond [53], and nonmonochromatic *Mg Kα* measurements on gallium nitride [54] have all revealed surface photovoltage of up to 1.5 eV depending on the experimental conditions. Importantly silicon was shown to have a completely saturated photovoltage (flat bands) at 20 K with high UV flux or at 50 K with mild UV flux, revealing the maximum surface photovoltage shift is equal to the true barrier height. Similarly diamond was shown to have a small surface photovoltage at 300 K which increased rapidly with decreasing temperature, reaching 0.6 eV at 170 K.

2.3.8 Quantification

Photoelectron spectra enable the concentration of different atomic species present in a sample to be determined by fitting an appropriate lineshape due to the unique photoionization cross-section of energy levels. It has been discussed that the number of photoelectrons excited from a particular energy level in a single atom is dependent on the number of photons incident onto the atom and the photoionization cross-section of the energy level. For a homogeneous sample the number of photoelectrons excited is proportional to the number of atoms with an identical energy level. There is an additional dependency on the electron attenuation length and the transmission function of the analyser. Therefore for a sample consisting of a species i with a concentration N_i, the number of photoelectrons $\mathrm{I}(E_k, \mathrm{x})$, which is proportional to the peak intensity produced from an energy level x, is given by

$$\mathrm{I}(E_k, \mathrm{x}) = \mathrm{J}(\mathrm{h\upsilon}) \cdot N_i \cdot \sigma(\mathrm{h\nu}, \mathrm{x}) \cdot \mathrm{T}(E_k) \cdot \lambda(E_k)$$

(Eqn. 2.3.10)

where J is the photon flux, N_i the concentration of species i, σ the photoionization cross-section of energy level x, T the transmission function of the spectrometer, λ the electron attenuation length, E_k the kinetic energy of the photoelectrons, x the energy level of interest and $\mathrm{h\nu}$ the incident photon energy. Therefore, for a multi compound sample, the concentration of each element can be calculated with the single core level for each species (typically the most intense peak profile).

Moreover, the thickness of the overlayer can be calculated from the intensity of the substrate before and after deposition by deriving of *Eqn. 2.3.8*,

$$\frac{I}{I_0} = e^{(\frac{-x}{\lambda})}$$

(Eqn. 2.3.11)

where I is the intensity of the substrate core level, I_o is the intensity for the clean substrate, x is the thickness of the overlayer and λ the electron attenuation length. In addition, the overlayer thickness can also be calculated by measurement of the overlayer core level with,

$$I = I_\infty(1 - e^{\left(\frac{-x}{\lambda}\right)})$$

(Eqn. 2.3.12)

where I_∞ is the intensity of an infinitely thick overlayer which can be approximated to the intensity of the core level for a thickness which is much greater than the mean free path of the electron through the overlayer material.

2.4 Complementary Techniques

2.4.1 Low Energy Electron Diffraction

Low Energy Electron Diffraction (LEED) utilises the wave-like nature of electrons in order to probe the surface structure of materials. For low energy (non-relativistic) electrons，their wavelength can be determined by applying the de Broglie relation to the kinetic energy equation. For electrons with kinetic energies between 10-200 eV, their de Broglie

wavelength is in the order of 1-2 Å or less, which is similar to the typical interatomic spacing within crystalline lattices. Therefore diffraction can occur when electrons encounter an ordered lattice structure as the crystalline lattice acts as a grating for the incident electron beam. The electron attenuation length (which has been discussed in 2.3.4) determines that this technique is very surface sensitive and able to probe only the uppermost atomic layers of the solid with a depth of 3-4 Å. Electrons, which are first generated by thermionic emission, are accelerated towards the sample surface with a chosen kinetic energy chosen by an electron gun, illustrated in Figure 2.6. The interference pattern occurring as two electrons interact with each other due to a path difference D, after backscattering from adjacent lattice points on the surface at distance 'α' can be written as,

$$\mathrm{D} = \alpha \sin\theta$$

(*Eqn 2.4.1*)

where θ is the angle of incidence to the surface plane. The intensity of the backscattered beams dependents on the electron wavelength λ'. It varies as a function of θ and are at a maximum when the Bragg Condition is met. This occurs when the when the electron wavelength is equal to or an exact integer 'n' multiple of the path difference, given as

$$\mathrm{n}\lambda' = \alpha \sin\theta$$

(*Eqn 2.4.2*)

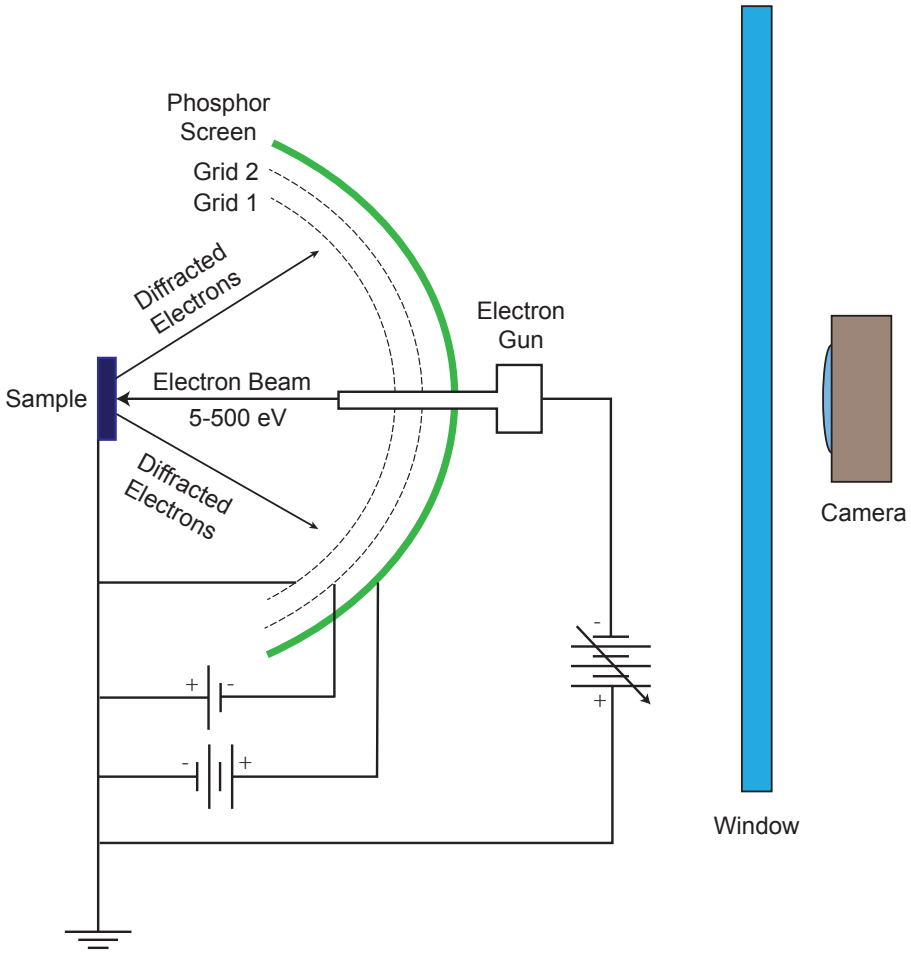

Figure 2.6 Schematic diagram of the experimental configuration of a rear-view low energy electron diffraction system.

Since a surface is 2D in nature, the crystal structure diffracts the electrons in two orthogonal directions. The interference of all the backscattered electrons from a large number of unit cells (the electron beam usually has a diameter with around 1mm diameter) then forms the diffraction pattern which maps reciprocally with the structure of the sample surface.

The backscattered electrons in a conventional rear-view LEED system are collected by a series of grids that filter the secondary electrons and accelerate the backscattered electrons towards a luminescing phosphor screen. Focus of the illumination source and variable bias contrast meshes are also used to image the diffraction pattern at the screen with the best possible contrast between diffracted spots and background intensity. Generally a high background intensity in the diffraction pattern refers to poor crystallinity of surface, since there will be a high percentage of other reflection angles from dislocations etc. As the wavelength of the incident electrons changes with kinetic energy so does the size of the reciprocal space pattern, and therefore the distance between spots.

2.4.2 Vibrating Sample Magnetometer

Vibrating Sample Magnetometry (VSM) is one of the most important methods for measuring the magnetism of a sample [55]. It allows magnetic parameters of the sample to be determined by observing the hysteresis loop with VSM measurement. As shown in Figure 2.3a, which is a schematic diagram of a VSM unit, the sample is placed in a magnetic field, which equals the magnetic dipole, and vibrates with constant amplitude in the homogenous magnetic field. Utilising the electron signal amplifier system, the induced voltage in the coil generated by the dipole field will be amplified. The magnetic moment can then be calculated by the relationship with the induce voltage of tested

samples. As shown in figure 2.3 (b), the direction of the applied magnetic field H is along with the x axis, the sample vibrates around the z axis, the coil is placed at position r with the number of turns N, the area of the coil as S. The induced voltage can be expressed as

$$\varepsilon(t) = -\frac{d\varphi}{dt} = -\frac{3M}{4\pi} a_0 \omega \cos(\omega t) K$$

(*Eqn 2.4.3*)

where M is the magnetic moment of the sample, a_0 is the amplitude of vibration, ω is the frequency of the vibration, K is a constant related to the size, shape, number of turns and position of the coil.

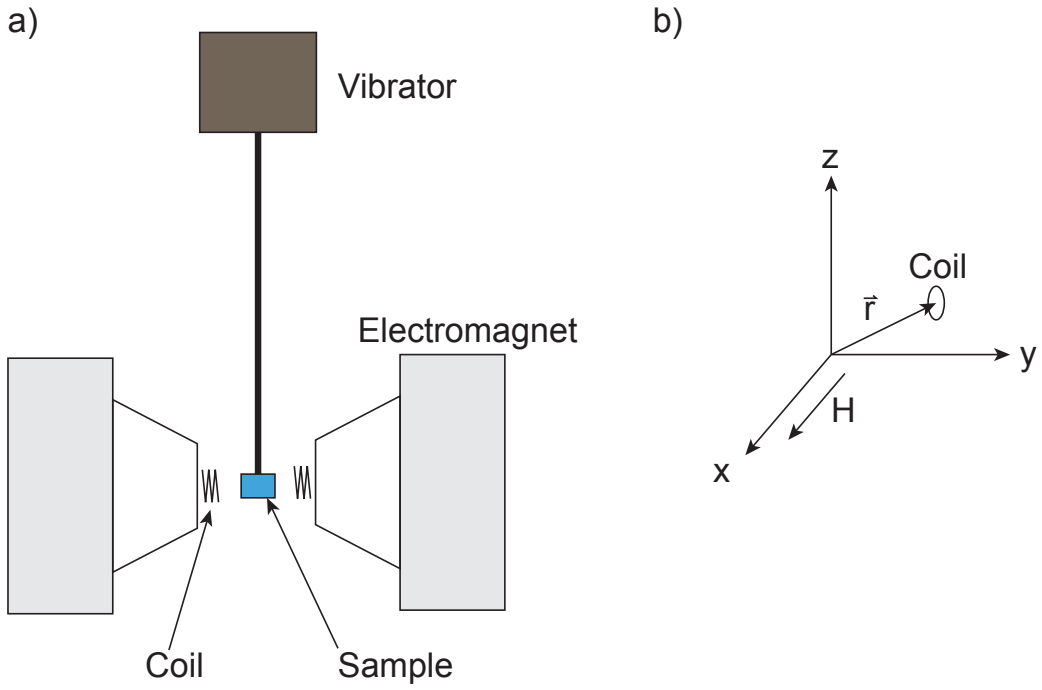

Figure 2.7 Schematic diagrams of (a) VSM system and (b) spatial relationship between the coil position and the magnetic field.

VSM units are the most common equipment on the Physical Property Measurement System (PPMS), which is designed for the comprehensive measurement of materials

under an environment with low temperature and strong magnetic field, such as direct current (DC) magnetization and alternating current (AC) magnetic susceptibility, DC resistance, AC transport properties, heat resistance and torque of magnetic susceptibility etc[56]. The instrument used for the work in this thesis was a PPMS with a VMS unit made by Quantum Design Ltd. PPMS is consistent with a base system and other optional units. According to the magnetism of internal superconducting devices the system is classified with 7 T, 9 T, 14 T and 16 T. With temperature and magnetic field provided by the fundamental system, it allows a variety of options for magnetic measurement, the electric transport measurement, thermal parameters and thermal transport measurements, whilst the AC unit and VSM unit are the most common optional units used with PPMS for magnetic measurement.

2.4.3 Atomic Force Microscopy

Atomic force microscopy (AFM), is a nanoscale high resolution scanning probe microscope. The resolution of AFM is 1000 times better than the optical diffraction limit. The first AFM was invented by Heinrich Rohrer and Gerd Binnig of the IBM Zurich Research Laboratory in the 1980s, based on scan tunnelling microscope. The instrument used for the work in this thesis was a Park XE-100 instrument with all samples measured *ex situ* under atmospheric conditions.

Figure 2.8 shows the configuration of AFM. The key component of AFM is a micro cantilever with a pointed probe on the head that scans the surface of the sample. The size of the cantilever is usually in the range of several tens to hundreds of microns and made of silicon or silicon nitride. The curvature radius of the probe tip is in the nanometer scale. When the probe is placed near the surface of the sample, the probe head on the cantilever will be deflected according to Hooke's law due to the atomic forces induced between the sample surface and the probe tip. In different cases, the force may be mechanical contact force, van der Waals force, chemical bond, orientation force, electrostatic force, magnetic force, solvent force, etc. The offset of the tip is detected by a laser beam incident on the topside of the micro-cantilever. The surface of the cantilever is often coated with a reflective material, such as aluminum, which reflects the laser beam into a position sensitive photodiode (PSPD).

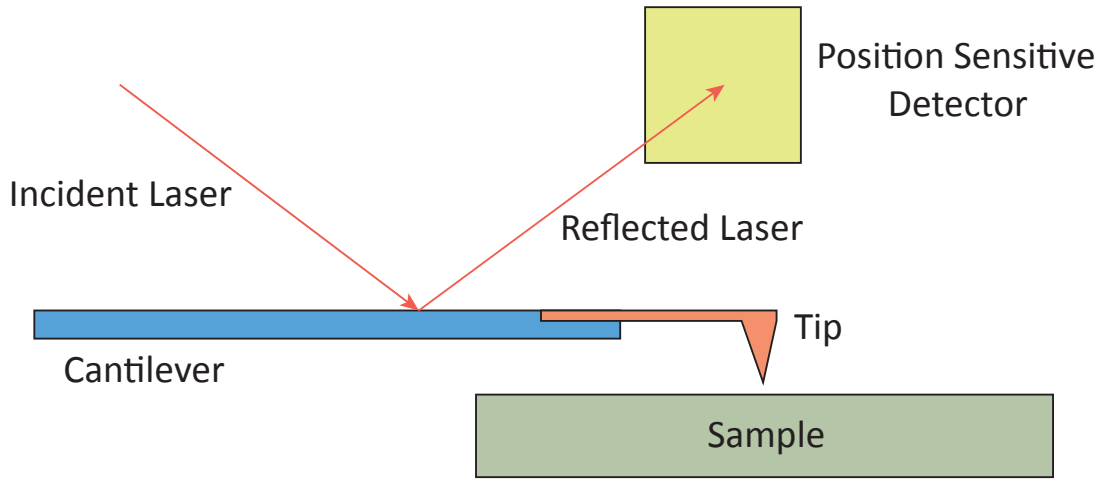

Figure 2.8 Schematic diagrams of the AFM system.

AFM measurements can be conducted in a number of different modes. The two modes used in this study are known as contact mode (C-AFM) and non-contact mode (NC-AFM). In contact mode the probe scans the sample surface and is deflected due to electrostatic repulsion between the probe and the surface atoms. The topography is obtained by keeping the probe at a fixed distance from the surface by correcting for any deflections caused by interaction with the surface. This correction then yields a direct image of the sample surface. The forces experienced by the cantilever will typically be in the 1-10 nN range hence the cantilevers have small spring constants (typically 0.1-3 N/m).

2.4.4 Near Edge X-ray Absorption Fine Structure

Near edge x-ray absorption fine structure (NEXAFS), is a type of absorption spectroscopy that indicates the features in the x-ray absorption spectra (XAS) of condensed matter due to the photoabsorption cross section for electronic transitions from an atomic core level to final states in the energy region of 50–100 eV above the selected atomic core level ionization energy, where the wavelength of the photoelectron is larger than the interatomic distance between the absorbing atom and its first neighbour atoms.

X-rays are absorbed through excitations of core electrons to empty states above the

vacuum or Fermi level due to the photoabsorption cross section for electronic transitions from an atomic core level to final states in the energy region of 50–100 eV above the selected atomic core level ionization energy, where the wavelength of the photoelectron is larger than the interatomic distance between the absorbing atom and its first neighbour atoms[57]. The energy of the incident photons is scanned across the ionization energy for a pre-selected core level. At the ionization energy there is marked increase in absorption (referred to as an absorption edge) as electrons are excited from the core state to the lowest unoccupied state above the Fermi level. As the incident photon energy is increased further the unoccupied states which exist at higher energies are populated in turn. As all photons are absorbed within the sample at soft x-ray energies the absorption can only be measured indirectly by measurement of emitted electrons. For materials with low atomic number, such as carbon it is the Auger emission which is dominant. Measurement of electron yield as a function of incident photon energy provides an indirect measurement of the x-ray absorption. Electrons can only escape from the near-surface region of the material. Two methods of electron detection exist. Total electron yield is obtained by measurement of the sample drain current which detects all electrons emitted from the sample. For Auger (or partial) electron yield only the electrons emitted at a pre-selected energy are detected using an energy analyser.

This technique requires a tuneable x-ray source such as a synchrotron, therefore the instrument used for this work was the D1011 beamline at MAX Lab, Lund University

Sweden.

2.5 Chapter Summary

In this chapter the methods used during this study have been discussed along with the theory of PES. This forms a basis for the next chapter where the instrumentation needed for the investigations is introduced. Other complementary techniques, LEED, VSM, AFM and NEXAFS used in these studies, have also been introduced.

CHAPTER 3 – INSTRUMENTATION

Instrumentation plays a critical role in the development of any characterisation technique such as x-ray photoelectron spectroscopy (PES). The theoretical basis for PES has already been discussed in the previous chapter. This chapter will present the main instrumentation on the custom-built Real-time Electron Spectroscopy (REES) system developed by the Aberystwyth University group.

3.1 The REES UHV System

The vacuum system at the Material Laboratory, Aberystwyth University, consisted of stainless steel chambers equipped with different experimental units, pumping system, and gas-lines. Figure 3.1 shows the configuration of this system.

Four UHV chambers are the basis of the system, which includes a fast load-lock, an analysis chamber, a transfer chamber, and a plasma chamber. Most of the processing and measurements are performed in those sections during investigations. Each chamber is isolated from the other with a UHV hand-valve. The load-lock chamber is pumped by a turbo pump and has a base pressure of $5x10^{-7}$ mbar. A magnetic arm is attached for transferring samples between the load-lock chamber and the transfer chamber. The vacuum in the transfer chamber is maintained with an ion pump and titanium sublimation pump (TSP), which has a base pressure of $5x10^{-10}$ mbar. The chamber is

equipped with an ion gun, mass spectrometer and a vacuum isolated Knudsen cell (K-cell) for depositing 5-FU (a drug molecule for cancer treatment). The analysis chamber is pumped with an ion pump and TSP filaments and has a base pressure of around $1x10^{-10}$ mbar. This chamber is equipped with an Al/Mg twin anode X-ray source, a rear-view LEED unit in line with the electron analyser, a Dycor quadrupole mass spectrometer (used only in this work to check vacuum quality and He leak-test) and two k-cells for depositing Fe and Ag. The K-cells are collimated and shuttered, and are positioned to avoid contamination of the analyser lens and x-ray head. A VG OMNIAX manipulator allows for precise control over sample position and is fitted with a heater. The plasma chamber is built for surface termination with active gas sources. A system of ¼ inch stainless steel piping was used to connect a plasma gas-line system to the plasma chamber. The gas-lines are pumped by a turbo and rotary pump for quick evacuation and have a high vacuum base pressure. The lines are connected to the glass capillary through a needle valve for controlling pressure during the termination.

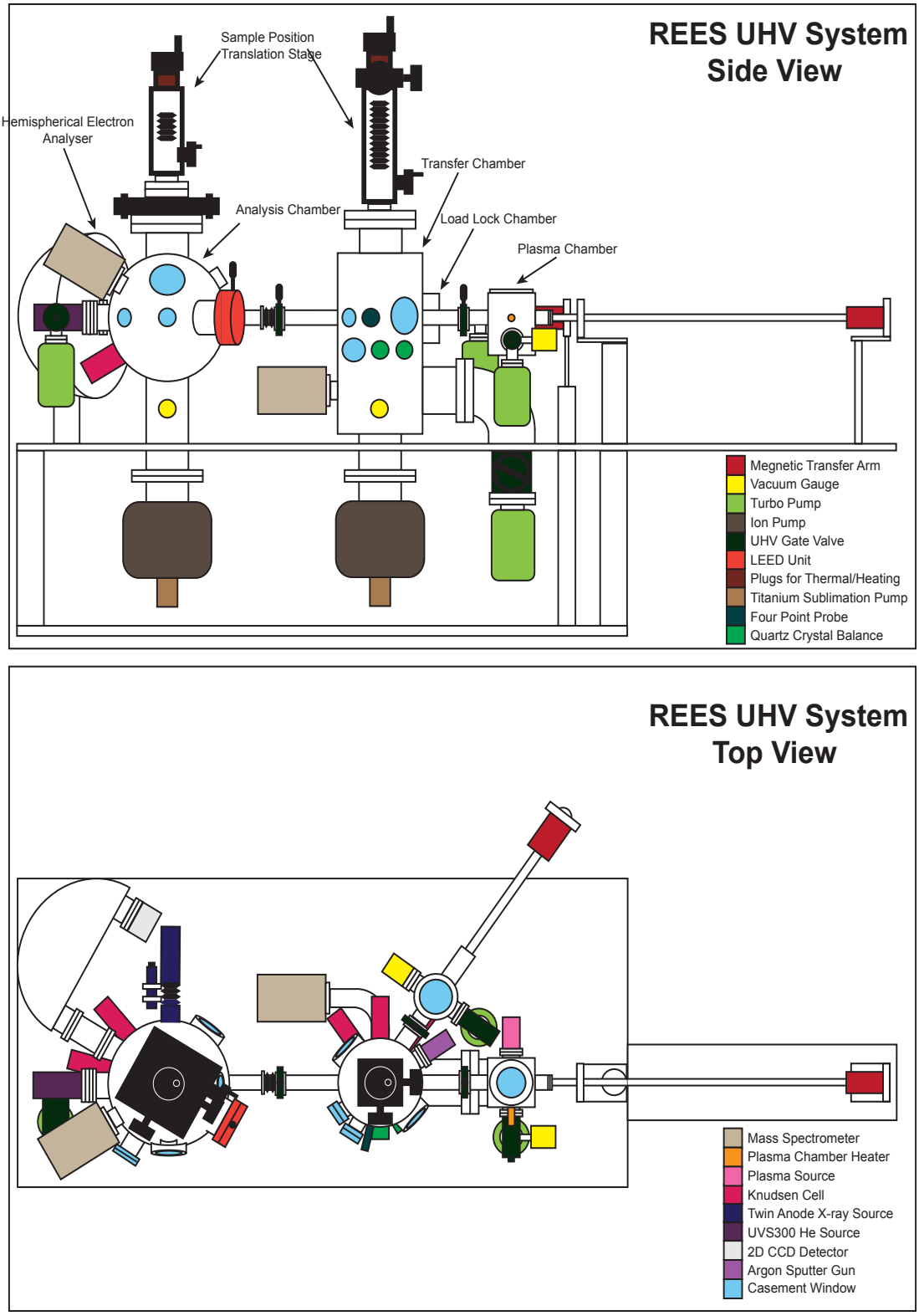

Figure 3.1 Schematic diagrams of REES ultra-high vacuum system with processing and detection units; (a) side view, (b) top view (refers from [58]).

The improvement of vacuum systems from those manufactured in glass has aided in the development of a semi-universal (differing only in the use of imperial or metric threads) method of creating UHV seals between chamber components, known as the Conflat flange seal [59]. To create the UHV seal a copper gasket is bitten from opposing sides by a machined 'knife edge' on the flanges. A helium leak test either by mass spectrometry attached to the vacuum chamber or a helium 'sniffer' at the discharge end of the rotary pump is performed to ensure a UHV seal has been made.

The pump system primarily consisted of four turbo pumps and two rotary pumps, which are connected to each vacuum chamber except the analysis chamber, as shown in Figure 3.2. Two ion-getter pumps are connected to the transfer and analysis chambers respectively. Two rotary pumps are employed as roughing and backing lines to provide a base pressure (10^{-3} mbar) for the turbo pumps. The roughing line is usually used for the baking procedure or other processing which may increase the pressure in a chamber, while backing line is used the rest of the time. The turbo molecular pump allows a pressure of around $1x10^{-9}$ mbar in the chamber after baking the system. However to decrease the pressure further (to $1x10^{-10}$ mbar), the use of ion-getter pumps is required. Ion pumps are a type of 'capture pump' as the gas is collected and captured in the pumps structure [60]. High voltage is used to reduce the pressure of the vacuum chamber, by ionising gas molecules and using magnetic fields to direct and embed them in reactive targets (primarily titanium).

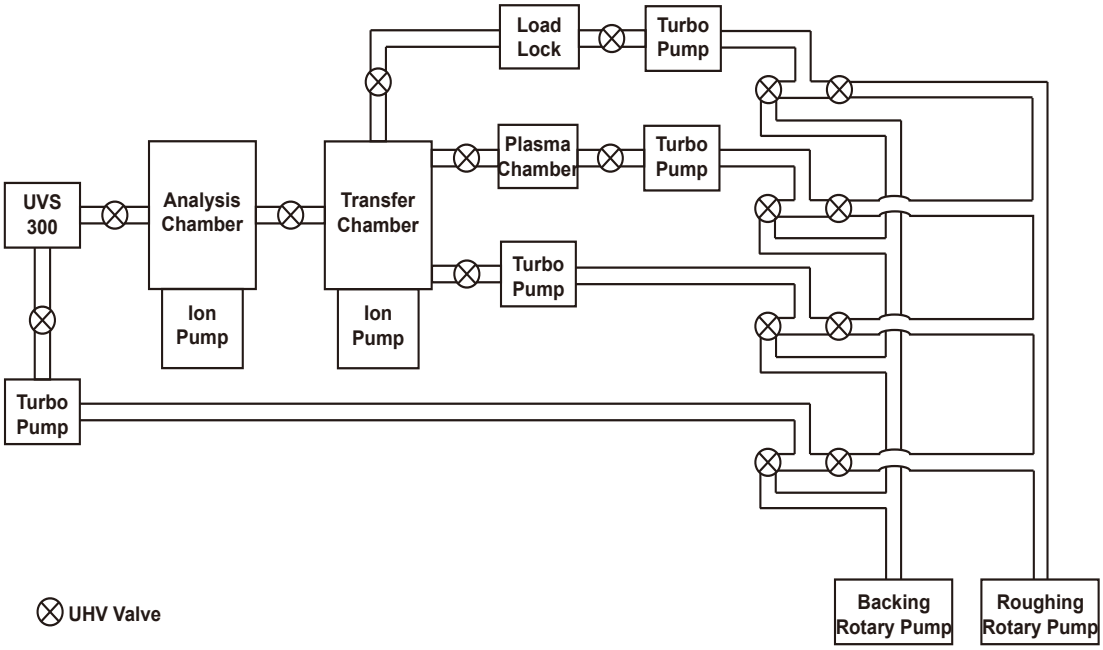

Figure 3.2 Schematic diagrams of the REES UHV pumping system.

3.2 Photon Sources

Utilising different photon sources allows the measurement of different properties or aspects of the sample. For instance, the energy of photon source has an important effect on the analysis and quantification of XPS spectra. Meanwhile, varying the photon energy allows for selection of surface sensitivity [61]. Different sources also vary in intensity and polarisation etc [62]. Two different photon sources are used during the course of these investigations at the laboratory; a twin anode x-ray lamp and a magnetron based helium plasma source for XPS and UPS respectively, which will be introduced in this section.

3.2.1 X-Ray Radiation Source

Since its early discovery in 1895 [63], x-ray radiation has been proven as one of the most powerful tools used to probe the properties of matter in a wide range of scientific disciplines. As detailed earlier, the quantification of a photoelectric peak in XPS relies on the incident x-ray photon being monochromatic and its energy known.

Using metal targets as anodes to generate x-ray photon sources is the conventional setup for laboratory XPS procedure. A VG twin anode x-ray gun has been used in the following investigations. It has Al and Mg anodes producing Al K*a* and Mg K*a photon* sources primarily. The lamp is operated at a bias of 15 KV and a flux of 20 mA at a distance of 25 mm from the sample surface. All data presented in this study was obtained using Mg K*a* radiation which has the narrowest line width of the two anodes at around 0.7 eV. In the twin anode x-ray gun, the x-ray source is produced by accelerating electrons emitted from a filament into a target anode that is at high voltage relative to the filament and ground (Figure 3.3). This produces a series of x-ray lines that are dominated by the K$\alpha_{1\text{-}2}$ transition at 1253.6 eV for the Mg and 1486.6 eV for the Al anode. However other less intense (higher energy) x-rays are produced due to other electron transitions within the metal anode such as $K\alpha_{3\text{-}4}$. But these transitions usually generate a negligible amount x-rays which have intensities ≤1.0 % of the $K\alpha_{1\text{-}2}$ peak [64].

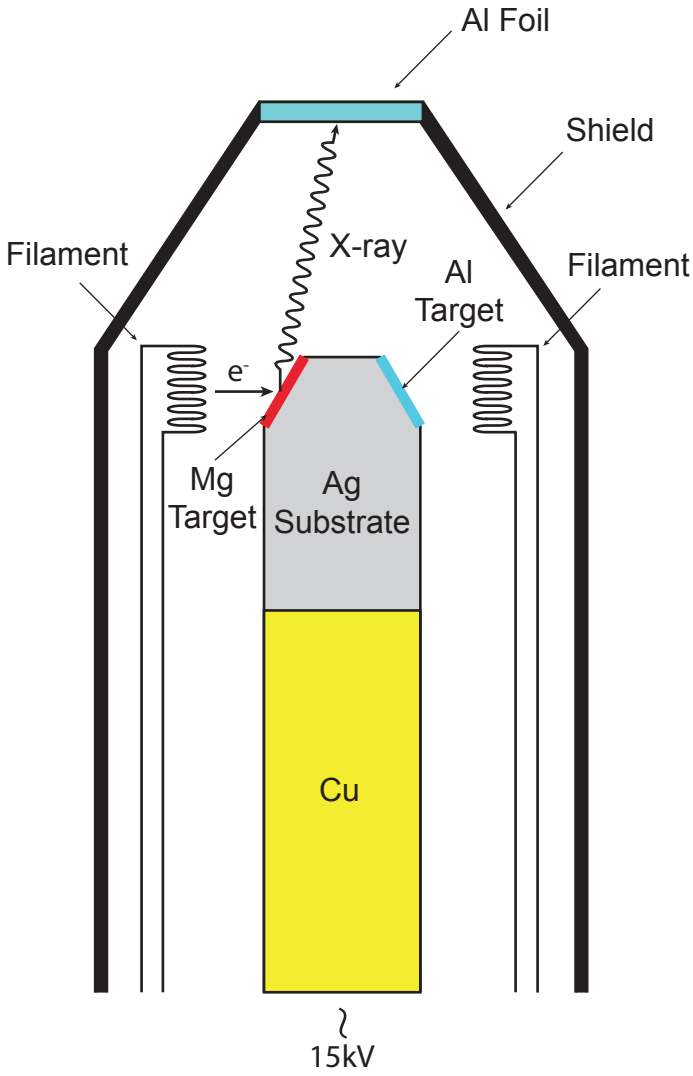

Figure 3.3 The configuration of a VG Twin anodes x-ray gun with Mg and Al anodes.

3.2.2 Ultraviolet Radiation Source

The high energy photons produced by the x-ray lamp (>1KV) allows the excitation of core-level electrons (those not involved in chemical bonding) from the sample. Since the photoionisation cross-section of core electrons is much larger in comparison with valence electrons at high energies, the intensity of core level peaks dominates the

spectrum, and features such as valence states are diminished. Therefore a low energy source to study the valence electrons is necessary for the full characterisation of the sample under investigation.

In this case, characteristic emission lines from various noble gases are conventionally used as an excitation source for ultraviolet photoelectron spectroscopy (UPS) or angle-resolved photoelectron spectroscopy (ARPES) with the sources known as a discharge lamps [65]. Resonant fluorescence is produced when the gas is excited and decays, emitting high intensity photons with narrow line widths [19]. A UVS-300 Specs high brilliance UV source is employed in the following studies to produce HeI and HeII lines at 21.2 eV and 40.8 eV respectively. The generation of a high density plasma in a small region of the discharge section of the lamp is achieved by guiding electrons emitted from a hot filament along the lines of a strongly inhomogeneous magnetic field within a partial pressure of the noble gas species required [66]. A turbomolecular pump is located between the discharge chamber and a quartz capillary used for extracting the ultraviolet radiation to analysis chamber (shown in Figure3.2). The UV source generates a small spot (diameter at ~ 1mm) on the sample surface at a maximum induced photocurrent of 200nA.

3.3 Surface Treatment

As discussed in the last chapter, the surface *in situ* processes in this work were performed by thin film deposition or active gases termination. In these investigations,

homemade Knudsen cells (K-cell) are used as evaporation source for thin films growth, and a non-thermal plasma source at the laboratory is used for the surface terminations.

3.3.1 Knudsen Cell (K-cell)

A large variety of deposition technologies have been developed that can facilitate the growth of materials for both industrial and academic areas during the past decades, including thermal evaporation in vacuum, glow-discharge processes (ion sputtering etc.), gas-phase chemical processes (CVD etc.), liquid-phase chemical processes (electroplating) [67], and liquid-phase evaporation in vacuum via electrospray which has been demonstrated recently [68]. Among those thermal evaporation via physical vapor deposition (PVD) in vacuum has been employed for the following studies, which is a primary technique that enables the deposition of a wide range of materials[69, 70].

Homemade Knudsen cells (K-cells) were used for the deposition of 5-Fluorouracil and pure Fe during the following investigations (illustrated in Figure 3.4). A ceramic crucible containing the desired material is heated by passing current through a tungsten wire wrapped around the crucible in vacuum. Here the tungsten wire is threaded through ceramic tubes to ensure electrical isolation from each other. A K-type thermocouple is attach to the crucible for monitoring the temperature of the source, and a stainless steel shroud around the entire unit ensures that a collimated beam of the source propagates toward the sample surface within the vacuum vessel, whilst also acting as radiative heat

shield. The source is supported on stainless steel rods fixed to a CF70 vacuum flange. Shutter is present at the end of the shroud for controlling the deposition time.

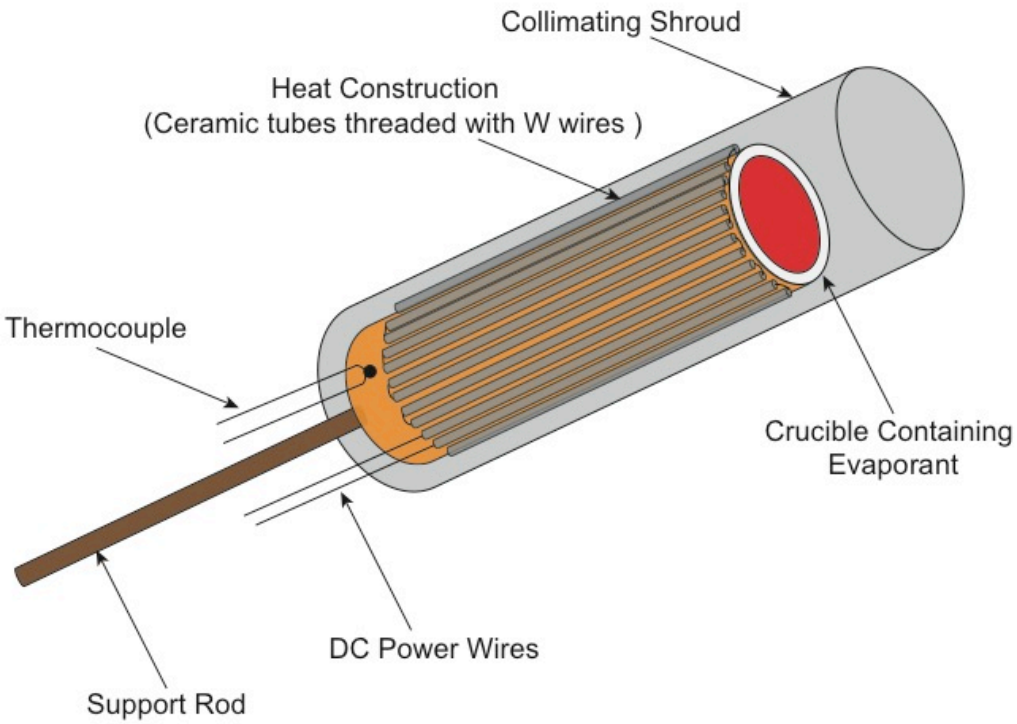

Figure 3.4 A schematic diagram of the homemade Knudsen cell used for PVD of metals and organic materials in Aberystwyth materials laboratory[58].

The temperature and pressure of vacuum chamber must be maintained at a minimum level (usually around 3-8x10^{-9} mbar) during the deposition of materials with high melting temperatures such as metals, due to the chamber and deposition material outgassing contaminations onto the sample. In this case, water-cooling is equipped in order to maintain the high purity of the deposition beam. Another important parameter for depositing with K-cells is the growth rate of the thin films, which is dependent on the material, evaporating temperature and surface [21]. However the most controllable method to achieve a constant growth rate is by varying the

temperature (power) of the K-cell, which measured by a thermocouple in contact with the crucible. A well-calibrated growth rate can be measured with an oscillating quartz crystal thickness monitor [71] or calculated from XPS spectra for thin coverages [61].

3.3.2 Non-Thermal Plasma Source

As it shown in Figure 3.5, the custom UHV non-thermal plasma source at the laboratory was first setup by S. Evans in 1970s [72]. Activated hydrogen (H*) can be created by using a source gas mixture of 50/50 argon in hydrogen. Argon is used in the hydrogen because it lowers the striking voltage necessary to create the plasma (Paschen's law), in turn ionising the hydrogen (which has a much higher striking voltage). A brass microwave cavity (MW-cavity) is placed around a quartz tube which connects with the plasma chamber and is sealed by polytetraflouroethylene (PTFE) ferrules within hoke fittings. Manipulation of the MW-cavity around the quartz capillary is possible via orthogonal micromanipulators in order to tune the cavity a tuning pin that changes the internal dimensions of the cavity (hence resonance frequency) also aids this. Compressed air forced around the capillary and cavity was used to cool the instrument during operation.

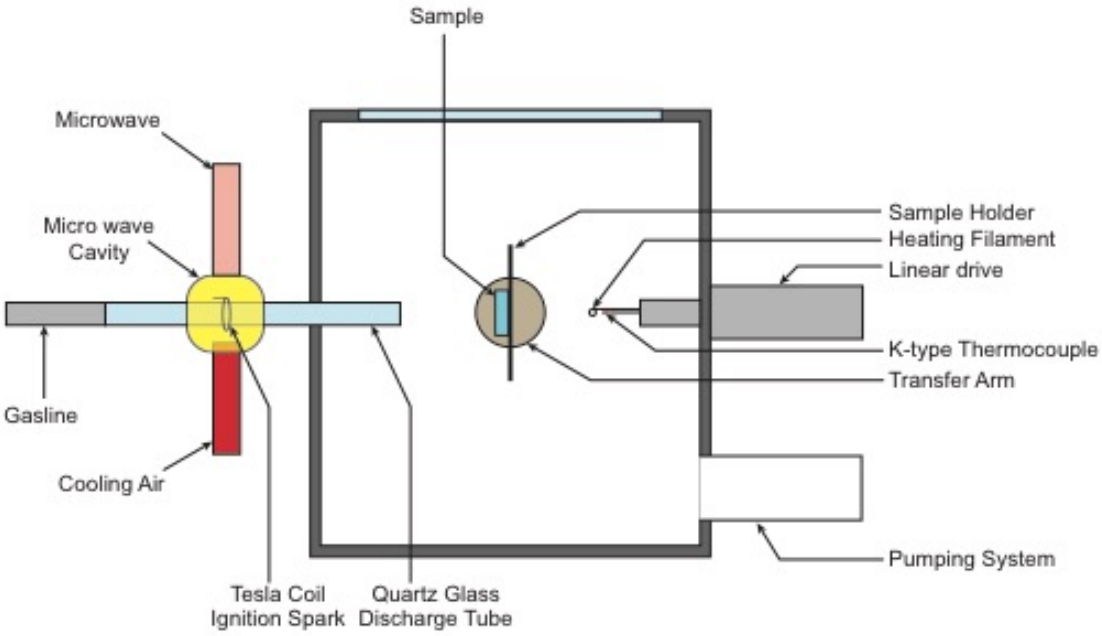

Figure 3.5 A cross-section diagram of the custom made plasma system on the REES system.

Microwaves generated by a 2.45Ghz microtron (EMS200 MKII) were coupled to a reflected microwave power meter, which was used to assist the tuning of the cavity (lowest reflected power). The MW-cavity lies at a distance of 100 mm from the sample position, and the end of the quartz tube is 20mm away from the sample. A tungsten bulb filament and thermocouple can approach the rear of the sample holder in order to increase the substrate temperature to near 600°C. The thermocouple is placed in good contact with the rear of the sample holder during heating. The hydrogen plasma is normally performed at pressure of 6×10^{-4} mbar (measured by Pfeiffer full range cold cathode gauge) excited by 150W microwaves at a reflected power <3W. Hydrogenation of the sample was performed with a substrate temperature at 450°C for 20 min and then controlled cooling of the substrate to 200°C over 20min.

3.4 Sample Holder and Stage

In vacuo annealing can be performed on the sample during the real-time measurement in the analysis chamber as another type of *in situ* treatment used for these investigations. A good thermal contact between the sample and the heater is therefore crucial for precisely controlling the temperature of the sample.

3.4.1 Sample Holder

Figure 3.6 presents the custom-made molybdenum sample holder which is employed in the vacuum system. 0.2mm molybdenum (Mo) sheet was used for the sample holder due to its high melting temperature and good thermal conductivity. A top plate was handmade with 0.125mm thick Mo for each sample. The faceplate then slides under the folded 'wings' of the sample holder to create a secure mount for the sample.

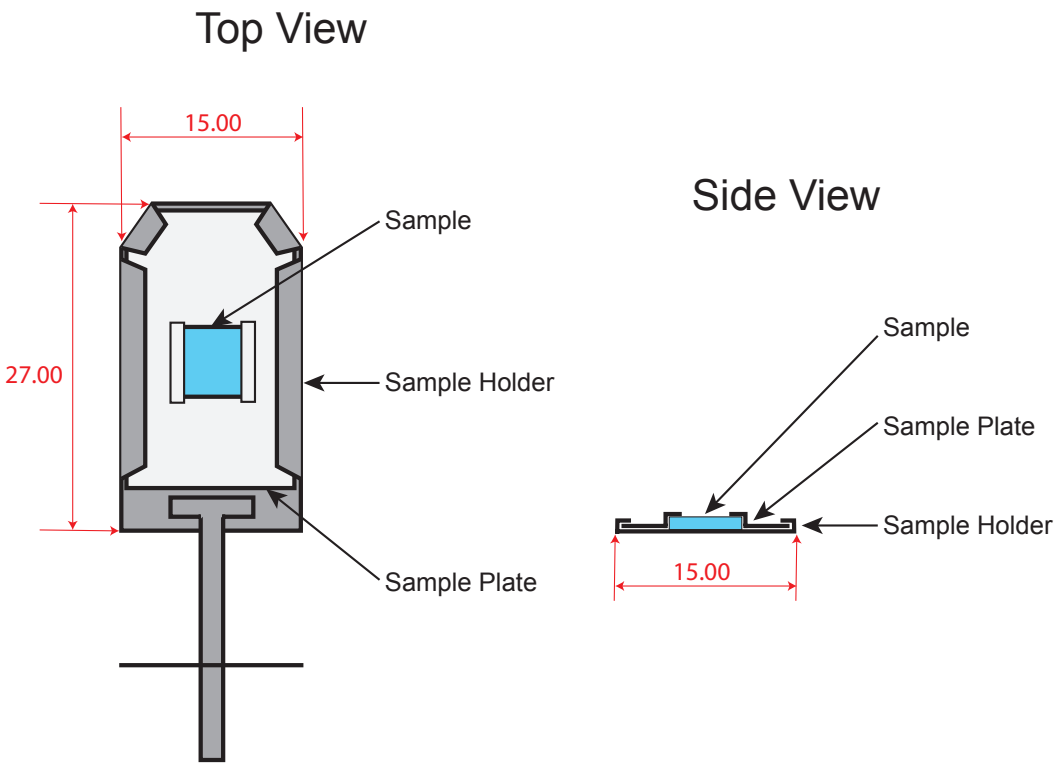

Figure 3.6 Schematic diagrams of the standard custom Mo sample holder (dimensions in mm).

3.4.2 Sample Mounting & Heating Stage

The sample stage consists of a 0.3mm thick Tantalum (Ta) faceplate and a UHV compatible Boralectric® heater, which comprises of encapsulated graphite tracks within boron-nitride (BN). These two parts were connect through Ta rods, Mo nut and ceramic washers, as shown in Figure 3.6, which makes a good thermal contact with sample during the measurement and enables heating the sample up to ~1200°C maximum. A type-K thermocouple is mounted on one of the ceramic support rods and in good mechanical contact with the Ta faceplate which can measure the sample temperature, whilst sample ground/drain source is connected with the other bolt. Two stages of

reflective heat shields are mounted on the rear side of the heater to ensure that heating of the connection cables (not shown) that traverse up the rear of the manipulator plate is kept to a minimum. 1mm diameter Ta wire was spot-welded to the rear of the faceplate as rails for guiding and securing the sample holder. A programmable Kenwood PDS60-12 regulated DC power supply is used for heating power and the constant-current vs time profiles can be exported with LabVIEW software.

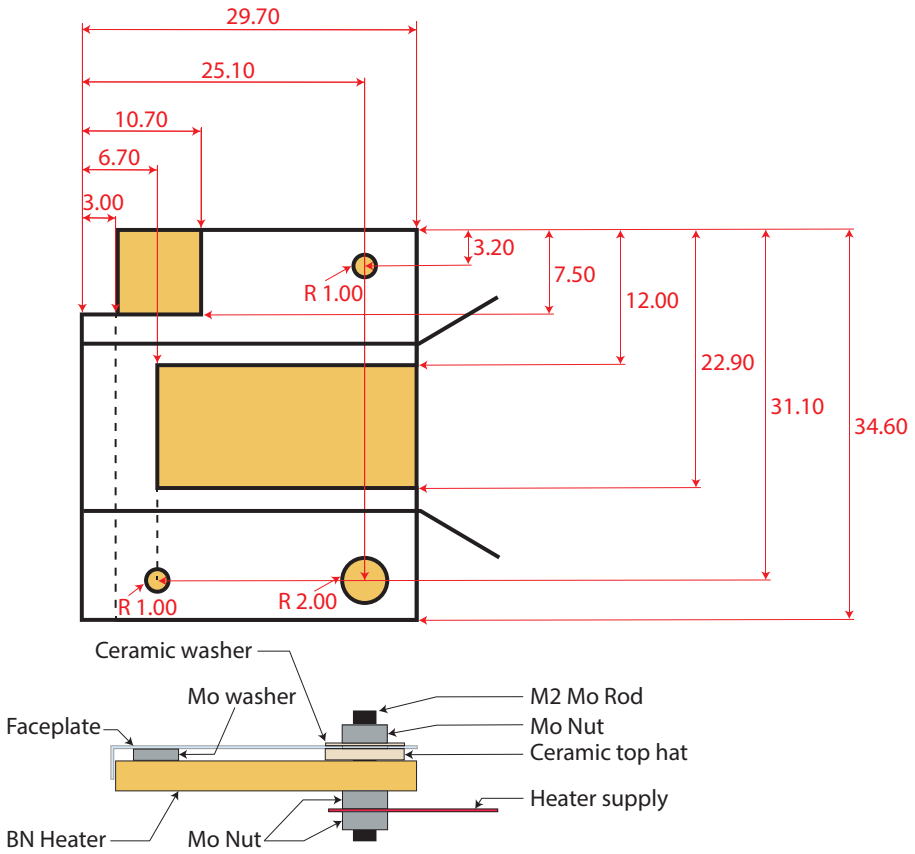

Figure 3.6 Schematic diagrams of the standard custom made sample stage with the Boralectric® heater equipped on the manipulator for the transfer chamber and analysis chamber (dimensions in mm).

3.5 Electron Analyser

A large variety of techniques have been used to measure electron spectrum including time of flight, deceleration in an electric field, or orbit change in a magnetic field [37]. In a PES measurement, an electron energy analyser is used to disperse the photoelectrons emitted from the sample into their respective kinetic energies, therefore to generate an electron intensity curve as a function of kinetic energy (known as the PES spectrum) [73]. A 'SPECS Phoibos100' hemispherical electron analyser (HSA) is the primary analyser in the Aberystwyth materials physics laboratory. Figure 3.7 shows the operating principle of the hemispherical electron analyser. The HSA is based on two hemispheres, which are electrically isolated. At one end of the hemispheres is an entrance plane containing an entrance slit, while on the opposite side is an exit plane.

The 180° geometry provides perfect focus of electrons from the entrance slit to the exit plane without distortion, making it superior to other analyser designs [74]. After being excited into vacuum (aka the photoemission process), photoelectrons are collected and retarded by the electrostatic lenses and then focused onto the entrance plane of the HSA. Two negative voltages (V_1 and V_2) applied to the two hemispheres (R_1 and R_2) result in electrostatic dispersion of the electrons and imaging at the exit plane. As shown in Figure 3.7, the trajectory of the higher kinetic energy electrons through the analyser is in blue while the trajectory of the lower kinetic energy electrons is in red. The energy of those electrons following a perfect trajectory (green) through the

analyser is known as the pass energy E_p, which is dependent on the difference in potential ΔV applied between the two hemispheres and the radii of the inner and outer hemispheres, given by *Eqn 3.5.1*, where q is the electron charge [7].

$$E_p = (-q)\Delta V\left(\frac{R_1 R_2}{R_2^2 - R_1^2}\right) \qquad (Eqn\ 3.5.1)$$

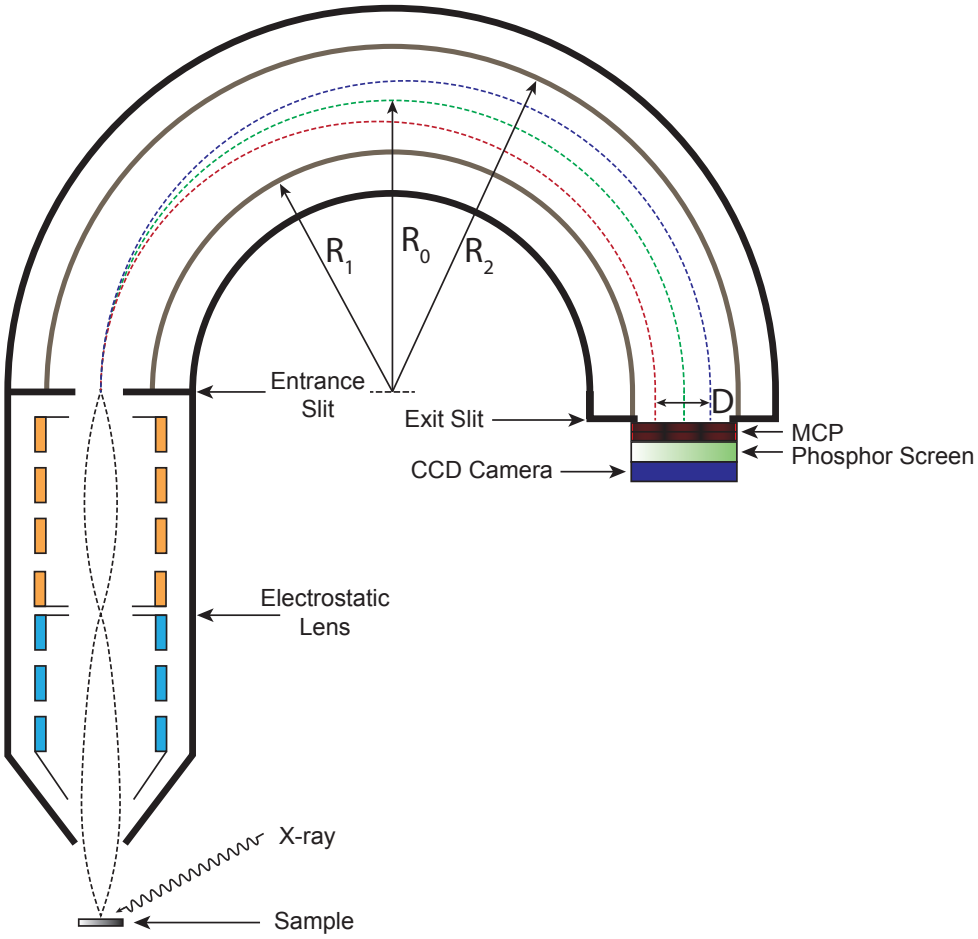

Figure 3.7 Schematic diagram of the hemispherical electron analyser. R_1 and R_2 are the radii of the inner and outer hemispheres respectively, whilst R_0 the mean path of the electron beam.

The resolution of the photoelectron spectrum can be adjusted via controlling the pass

energy of the analyser. Usually, high resolution spectra can be acquired with a small pass energy, although the intensity of the spectrum will be attenuated due to less electrons imaged on the exit slit. In contrast, with a high pass energy can improve the electron transmittance, i.e. signal strength, but results in a low resolution of the spectrum. Photoelectrons are collected and focused by the electrostatic lens and the kinetic energy of these electrons will be retarded to the pass energy at the entrance silt. The energy resolution of this mode can be obtained from the following equation:

$$\Delta E = E_p\left(\frac{R_1 R_2}{2R_0 + \alpha^2}\right)$$

(*Eqn 3.5.2*)

where R_0 is the mean radii of the two hemispheres and α is the angular half aperture of the electron beam at the entrance slit and is determined by the electrostatic lens system. With the analyser functioning in this way the spectrum acquired is known as a fixed analyser transmission (FAT), which is always used when performing XPS. In order to acquire a spectrum over larger energy ranges it is necessary to scan the potential applied to the lenses. The efficiency at which the lenses deliver different energies onto the focal plane of the analyser is called the transmission function, and differs for all lens modes of the analyser. The transmission function therefore plays an important role in quantifying the intensity of peak profiles. It is usually included in the data acquisition software and transferred to the analysis software for this purpose.

Traveling through the hemispherical analyser, the dispersion energy scale of the electrons at the focus plane is related to the position at which they appear on the screen. The energetic dispersion being determined by the electron pass energy. A relationship between electron energy and position along the exit plane is given by,

$$\Delta E_k = D(\Delta x)$$

(*Eqn 3.5.3*)

where ΔE_K represents kinetic energy, D the dispersion in eV/mm, and Δx distance along the plane.

3.6 Position Sensitive Detector

The Aberystwyth group has developed a custom made multi-channel detector and realised the measurement of a core level spectrum in second regime[11, 15]. The electrons are detected by several methods when they arrive at the exit plane of the HSA. For acquiring an electron energy spectrum, it is necessary to count the number of electrons as a function of energy. Originally the channeltron detector (a type of photomultiplier tube) was the optimum detector of choice due to its dynamic range, detection efficiency and lifetime. For a given set of analyser voltages only electrons of a known energy could traverse to the electron counter. Thus by varying the analyser voltages the electron energy distribution could be measured. The disadvantage of the single detector mounted at the exit plane of the analyser is that efficiency is too low, due to all electrons with trajectories outside the exit slit being lost, extending the

amount of time for measuring. Researchers then realised that having more than one exit slit/channeltron configuration would allow the spread of the spectral features to be captured more easily and with more energy resolution. Early systems focused on one exit slit at either side of the central slit, which later developed into a multi-slit configuration. An example is the SPECS Phoibos MCD-9 detector, which has nine slits [75]. Although it was still not efficient enough, only 7% of the available energy window will be counted at any time [8].

Position sensitive detectors (PSD's) are capable for spatially resolved electron counting at the analyser exit plane, which are primarily composed of a microchannel plate, an array of many photomultipliers (or channel electron multipliers CEMs) in parallel with each other[76]. Each unit of those detectors allows for counting the number or luminescent intensity of incoming electrons. With PSDs, the efficiency of detection and time of measurement have significant improved. Four classes of PSD are noted in the literature; discrete channel, coincidence array, charge division and optical image detectors. The last method was used for this investigation.

Figure 3.8 shows the configuration of the PSDs. A microchannel plate (MCP) is employed for amplifying the number of electrons impinging on the detector after traversing the analyser to the exit plane. The channels are usually made from semiconducting glass, so that large amounts of secondary electrons treated can be generated with the inner

wall, and electrons can be easily amplified by applying a kilovolts high potential across the plate[77]. When an electron enters the MCP it collides with the wall and ejects more electrons, and as the tubes are in an array, the emission onto the detector is still spatially resolved in energy. Therefore only a gain in the number of electrons detected is caused via the MCP, further enhancing the time efficiency of this method. Typical gains are expected of between 10^3-10^5 counts.

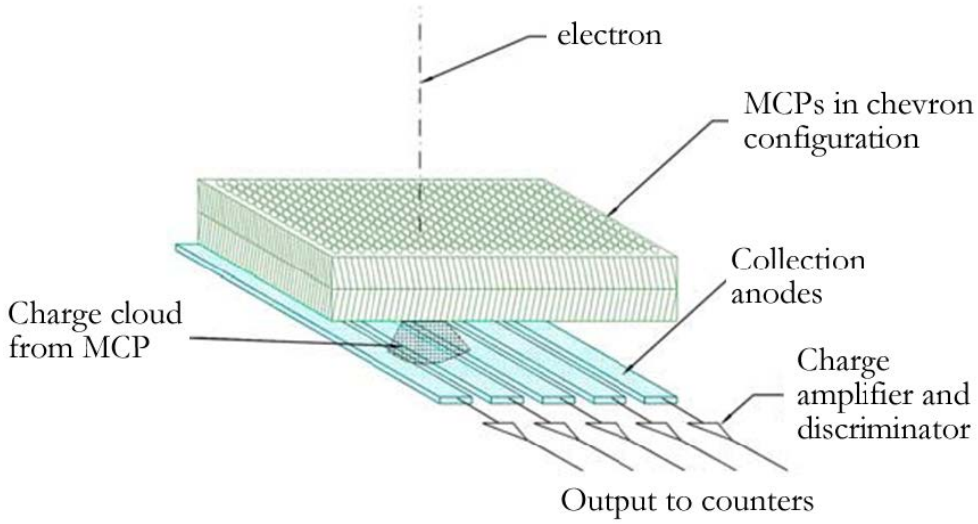

Figure 3.8 The operating principle of a position sensitive detectors (taken from reference[11]). Photoelectrons are directly detected on collection anodes situated underneath a multi-channel plate electron multiplier. Each anode is in direct contact with its pre-amplifier and discriminator circuitry.

Discrete channel detectors are a series of collecting channels positioned underneath the MCP, each channel being connected to a discriminator and pulse counting hardware, which may directly count the number of incident electrons. Therefore the number of discrete channels available aids in counting efficiency. Early examples have been demonstrated

consisting of 40 channels [8] and 96 channels [10]. Incorporating the electron counting electronics and channels into a single device addresses as the noise and geometric difficulties. However progress on the denser arrays has been made, including those created at Aberystwyth University that increased the number from 198 channels to 1526 channels (currently being characterised) by D. Langstaff and A. Evans [11, 12, 78].

The optical image method is an indirect method relying on the conversion of electrons to photons by using a phosphorescent screen and imaging the screen with a Charge Coupled Device (CCD). The phosphor screen/CCD configuration has an advantage over the discrete channel method in that it measures the exit plane in two dimensions allowing the energy and angular distribution of the electrons to be determined, and was used in this work. Here the electrons that are generated in the MCP are incident on a phosphor screen in turn causing luminescence, and then the fluorescence is imaged with a CCD. The energy scale of the energy-dispersed electrons at the exit plane (energy window) is then related to the position at which they appear on the screen (pixel number). As the pass energy changes, the scale of the energy window changes (amount of dispersion from the perfect transmission trajectory in figure 3.7), and a relationship for the measured kinetic energy at the screen can be derived from *Eqn 3.5.3*, given as,

$$\Delta E_k = D(\Delta_{pixel})$$

(*Eqn 3.5.4*)

where ΔE_K represents kinetic energy, D the dispersion in eV/pixel, and Δ_{pixel} number of

the pixel.

3.7 Real-time Electron Spectroscopy

As the main spectroscopy kit at Aberystwyth group, most of the techniques and instrumentations on the Real-time Electron Spectroscopy (REES) system have been introduced, including the UHV system, PES and *in situ* processing units etc. The units equipped on each part of the system have been introduced in part 3.1 combined with the UHV system and the configuration of the entire system has been illustrated in Figure 3.1. However, in this section, the operating process of the real-time electron spectroscopy (as shown in Figure 3.9) will be explained.

The REES is composed of a sample stage, evaporating sources (K-cell) and a photoelectron spectrometer equipped with a CCD, which allows 477 pixels across the energy dispersive for snapshot spectrum. The graphite/BN boroelectric heater attached to the sample stage can provide controlled temperature profile on the sample by applying programmable power (maximum temperature as 1200℃). Therefore the real-time measurements make it possible to measure a core level electron spectrum in seconds-regime during the surface treating process (including the annealing process and thin film deposition process). The real-time data could present the spectra in 2D block mode as shown in Figure 3.9, which is a series of the core level snapshots during the

acquisition period.

A single file, which contains experimental variables (time, pressure, temperatures, heater current, heater voltage) and the snapshot spectrum, can be exported with LabvVIEW software. Files were composed of 14 columns of experimental variables and 477 columns of CCD pixel intensities, with each row representing one measurement. After processing with the CasaXPS software, specific information on the core level spectra can be used for analysis and further discussion, for example plotting the variation of peak position vs intensity with the time. The snapshots are usually fitted in CasaXPS with a SGL (Sum Gaussian-Lorentzian) line-shape (Voigt function) with a Shirley background [79]. In addition, the conventional XPS, UPS and LEED measurements can be used for further characterization, such as studying the chemical composition and electronic structure of the surface.

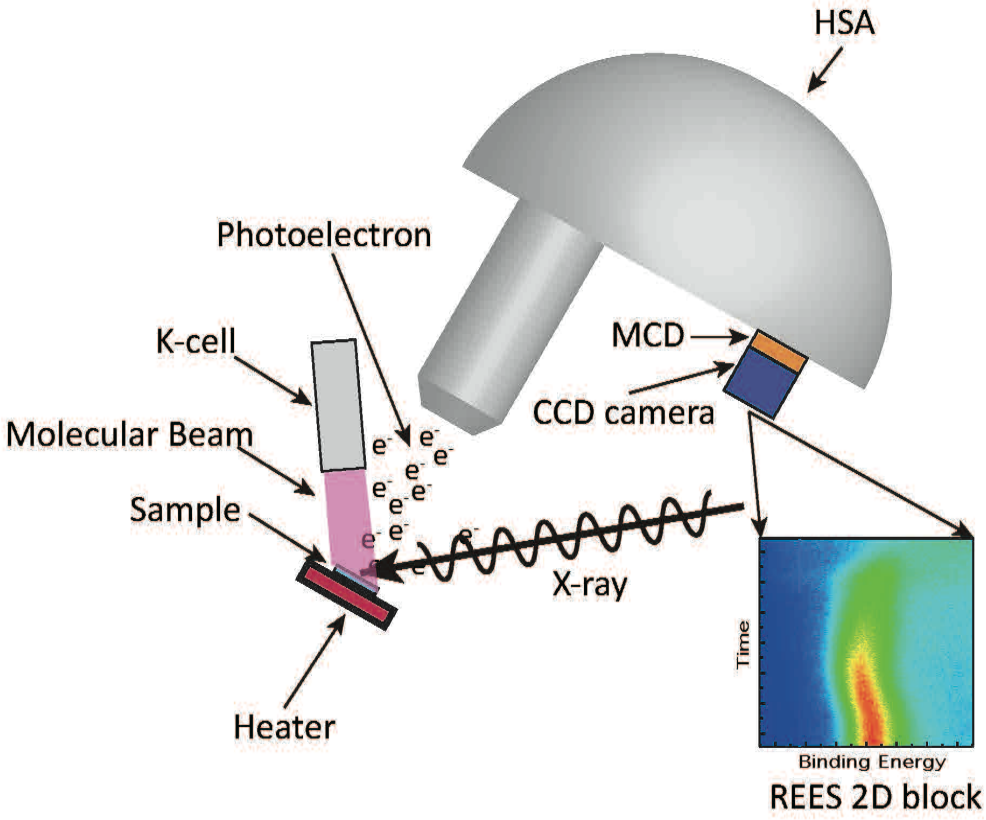

Figure 3.9 Schematic diagram of operating process of Real-time Electron Spectroscopy, consisting of a sample stage, *in situ* heating/deposition devices and a hemispherical electron analyser equipped with a 477 pixels CCD unit.

3.8 Chapter Summary

In this chapter, the main instrumentation requirements for x-ray photoelectron spectroscopy have been presented. An overview of current developments in the field of fast electron detection, which underpins the ability to perform real-time photoelectron spectroscopy has been given. It has demonstrated that the Aberystwyth REES system allows temperature-dependent and thickness-dependent real-time photoelectron spectroscopy to be performed with the laboratory x-ray source. The following chapters will present experimental data gathered using this system.

CHAPTER 4 – DIAMOND SURFACE

4.1 Introduction

During the past few decades, diamond research has been a focus of materials scientists worldwide. The superior hardness, chemical stability and thermodynamic properties have all been well established. Semiconducting diamond was found having great potential in the application of electronics due to its extraordinary properties, including biosensors [80], transistor [81, 82], and photonic and optical devices [83, 84]. Furthermore, it has recently been reported that the unique spin properties of the diamond nitrogen-vacancy (NV) center allow it to act as a solid-state “artificial atom” [85, 86], and thus acknowledged as a promising technique in application of spintronic devices [87-89] and quantum information [90, 91]. It has been found that the desirable optical and spin properties of NV centers are affected by interactions with the near-surface properties of diamond [92]. However, as the dimensions of diamond-based applications continue to decrease and quantum devices approach nano-scales, the role of the surface therefore becomes increasingly important and challenging in both the industrial and academic fields. In this case, the chemical and physical modifications on the surface are widely utilized as one of the most conventional and effective methods for developing and controlling diamond-based applications [16, 93, 94].

4.1.1 The Nature and History of Diamond

Diamond, as an allotrope of carbon, is in a metastable phase at atmospheric pressure and room temperature, where the thermodynamically preferred allotrope of carbon is graphite; therefore the existence of diamond at room temperature is due to the large activation barrier for conversion from diamond to graphite. As a material which possesses many extreme properties including extreme hardness, high thermal conductivity and a wide-range optical transparency ranging from the far IR to UV [95], diamond is unique in many ways.

- Extreme mechanical hardness (*ca.* 90 gPa) and wear resistance
- Highest bulk modulus (1.2×10^{12} N m^{-2})
- Lowest compressibility (8.3×10^{-13} m^2 N^{-1})
- Highest room temperature thermal conductivity (2×10^3 Wm^{-1} K^{-1})
- Thermal expansion coefficient at room temperature very low (1×10^{-6} K)
- Broad optical transparency from the deep ultraviolet to the far infrared
- Highest sound propagation velocity (17.5 km s^{-1})
- Very good electrical insulator (room temperature resistivity is *ca.* 10^{13} Ω cm)
- Diamond can be doped, becoming a semiconductor (wide bad gap of 5.5 eV)
- Very resistant to chemical corrosion
- Biologically compatible
- Some surfaces exhibit very low or 'negative' electron affinity

Table 4.1 Some 'extreme' properties of diamond (taken from reference [95])

Various valence and hybridisation states can occur through combination of the valence electron wave functions in carbon. For diamond, due to the overlap of the wave functions with neighbouring atomic sites within the lattice, a combination of s and p like character functions arise from the L-shell of the ground-state atom ($2s^2 2p^2$). Sp^3 hybridisation occurs when a C has 4 attached groups This means that four independent valence electron states are now available for bonding, which in the case of diamond bond to four neighbouring carbon atoms (sp^3-bonded) creating the tetrahedral symmetry and configuration shown in Figure 4.1. The resulting crystal structure is two interpenetrating FCC lattices with a cubic edge length of 3.57 Å and a C-C spacing of 1.54Å [96].

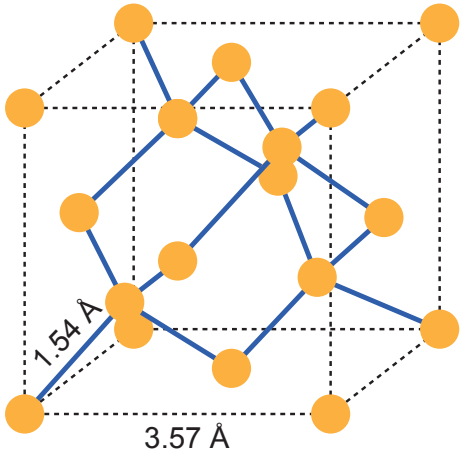

Figure 4.1 Diamond cubic structure.

Natural diamonds usually contains a variety of impurities (especially nitrogen). The range of defects in diamond result in a wide array of characteristics, thus stringent guidelines are in place for the classification of natural diamond, for example classified by color[97],

transparency [98], purity [99]. Two types were first distinguished by Robertson *et al* as a small number of diamonds showed lack of absorption in the infrared and the ultraviolet, which is based on nitrogen concentration and used to classify natural crystals [98]. The 'transparent' diamonds were classified 'Type II' and the majority 'Type I'. It was found that the lack of nitrogen was responsible for the deviation in spectroscopic absorption where natural diamonds of Type I contain around 0.3% nitrogen and Type II virtually none. Further subcategories were added when phosphorescence and conductivity were apparent in a tiny fraction of the stones studied by Custer [99]. Boron substitutions in the lattice were responsible for the observed conductivity.

- Type Ia – Nitrogen content of around 0.3% (Most common)
- Type Ib – Very low nitrogen content around few hundred ppm (Rare)
- Type IIa – Undetectable amount of nitrogen (Very rare)
- Type IIb – Naturally boron doped, semiconducting (Extremely rare)

Table 4.2 Four categories of current classification of natural diamonds.

Diamonds formed naturally in the earth under high pressures and temperatures usually are insulating. The first synthetic crystalline diamond was demonstrated by General Electric in 1950s with a high-pressure high-temperature (HPHT) method [100]. By subjecting graphite to extreme pressures in a cell full of transition metal at high temperature, diamond crystals were produced in small size and can be used as abrasives. The process is now available to produce large crystals; however the substrates for

electronic applications can not be produced due to an abundance of nitrogen defects created with this method. In this case, researchers have invented Chemical Vapor Deposition (CVD) methods to produce thin films of diamond that met the stringent requirements for semiconducting applications; namely good crystallinity (polycrystalline or monocrystalline), low nitrogen content (for transparency), selective dopant levels (to vary the conductivity) and large wafers for industrial processing of devices. CVD synthesis of diamond is also possible and was also demonstrated in the 1950s but was not pursued until the 1980s due to the low growth rates [101]. A vast variety of large single crystal growth is now possible with CVD with a high degree of control over the chemical content [32]. The most common technique of CVD growth is microwave plasma CVD (MPCVD) method. The process involves some initial gas phase chemistry, in which the reactant gas (gases) is (are) activated into the atomic state, and then incident onto a substrate for epitaxial growth. The growth mechanism relies on the different bond strengths between the gas species. The added advantage of doping the material during growth with boron means that it is possible to produce p-type semiconducting and even superconducting diamond wafers[102-104].

4.1.2 Diamond Surfaces

Utilising boron-doped diamond wafers as semiconducting substrates has been discussed for decades due to its wide band gap. In this case, understanding the various band gap states is of fundamental importance for research. For the semiconductors, these states

depends on the passivation of the surface dangling bonds, either by chemisorbed adsorbates or by the formation of mutual chemical bonds as a consequence of surface reconstruction. Depending on the type of surface termination, specific surface states in the gap of the semiconductor are eventually formed at the surface with wave functions more or less localized at the surface and with the capability of accommodating extra electrons or holes extracted from the bulk of the material. The growth dominates on the two crystallographic planes (100) and (111), illustrated as in Figure 4.2; however (100) is the preferential growth direction as stacking faults along the (111) direction are easily formed [105, 106]. A single crystalline CVD diamond with (100) facet was used for this investigation.

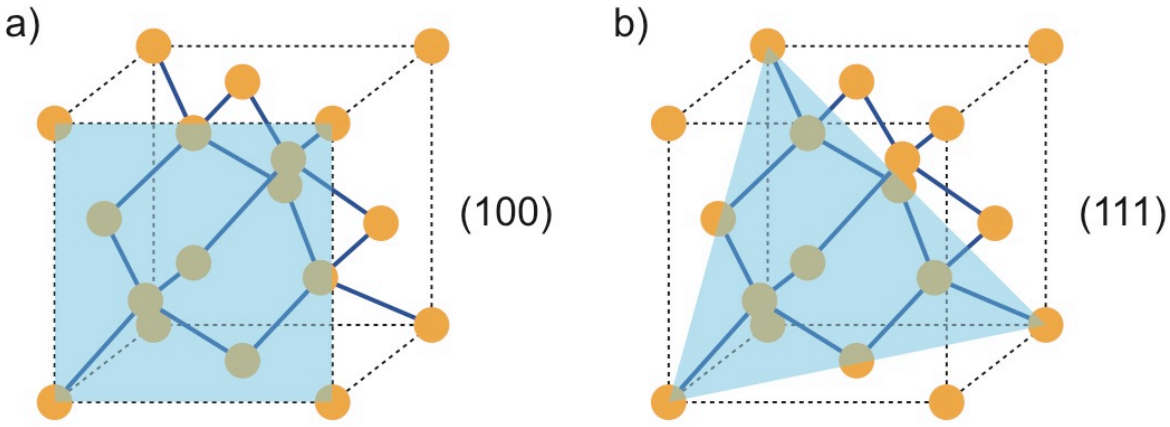

Figure 4.2 The (100) and (111) crystallographic orientations in diamond lattice, shown in a) and b) respectively.

The bulk terminated diamond (100) surface contains two dangling bonds per surface atom and favors lowering their energy considerably by forming mutual bonds. As a consequence, a clean diamond surface is unstable in the 1x1 geometry (Figure 4.3a) and

reconstructs into a 2x1 geometry (Figure 4.3b) with neighboring surface atoms forming π-bonded dimers along the (011) axis. The atomic spacing of the surface atoms is $\frac{a}{\sqrt{2}} = 2.523\,\text{Å}$ for the 1x1 geometry, while π-bonded dimers of the 2x1 geometry has a spacing of d(C-C) as $1.37\,\text{Å}$. Since the surface has a twofold symmetry ($\theta_{\text{mirror plane}}$=90°) the reconstruction is equally likely to occur along the $[01\bar{1}]$ direction, meaning two rotational domains of the reconstruction are usually observed[107].

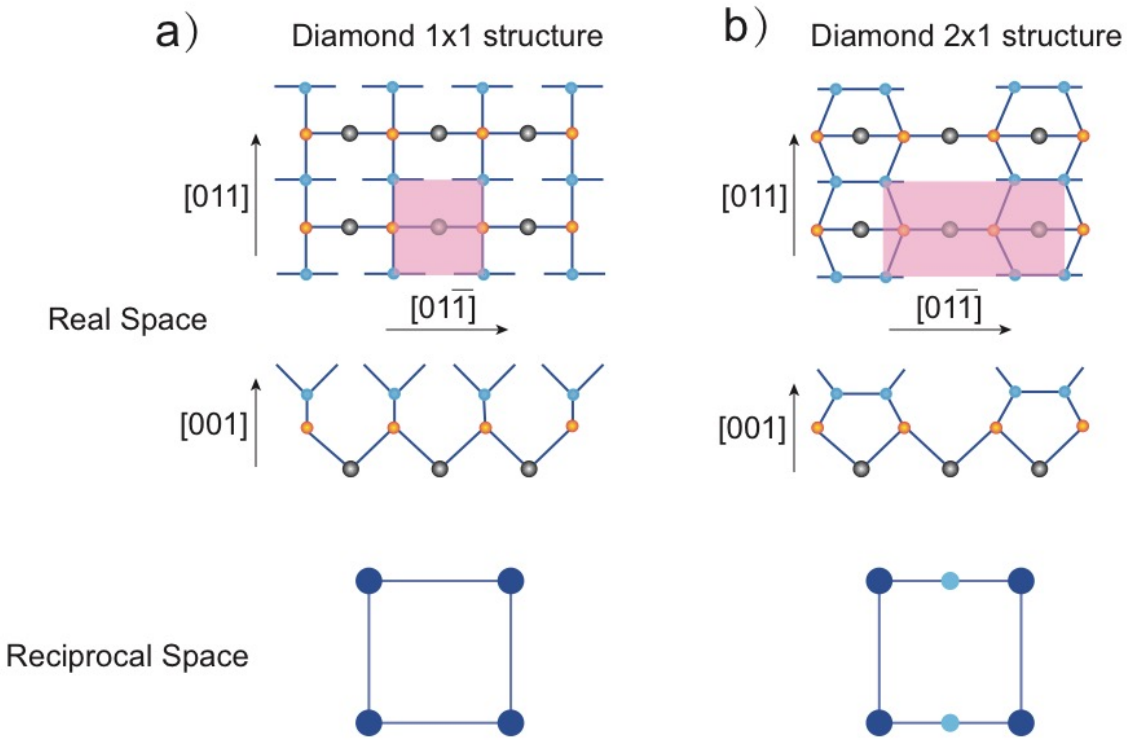

Figure 4.3 Schematic image (top and side view) of the three top most layers of carbon atoms of the ordered diamond (100) surface. a): the bulk terminated, unreconstructed 1X1 geometry. b): the 2x1 reconstructed geometry. The atoms subtended by pink shadow represent the unit cell of each structure.

4.1.3 Diamond Surface Terminations

The oxygen-terminated and hydrogen-terminated (O-/H-) diamond surfaces are the most widely studied due to their many potential applications. The surface properties of diamond depend on a combination of factors including the chemical species, surface roughness, surface reconstruction and the surface adsorbates. All of the above factors influence properties such as surface conductivity, surface dipole, work function and electron affinity. The electron affinity (χ) of diamond may cover a range of about 3 eV for the same diamond by varying the surface from fully hydrogenated C(100)-(*2×1*):H (χ=*−1.3* eV) to oxidized C(100)-(*1×1*):O (χ=*+1.7* eV), as reported by L. Ley[108]. In addition, the surface composition can be widely divergent when the surface is pretreated with different oxidization processes. For instance, S. Szunertis *et al.* found that the proportion of ether groups (C-O-C) varied from 6% to 14% then 29% on the diamond surface by using plasma oxidation, electrochemical oxidation and 55 min photochemical oxidation respectively [109]. It is possible to alter the physical and chemical properties of the diamond surface termination to tune for different diamond applications. For example, J. Macpherson *et al* demonstrated that the H-termination on highly boron-doped diamond (BDD) electrodes (~$10^{21}$$cm^{-3}$) is electrochemically unstable, an effect which depends on the doping concentration of diamond and the input potentials[110]. Although some progress for revealing the nature of the diamond surface termination has been made, the surface composition and structure change during the treating process, especially high temperature annealing, is still not fully

understood.

As shown in Figure 4.4, a model of the surface geometry of the ideal diamond C(100)-(1×1):O surface has been constructed using the Avogadro software package (details of the software seen in ref [111]) with spacing parameters obtained from [112]. The bond length of bulk diamond is set as 1.545 Å. The C(100)-(1×1):O structure was modeled with the co-existence of C-O-C and C=O groups. The C-O-C groups (so-called ether groups) are displayed in the 'bridge' configuration with a length of 1.484 Å. For the C=O groups (so-called ketone groups), the oxygen atoms are located on the top of the surface carbon atoms with a bond length of 1.19 $\mathring{A}$.

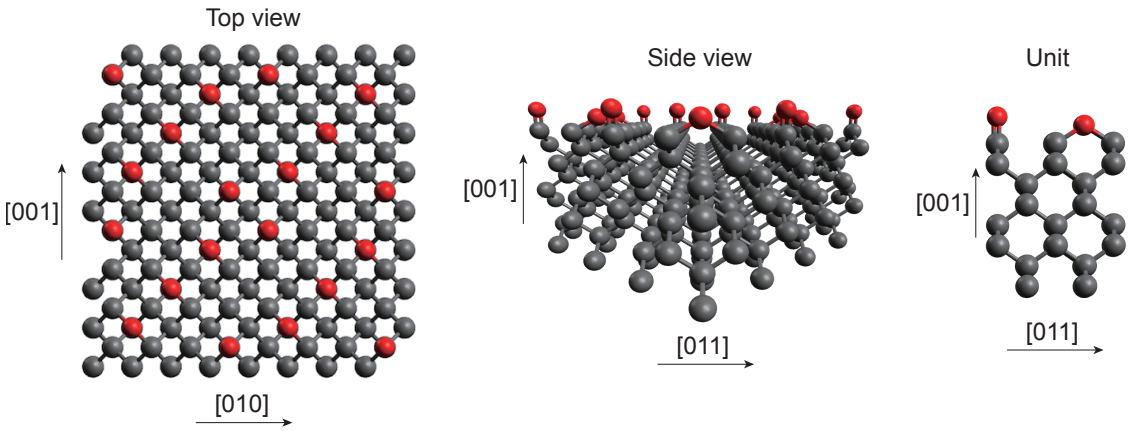

Figure 4.4 Shows the 1x1 surface geometry of the oxygen terminated (100) diamond surface. Oxygen atoms (red spheres) bond with the top layer carbon atoms (grey spheres) in two types, ether and ketone groups.

For the hydrogen-terminated (100) surface (shown in Figure 4.5), the surface carbon atoms are single bonded to adjacent atoms in dimer chains (bond length = 1.61 Å),

which show a 2×1 surface geometry. The hydrogen atoms are bonded to each of the atoms in the C-C pair. The C-H bond length is 1.11 Å and the distance between the two hydrogen atoms in a pair is 2.49 Å [112].

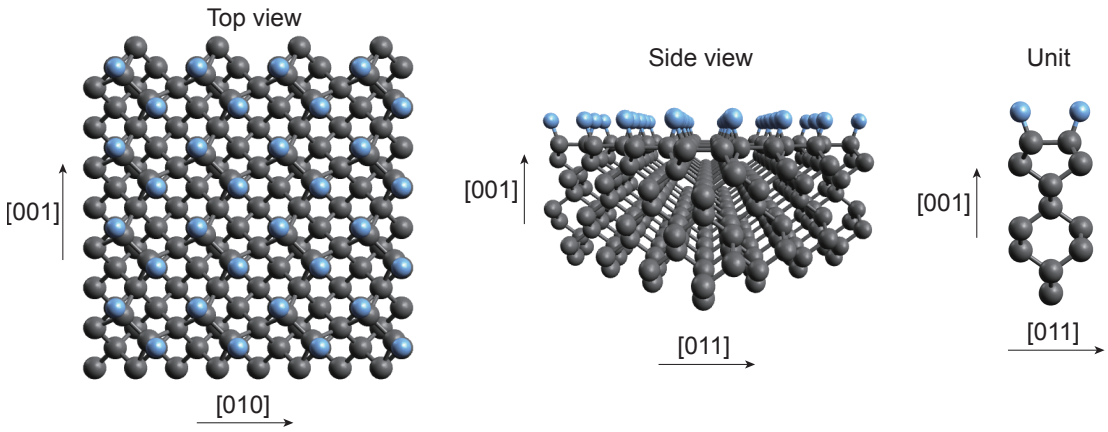

Figure 4.5 Shows the 2x1 surface geometry of the hydrogen terminated (100) facet diamond. Two hydrogen atoms (silver spheres) bonds with each top layer π-bonded dimers (grey spheres) as in single bonds.

The electron affinity χ is the energy difference between the conduction band minimum (E_{CBM}) and the vacuum level (E_{vac}), (equation 4.1.1),

$$\chi = \mathrm{E_{vac}} - \mathrm{E_{CBM}}$$

(*Eqn 4.1.1*)

The energy band diagram for the oxygen-terminated diamond surface is presented in Figure 4.6a. As a typical semiconducting surface, it exhibits a positive electron affinity (PEA). Since oxygen possess a higher electronegativity than carbon, the carbon-oxygen bond on the surface is polarized with a negative charge δ^-. In this case, the oxygen atoms would produce a potential step that locates the vacuum level above the CBM

increasing the energy barrier (χ) that would reduce the probability of low energy electrons escaping into the vacuum.

However, the electron affinity χ can be modified with different surface terminations. For example, the hydrogenated surface has a true negative electron affinity (NEA), one of the most interesting and unique features of diamond [113]. In contrast to the O-terminated surface, the hydrogen exhibits a lower electronegativity than carbon so that the polarity of the surface dipole is reversed, leading to E_{VAC} located below the CBM (Figure 4.6b). From the band diagram, the electron affinity χ can be derived from the absolute values of the work function ϕ and E_{Fermi}-E_{VBM}, according to equation 4.1.2.

$$\chi = \phi + (E_{Fermi} - E_{VBM}) - E_{gap}$$

(*Eqn 4.1.2*)

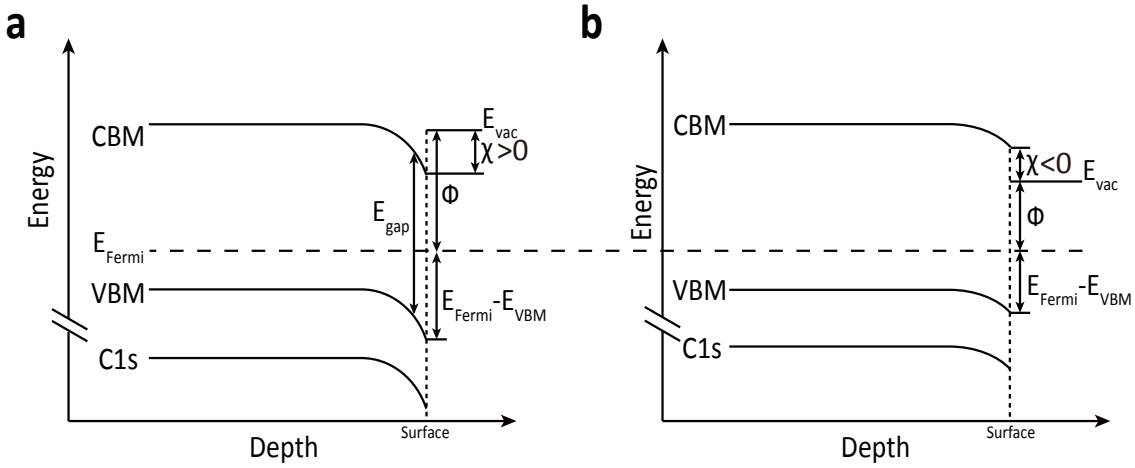

Figure 4.6 Band diagrams of the O-terminated diamond surface and the H-terminated diamond surface, as shown in (a) and (b) respectively.

4.2 Experimental

In this investigation, the transition process of surface composition and electronic structure of the oxygen-terminated diamond (100) surface was studied during high temperature annealing at 1000℃. The experimental data reveal the initial and final temperature of oxygen desorption and the surface band bending on the oxygen-terminated semiconducting diamond surface was found to vary by around 1 eV during the heating process. During the heating process, a transition of the surface structure from a C(100)-(1×1):O surface to C(100)-(2×1):H surface was observed.

4.2.1 Surface Pretreatment

The sample used was a moderately boron-doped (N_B ~ 2 x 10^{16} cm^{-3}) synthetic (100) CVD grown single crystal diamond (7.5 × 7.5 × 1.5 mm^3) provided by Element Six Ltd. The diamond surface topography was measured with a PSIA XE-100 non-contact mode atomic force microscopy (NC-AFM), which reveals a root-mean-squared roughness <0.2 nm, as shown as in Figure 4.7.

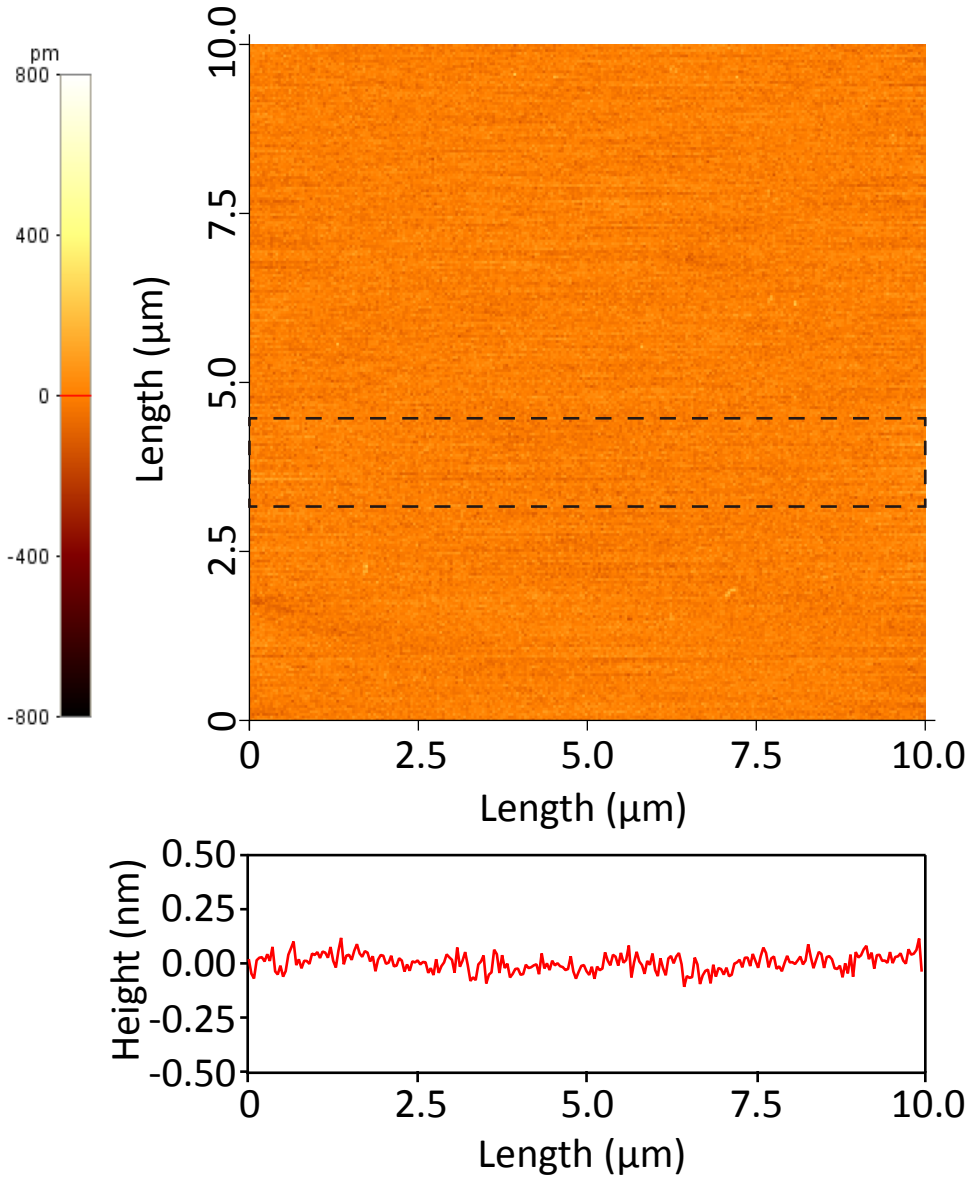

Figure 4.7 AFM profiles of the post-polished diamond (100) surface. Top: the topography image of a $10\times10\ \mu m$ area on flat diamond (100) surface; bottom: line profile extracted from the image by integrating the selected region (dash lines).

The O-terminated surface was produced with an acid-oxidizing method. The sample was heated in sulphuric acid (H_2SO_4, 98% purity, 10mL) for 10 minutes followed by the addition of potassium nitrate (KNO_3, 0.5g) and heating for a further 10 minutes. The diamond was then rinsed and sonicated in acetone, isopropanol, and de-ionized water

respectively, then dried using clean nitrogen gas before loading into the UHV system.

4.2.2 *In Vacuo* Annealing & Characterization.

The real-time data enables the recording of spectra in 2D block mode as shown in Figure 3.9, where each snapshot spectra in the time domain is arranged along the y-axis and the binding energy along the x-axis. This analysis process enables the extraction of specific information about the core level spectra, for example plotting the variation of peak position and intensity with time. Conventional XPS, UPS, and LEED measurements were also utilized in this work to determine the chemical composition and electronic structure of the surface.

4.3 Results and Discussion

4.3.1 XPS Study of the Oxygen-Terminated (100) Surface

To investigate the O-terminated diamond (100) surface, a series of conventional XPS surveys were performed while annealing the sample to different temperatures. Since high temperature annealing forms a Mo-carbide on the rear of the diamond sample, the sample is grounded and reliable drain current measurements can be taken (shown as in Figure 3.6). Figure 4.8 shows wide XPS survey spectra and the oxygen content on the acid oxygenated (100) surface measured at room temperature (red) and after annealing

cycles of 350 ℃ (blue) , 600 ℃ (green) and 1000 ℃ (orange).

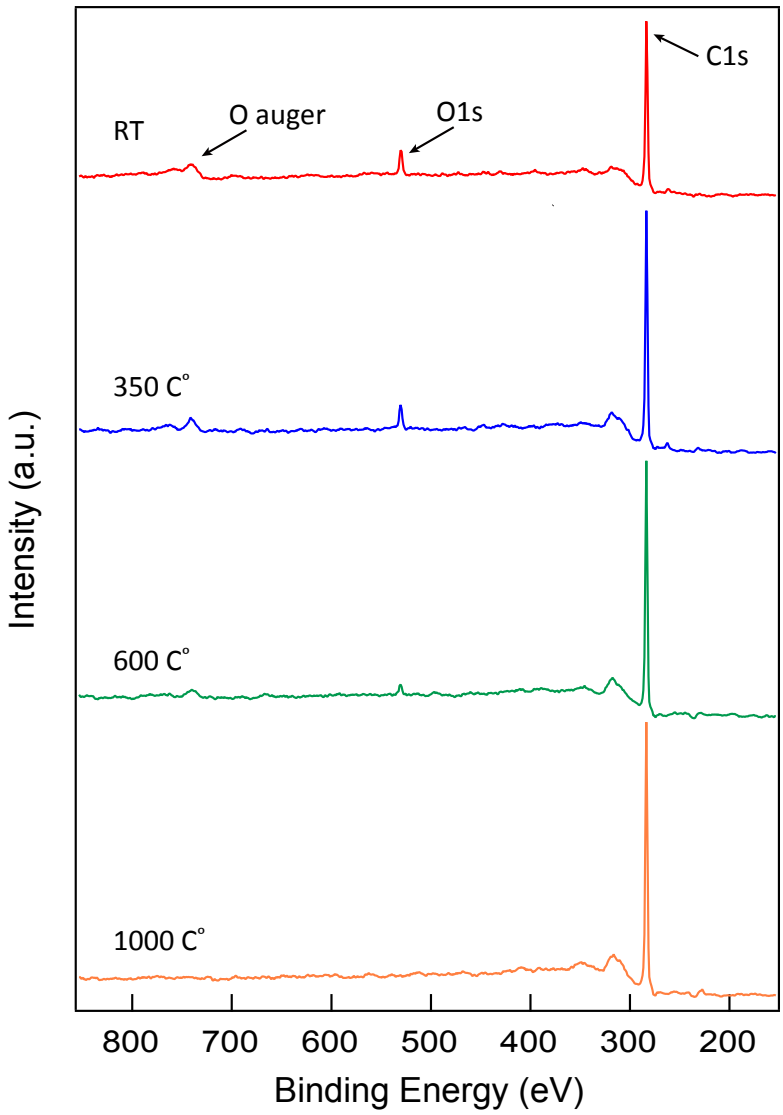

Figure 4.8 XPS wide spectra of the oxygen-terminated (100) surfaces measured at room temperature (23 ℃) (red), after annealing cycles at 350 ℃ (blue), 600 ℃ (green) and 1000 ℃ (orange).

	C1s (%)	O1s (%)
RT	93.9±0.1	6.1±0.1
350 ℃	94.3±0.1	5.7±0.1
600 ℃	97.4±0.1	2.6±0.1
1000 ℃	100	0.0

Table 4.3 Concentration of O1s and C1s derived from the XPS wide survey data.

The concentration of oxygen (ϕ_{oxygen}) was evaluated by the CasaXPS software from the widescans. This concentration can be converted into coverage of oxygen (C_{oxygen}) on the diamond surface, by using *Eqn 4.3.1*,

$$C_{oxygen} = \frac{\phi_{oxygen}}{\sum_{i=1}^{+\infty} e^{-\frac{id}{\lambda}}}$$

(*Eqn 4.3.1*)

where λ is the electron mean free path of C1s photoelectron, *d* is the layer separation distance in (100) faceted diamond and *i* is the number of layers. The result of this calculation is presented in Figure 4.9.

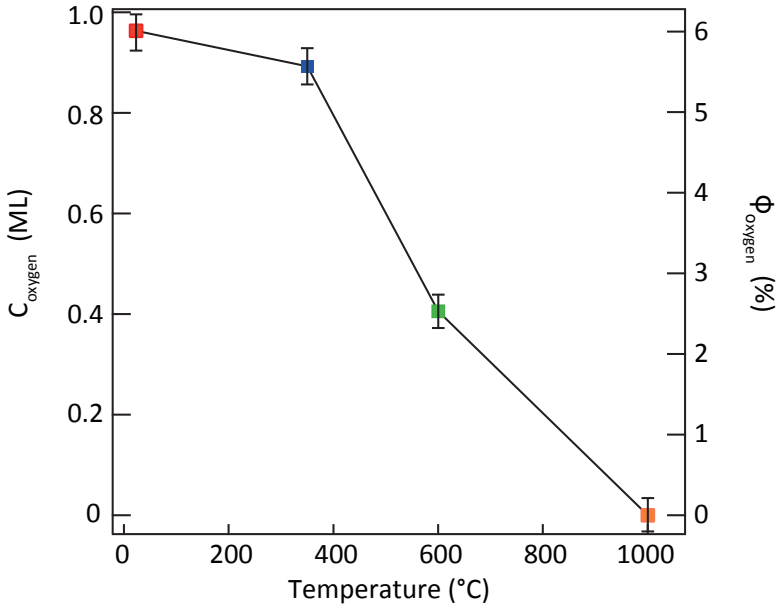

Figure 4.9 Oxygen concentration (ϕ_{oxygen}) and coverage (C_{oxygen}) of the surfaces calculated from the XPS wide spectra.

As shown in Figure 4.9, the oxygen coverage C_{oxygen} was 0.96 of a monolayer (ML) after chemical oxidization, using λ=1.4 nm [1] and d=0.89 Å [112], which then slightly decreased to 0.90 ML during the annealing cycle at 350℃. A sharp decreasing trend (from 0.89 ML to 0.4 ML) appeared during the next cycle from 350℃ to 600℃. The O1s peak disappeared after annealing to 1000℃, indicating that the oxygen was totally removed from the surface. Meanwhile, the C1s peak shows an obvious increase in intensity and narrower FWHM when the room temperature surface was heated to 350℃, implying that the contaminating sp^2 carbon was largely removed. The quantity of O1s only decreased slightly, implying the most of oxygen adsorbates were bonded to the surface carbon layer.

To further identify the oxygen species, Figure 4.10 shows detailed O1s and C1s core level

spectra which were recorded at room temperature (RT), and after annealing cycles to 350℃, 600℃, and 1000℃. All the spectra were fitted using a Sum Gaussian- Lorentzian (SGL) lineshape in CasaXPS after subtraction of a Shirley background. The intensities were normalized with respect to the maximum intensity of each core level. From the O1s spectra, three component peaks are extracted at 531.7±0.2 eV (blue) 530.4±0.2 eV (red) and 529.3±0.1 eV (green). Although little previous research could be found for identifying O1s spectra of the O-terminated diamond, according to the C1s spectra in figure 4.10, the three fitted components at 531.7 eV, 530.3 eV and 529.3 eV were discussed as ether (C-O-C) group, carbonyl (C=O) group and carboxyl (COOH) group respectively. C1s spectra were fitted with six different component peaks. For the oxygen-terminated diamond (100) surface, the peaks at the higher binding energy of main sp^3 peak are usually assigned to hydrocarbon (+0.5 to +0.8 eV) [114, 115] and oxidization states (ether group at +1.0 to +1.5 eV, carbonyl group at +1.8-2.5 eV, carboxyl group at +3.0 to +4.0 eV) [110, 116, 117], while the peak at lower binding energy is associated with sp^2 C-C (-0.9 to -1.4 eV) [109, 118]. In C1s profiles, the most intense component peak found at 284.5±0.1 eV (red) is attributed to the sp^3 C-C from the diamond bulk. The peaks at 285.4±0.1 eV (orange), 286.4±0.1 eV (green), 287.3±0.1 eV (purple), 283.3±0.1eV (blue) were assigned with C-O-C group, C=O group, COOH group and sp^2 C-C group respectively for spectra recorded at RT, 350℃, 600℃. However, a small peak at 285.2 eV (pink) suggests that a small amount of C-H appeared after the annealing cycle to 1000℃.

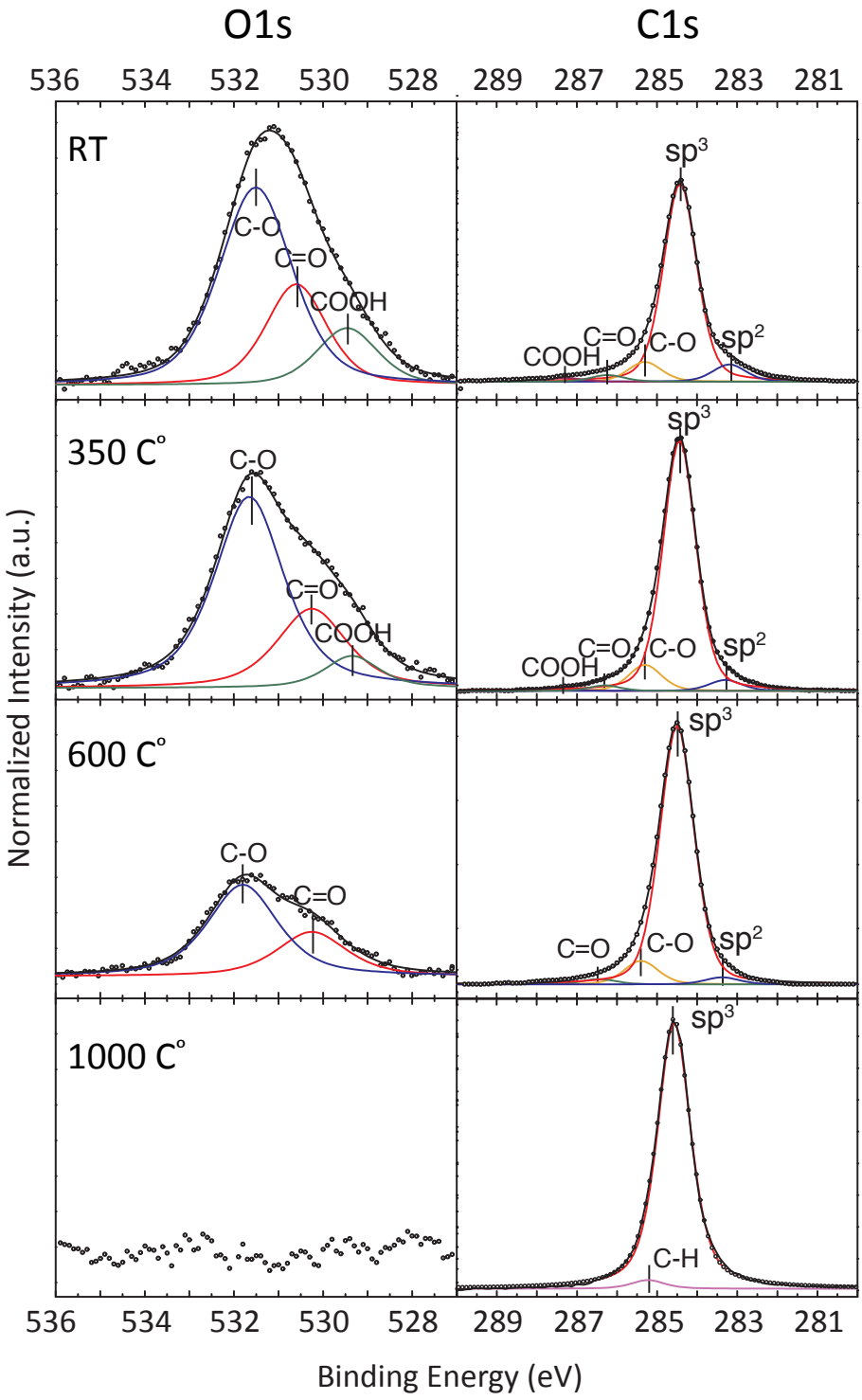

Figure 4.10 Core level XPS spectra for the oxygen-terminated diamond (100) surface measured at room temperature (23 ℃) and after annealing cycles at 350 ℃, 600 ℃ and 1000 ℃. Left: O1s core level spectra. Right: C1s core level spectra with peak fittings. The open symbols represent the experimental data; the colored lines represent fitted components; and the black lines represent the overall fit.

From the O1s core level spectra, comparing the surfaces at RT and after 350 ℃ annealing process, the ratio of C-O:C=O:COOH varied from 60%:25%:15% to 62%:28%:10%, indicating that the COOH was preferentially desorbed below 350 ℃ while C-O and C=O persist on the diamond surface. After heating to 600 ℃, the COOH was totally removed while the intensity of both the C-O and C=O groups was reduced. No oxygen was detected after the surface was heated to 1000℃. In the corresponding C1s spectra, the sp2 carbon concentration reduced from 6.9% to 3.7% during heating from RT to 350 ℃, then to 0.78 % at 600 ℃. This implies that the annealing process below 350 ℃ is sufficient to remove the sp^2 contamination. A small component appeared at 285.2 eV in the C1s spectra, which is identified as a hydrocarbon peak. The residual hydrogen in the vacuum chamber could be a product of the boron-nitride heater outgassing above 900 ℃. This is further discussed with reference to UPS and LEED results.

	Core Level/ Component		Position (eV)	FWHM (eV)	%	Lineshape
RT	C 1s	sp^3	284.4	1.00	81.6	SGL(60)
		sp^2	283.2	1.00	6.90	SGL(60)
		C-O	285.3	1.00	6.96	SGL(60)
		C=O	286.3	1.00	3.01	SGL(60)
		COOH	287.3	1.00	1.53	SGL(60)
	O 1s	C-O	531.5	1.65	60.03	SGL(60)
		C=O	530.6	1.65	24.90	SGL(60)
		COOH	529.4	1.65	15.07	SGL(60)
350 ℃	C 1s	sp^3	284.4	0.97	85.98	SGL(60)
		sp^2	283.3	0.97	3.70	SGL(60)
		C-O	285.3	0.97	6.58	SGL(60)
		C=O	286.3	0.97	2.97	SGL(60)
		COOH	287.4	0.97	0.77	SGL(60)
	O 1s	C-O	531.6	1.75	62.25	SGL(60)
		C=O	530.3	1.75	27.96	SGL(60)
		COOH	529.3	1.75	9.79	SGL(60)
600 ℃	C 1s	sp^3	284.5	0.98	94.45	SGL(60)
		sp^2	283.4	0.98	0.78	SGL(60)
		C-O	285.4	0.98	3.75	SGL(60)
		C=O	286.5	0.98	1.02	SGL(60)
	O 1s	C-O	531.8	1.78	68.71	SGL(55)
		C=O	530.3	1.78	31.29	SGL(55)
1000 ℃	C 1s	sp^3	284.5	0.96	98.79	SGL(65)
		C-H	285.2	0.96	1.21	SGL(65)

Table 4.4 Fitting parameters of the O1s and C1s core level spectra.

4.3.2 UPS characterization on the annealed surfaces

UPS and LEED were employed to determine the surface composition after annealing the diamond at $1000℃$. Figure 4.11 shows the UPS spectra for on the oxygen-terminated surfaces. The acid oxygenated (100) surface was treated with annealing cycles up to $350\ ℃$ (blue), $600\ ℃$ (green) and $1000\ ℃$ (orange), and then measured with UPS at room temperature between each heating cycle using a Helium(I) source (photon energy $h\upsilon$ = 21.19eV). The Fermi level was calibrated at 0 eV binding energy position with reference to a Ta faceplate on the sample stage. Figure 4.11b and Figure 4.11c shows the definition of the secondary electron peak cut-off and valence band maximum values. The electron affinitiy for each surface was calculated using *Eqn 4.1.2*.

$$\chi = (h\nu - E_{sec}) + E_{VBM} - E_{gap}$$

(*Eqn 4.3.1*)

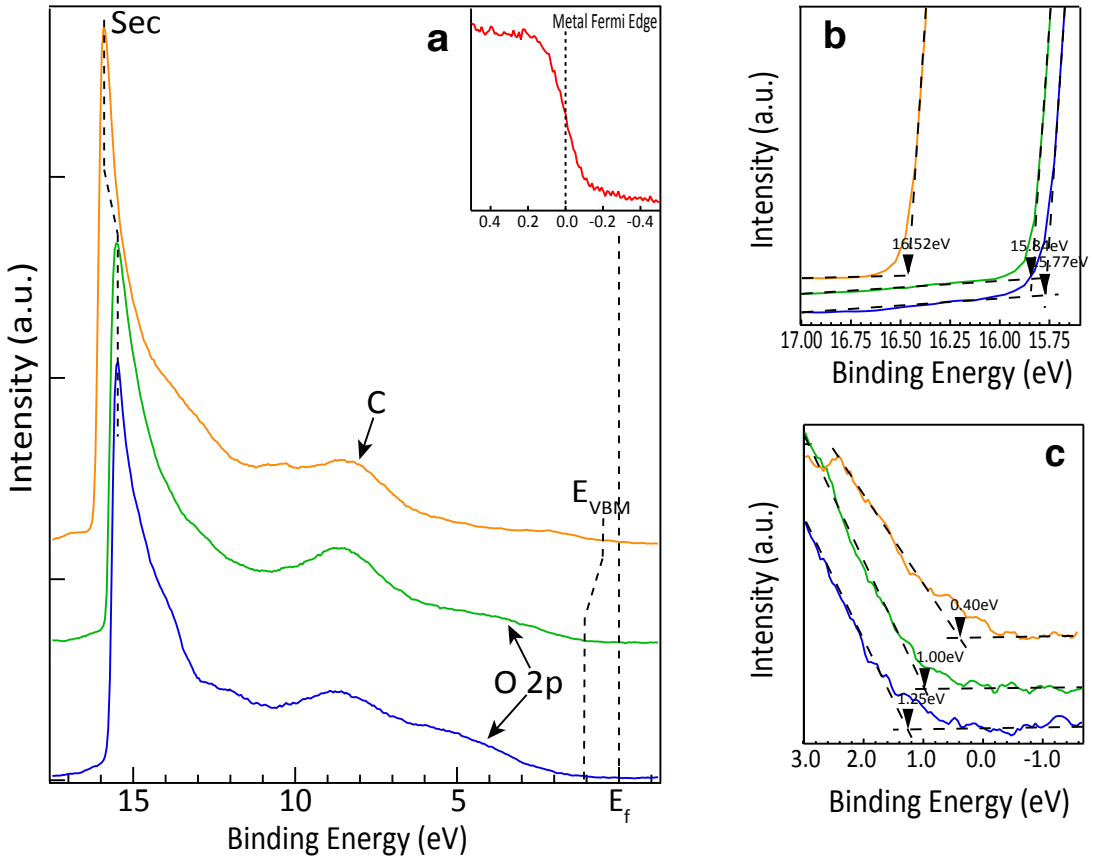

Figure 4.11 Valence band spectra for the oxygen-terminated diamond (100) surface: **(a)** wide-scan UPS spectra of oxygen-terminated (100) surfaces following annealing cycles at 350℃ (blue), 600℃ (green) and 1000℃ (orange). The Fermi energy level (inset) was calibrated using the metal faceplate; **(b)** High-resolution spectra of the secondary electron cut-off of the three surfaces; **(c)** High-resolution spectra of the valence band maximum (VBM) for each of the three surfaces.

	E_{VBM} (eV)	E_{Sec} (eV)	ϕ (eV)	χ (eV)
350 ℃	1.25±0.02	15.77±0.02	6.67±0.02	1.17±0.02
600 ℃	1.00±0.02	15.84±0.02	6.35±0.02	0.85±0.02
1000 ℃	0.40±0.02	16.52±0.02	5.07±0.02	-0.43±0.02

Table 4.5 Work function ϕ and electron affinity χ of the surfaces, derived from the UPS data. The diamond band gap is taken as 5.5eV.

From the wide-scan spectra (Figure 4.11a), it can be seen that the secondary electron peak is shifted towards higher binding energy during annealing from 350℃ to 1000℃, while the valance band maximum (VBM) is shifted 0.5-0.7eV towards the Fermi level. The increasing spectral width (E_{sec} - E_{VBM}) indicates that a reduction of the positive electron affinity χ has occurred on the surface. The feature indicated at around 4.5-5.0 eV is associated with the O2p state [119]. This feature was attenuated and the carbon state feature at 8-9 eV became narrower after 1000℃. In Figure 4.11b-c, the cut-off of the low kinetic energy (E_{SEC}) and VBM (E_{VBM}-E_{Fermi}) has been determined. Some groups have reported that hydrogen adsorption on (100) facet diamond samples affects the Fermi level pinning position at the surface, with typical values between 0.3 and 1 eV [25, 108]. Figure 4.11c shows that the VBM has shifted from 1.28 to 0.40eV during the annealing process. The values of work function ϕ and electron affinity χ presented in Figure 4.12 suggests a final state of the surface with a negative electron affinity of -0.4eV. All of these features indicate that a partially hydrogen-terminated (100) surface was produced after heating to 1000℃.

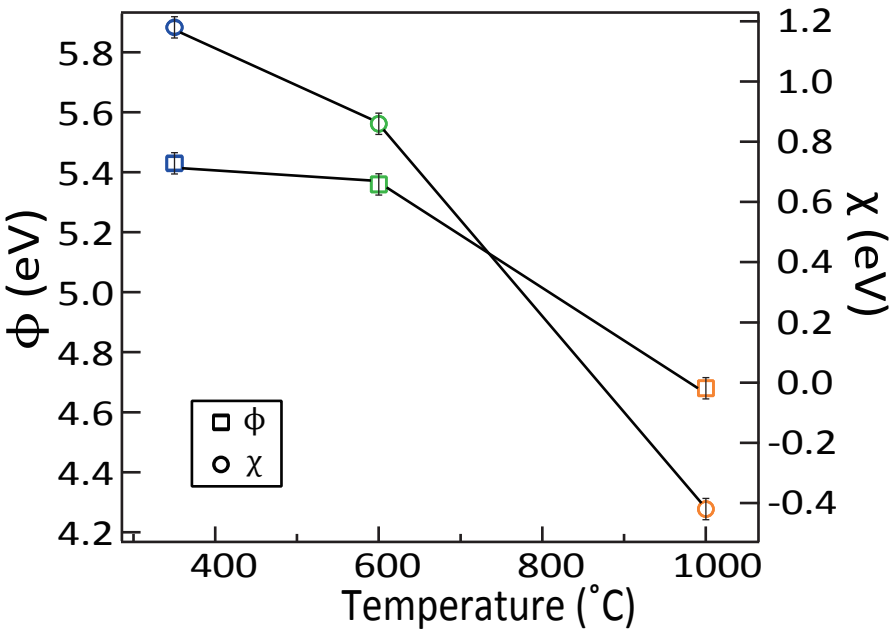

Figure 4.12 Variation of the surface work function (ϕ) and electron affinity (χ) with temperature, evaluated from the UPS spectra.

As shown in Figure 4.13, the structure of the surfaces annealed at $350\,℃$ (a) and at $1000\,℃$ (b) was monitored with LEED. It shows that the $1000\,℃$ vacuum annealing has converted the oxygen-terminated 1×1 geometry into a 2×1 geometry. It has been reported that the hydrogen free reconstructed 2×1 surface has a PEA and the C(100)-(2×1):H surface has a NEA by many experimental and theoretical results[25, 120]. Combined with UPS result in Figure 4.12, it confirms that the surface has converted into a C(100)-(2×1):H after annealing to $1000\,℃$.

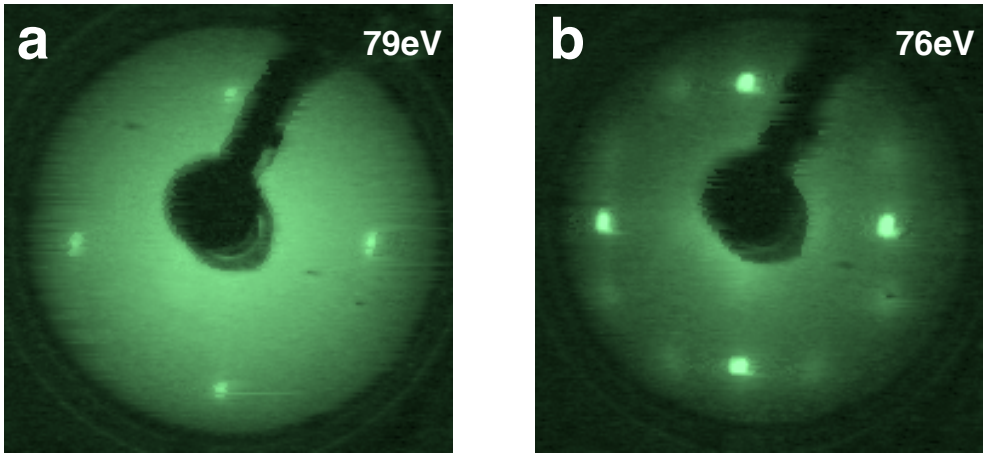

Figure 4.13 LEED patterns for the oxygen-terminated surfaces: **(a)** annealed to 600℃; **(b)** annealed to 1000℃.

4.3.3 Real-time Monitoring on the O-terminated surface during High Temperature Annealing

Deriving the electron affinity χ from the spectral width in UPS measurements has its limitation; for example the determination of the VBM with an accuracy better than 0.05 eV is challenging in UPS. Moreover, a reliable value for the vacuum level is difficult to determine from the low energy cutoff of the spectra since the spectral shape depends sensitively on the analyzer characteristic[108]. Thus, utilizing REES provides another way for revealing surface electronic structure regime as it can determine variation of surface composition during the whole heating process. REES therefore provides a useful and robust method for measuring the electronic properties of materials.

In this work, real-time measurements were performed on the acid-oxidized (100) diamond surface during annealing cycles at 310℃, 620℃ and 900℃. Two-dimensional

images of real-time spectra for C1s core level and O1s core level are shown in Figure 4.14a and Figure 4.14b respectively. These images were collected during a heating cycle from room temperature to 900℃. Each row in the image is a snapshot spectrum of the core levels. The time difference between each spectrum is 20s.

Figure 4.14c shows the O1s core level intensity during the heating. The heating process is divided into four different stages according to the oxygen intensity, RT-360℃ as stage 1, 360℃-610℃ as stage 2, 610℃-700℃ as stage 3, 700℃-900℃ as stage 4. The intensity remained at the initial level during stage 1, implying that the oxygen was strongly bonded on the diamond surface below 360℃ and therefore did not desorb. Stage 2 is associated with a large attenuation (more than 50%) of the O1s peak intensity as shown in Figure 4.14b and Figure 4.14c, which is consistent with the XPS results that show the oxygen coverage reduced from 0.96 ML to 0.42 ML after annealing to 600℃. An intensity plateau appeared during stage 3 in Figure 4.14c, indicating that the oxygen desorption stopped for some reason. After stage 3, the O1s peak resumed its attenuation until it was almost the same intensity as the spectral background at the end of stage 4. The real-time data of the O1s peak is in broad agreement with the conclusion of conventional XPS study. Moreover, it presents the oxygen desorption process more specifically and comprehensively during the overall annealing process.

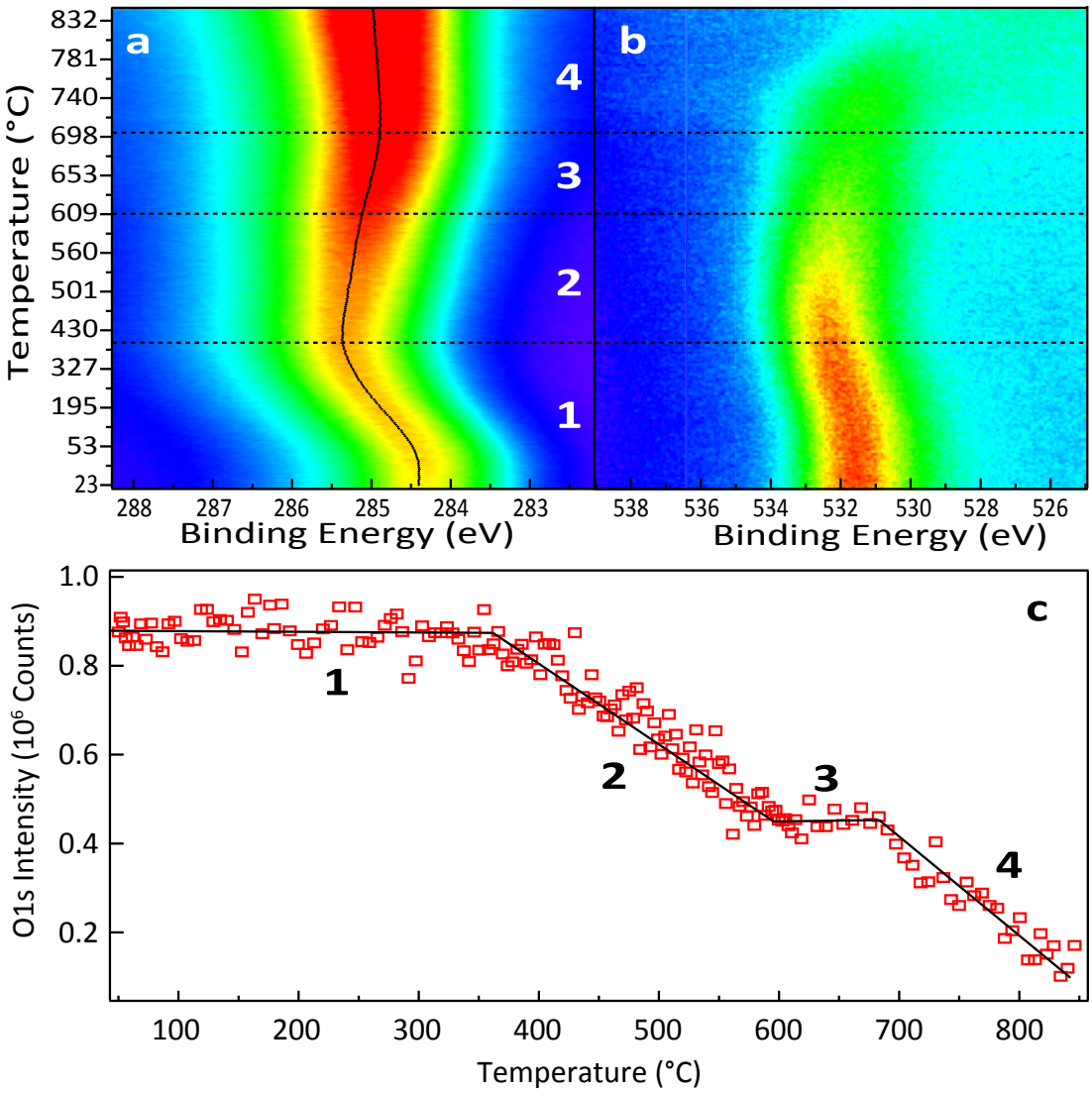

Figure 4.14. Real-time 2D block images of the C1s core level snaphshots(a) and O1s core level snapshots(b) during the heating process from room temperature to 850℃. The intensity of the spectra increases as the color ranges from blue to red. (c) The O1s peak intensity variation during the same heating process. The open squares represent the raw data of O1s intensity; the solid line indicates the overall trend of peak intensity.

In addition to the intensity analysis, the variation in peak position of C1s core level spectra in Figure 4.14a was also extracted from the fitting of each spectrum with a Voigt function, to provide the behavior of the electronic structure during the heating process. It indicates that the C1s peak position was shifted to a higher binding energy in stage 1 and then back towards lower binding energies above 350℃. To explain the shift of peak

position during the annealing process, REES was performed on the acid oxygen-terminated surface during annealing cycles at 320℃ and 620℃, as shown in Figure 4.15a and Figure 4.15b respectively.

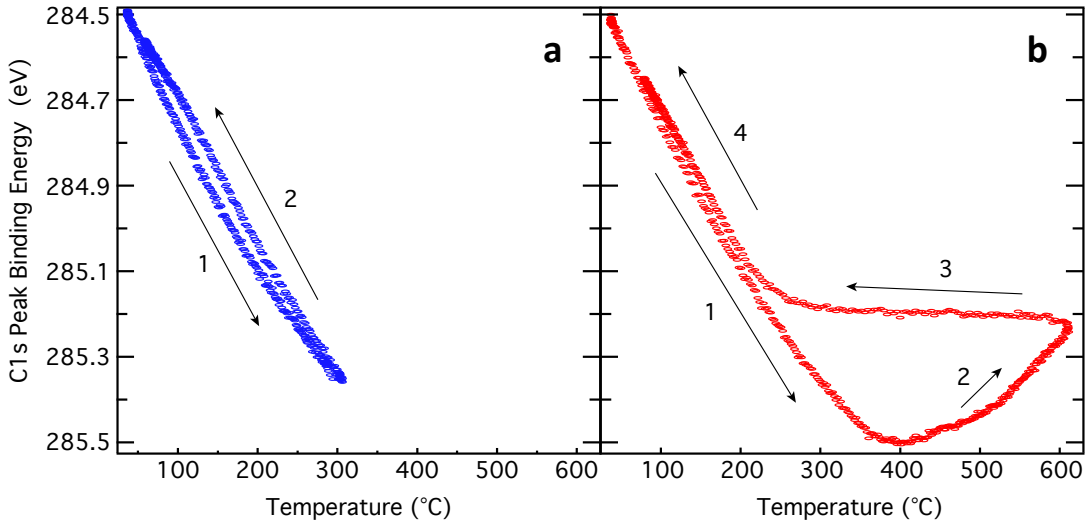

Figure 4.15 (a) The C1s peak position curve during the annealing cycle with 300 ℃. Stage 1 represents the heating process, while stage 2 shows the cooling process. (b) The C1s peak position curve during the annealing cycles with 600 ℃. Stage 1-2 represent the heating process, while stage 3-4 show the cooling process.

The photovoltage effect was modelled by Hecht [121] and was successfully used to clarify contradictory results on semiconductor-metal barrier heights. For diamond it has been reported that a photo-induced voltage could persist for several hundred degrees above room temperature on the moderately hydrogenated BDD surface[122]. Since charge-pairs are created within the depletion region, the charge accumulation at the surface would generate a photovoltage that flattens the bands. Similarly, a surface photovoltage has been discovered on this oxygenated BDD surface, although the surface dipole created by oxygen adsorbates is opposite to that of the hydrogenated surface in

our previous work[122]. This effect is generally a low-temperature effect as the holes are unable to overcome the barrier at low temperature. However the Hecht model was unable to account for the surface photovoltage persisting above 300 K since the thermal energy should be enough to overcome the barrier. Figure 4.15a shows the reversible peak position of C1s was continuously shifted from 284.5 eV to 285.4 eV. However, in Figure 4.15b, the situation is more complex during higher temperature annealing to 600 ℃. Although the temperature was still increasing steadily, the peak position began to reverse toward the lower binding energy at 400 ℃. Referring with our temperature-dependent surface photovoltage model which has been presented previously[122], the surface photovoltage on this moderately doped diamond surface reduced and became negligible at around 380 ℃. It shows a maximum peak shift at +1.0 eV indicating the true band bending position for this oxygenated semiconducting surface. During stage 2 in Figure 4.15b, the true band bending energy decreased due to oxygen desorption above 400 ℃. During the cooling process, the true band bending was pinned at +0.7 eV until temperature dropped to around 300 ℃, when the surface photovoltage reappeared.

The pause in oxygen desorption during stage 3 in figure 4.14c presents an interesting problem. Clearly, applying more thermal energy during this regime does not cause any more oxygen to desorb until the temperature of the sample exceeds 700℃. With no changes to the sample environment during this stage, the thermal energy provided to

the sample must be contributing to another separate process, thus inhibiting oxygen desorption momentarily. To investigate this regime further, the C1s and O1s peak positions and intensities during annealing from 440℃ to 850℃ were extracted from the data in figure 4.14, to provide information about the C1s core level during oxygen desorption (Figure 4.16a). A theoretical study has reported that the subsurface carbon layer may be displaced and sp^3 carbon bonds could be broken at around 700℃, providing a nucleation point for the surface reconstruction or graphitization[123]. As shown in Figure 4.16b, the intensity of the C1s peak kept increasing while the oxygen desorption stopped between 610℃ and 700℃. In addition, the peak shift rate of the C1s peak to lower binding energies increased in this stage before stopping and shifting back toward higher binding energies at 700℃, which indicates the variation of the band bending was different from below 600℃. This may relate to the subsurface carbon layer dislocating and reconstructing the bonding structure in the near-surface region between 610℃ and 700℃. The subsurface layer adsorbs most of the thermal energy for breaking the C-C bond and thus inhibits oxygen desorption until enough power is applied to the surface. This interpretation appears to be consistent with the theoretical study by B. Segall *et al*[123]. Additionally, recent simulation work has shown that the electron spin coherence time of near-surface NV centers in diamond significantly increases following annealing at 650℃ in vacuum for one hour. This also suggests that the thermal energy could be adsorbed by the subsurface carbon and has significant effect on the NV properties of diamonds in this temperature region. More importantly,

this is the first real-time data that reveals competing surface processes during high temperature annealing.

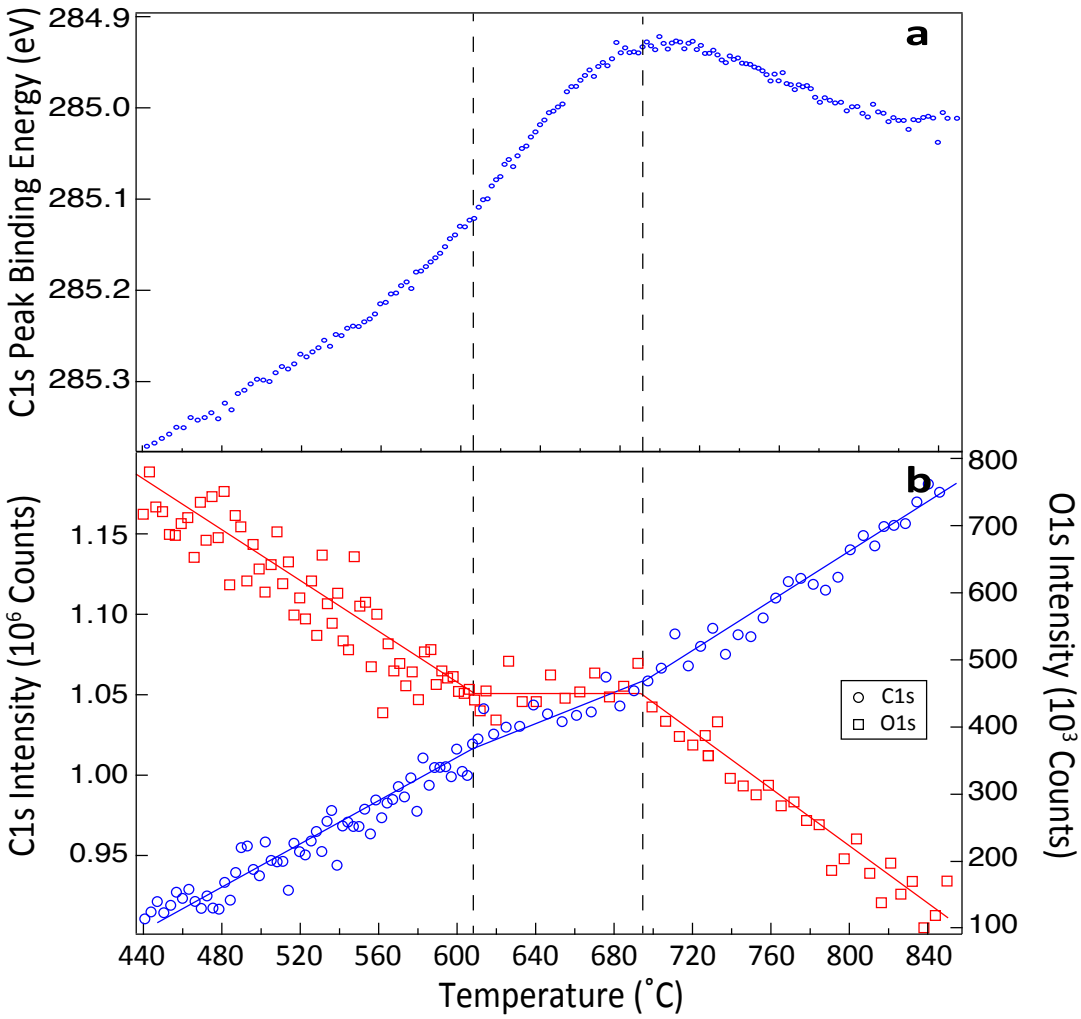

Figure 4.16. (a) Variation of the C1s peak position with temperature during heating from room temperature to 850 ℃ (b) The C1s core level (open circles) and O1s core level (open squares) intensity curve plotted again heating temperature. Solid lines indicate the trend of intensity variation.

Another set of experiments were designed to investigate the different desorption regions on the oxygen terminated surface. The sample was treated with the oxidizing

acid etch, then heated to specific temperatures where the REES of the O1s core level was measured (350℃ for 1 hour, 520℃ for 1 hour, 550 ℃ for 1 hour, 650 ℃ for 1 hour and 800 ℃ for 30 minutes). The results are shown in Figure 4.17. A clear trend can be observed from both the REES 2D block and the plotting of O1s peak intensity in Figure 4.17 and this is in agreement with the results shown in Figure 4.14. The surface oxygen stops desorbing at 650℃, which corresponds to the region from 610℃ to 700℃.

350˚C

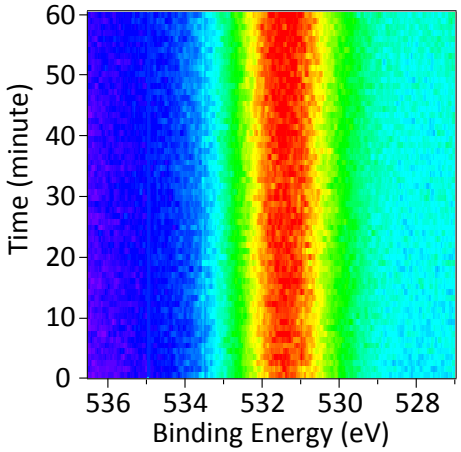

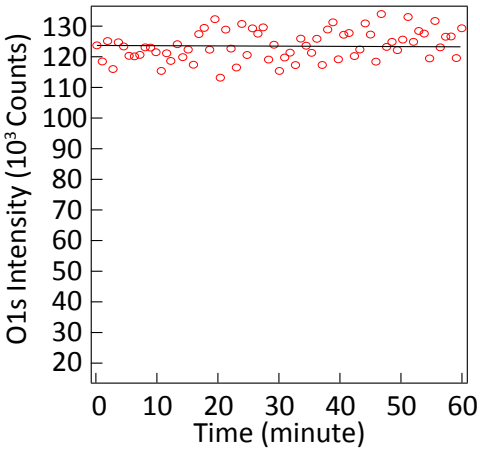

520˚C

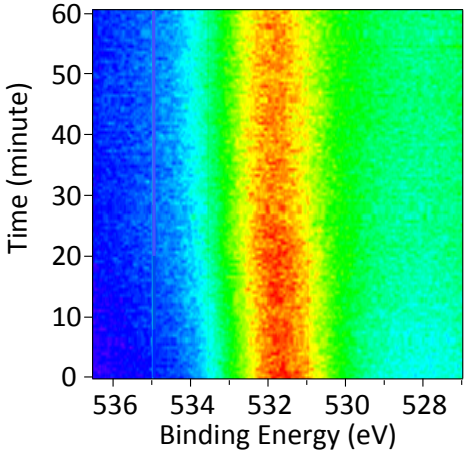

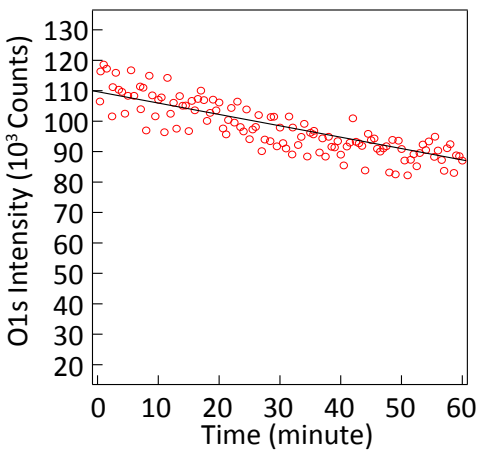

550˚C

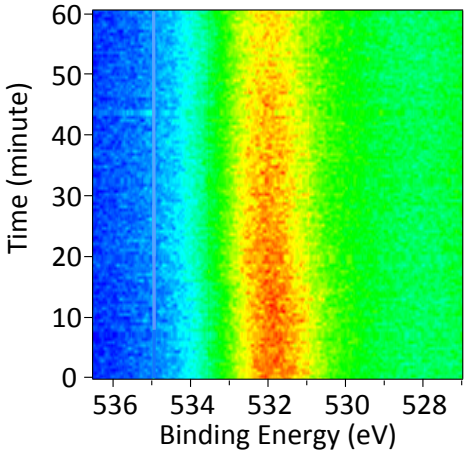

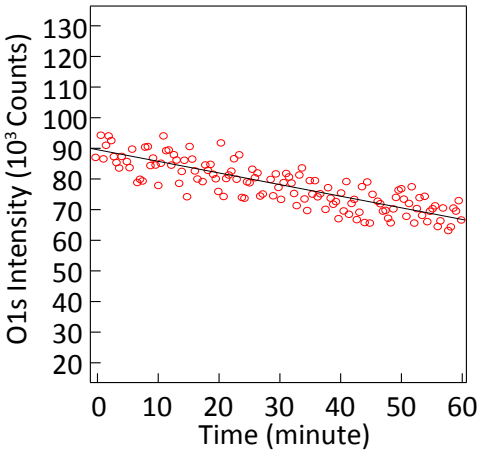

650˚C

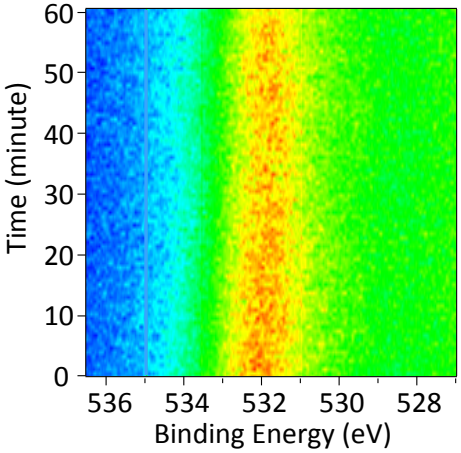

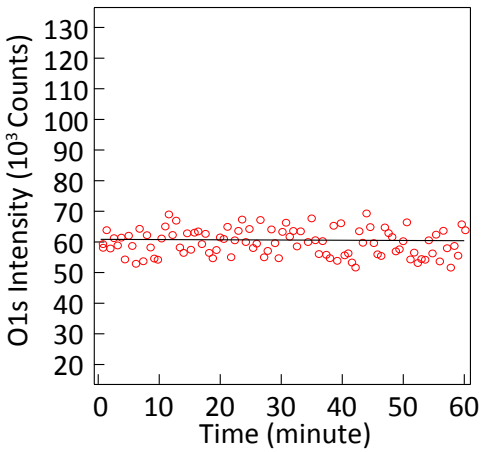

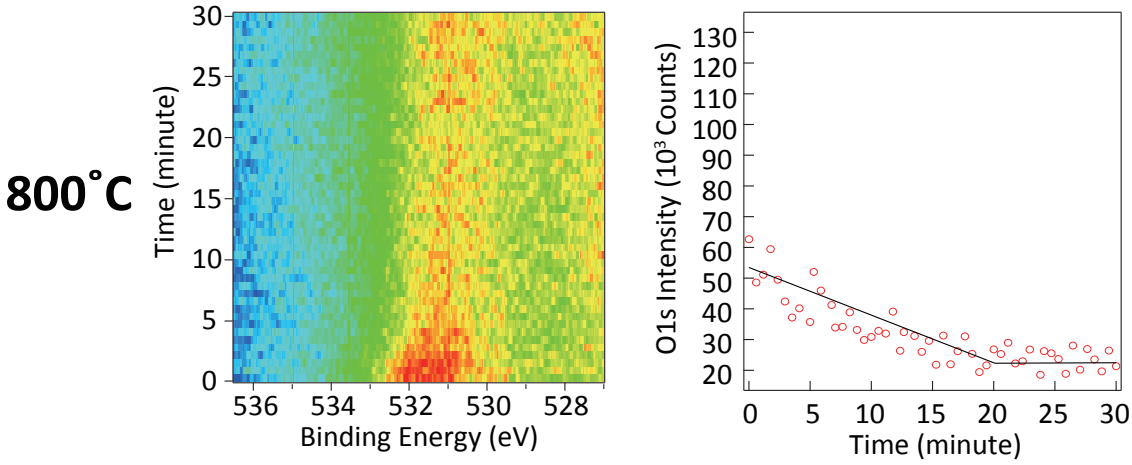

Figure 4.17 Left part: REES 2D block of O1s core level measured with consistent temperatures; right part: The core level intensity vs time. Solid lines indicate the trend of intensity variation

From these data, the activation energy of oxygen desorption can be estimated according to the Arrhenius relationship (Eqn 4.3.2)

$$k = Ae^{-\frac{E_a}{k_B T}}$$

(*Eqn 4.3.2*)

where E_a is as the activation energy, k_B is as the Boltzmann constant, *A* is constant, *T* is the temperature (in Kelvin), *k* is the reaction rate which can be estimated from the core level intensity attenuation along with the heating time. To determine E_a, *Eqn 4.3.2* can be written as,

$$\ln k = -\frac{E_a}{k_B}\left(\frac{1}{T}\right) + \ln A \qquad (Eqn\ 4.3.3)$$

Therefore the activation energy E_a can be determined from the gradient in Figure 4.18, which gives a activation energy E_a of oxygen desorption as 0.5±0.23 eV.

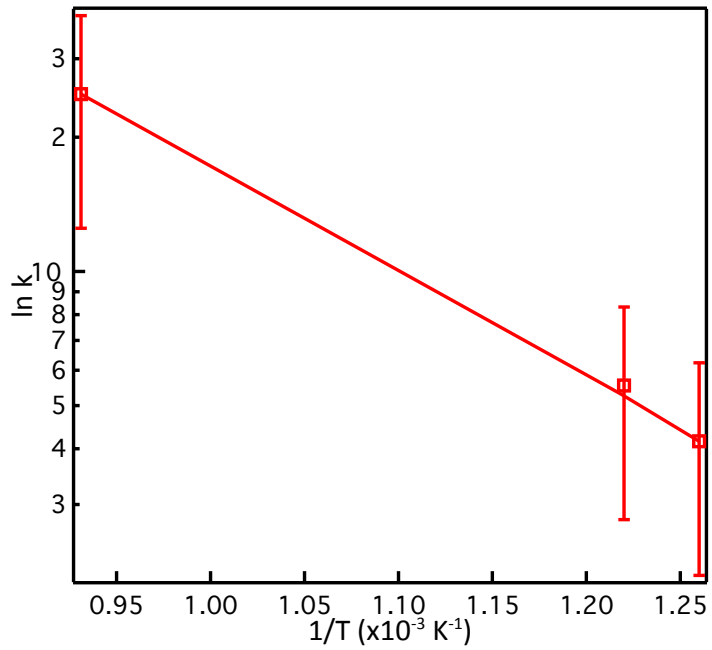

Figure 4.18 Plotting of lnk vs 1/T, data was evaluated from Figure 4.17.

4.4 Chapter Conclusion

In this chapter, the surface chemical composition and electronic structure of the oxygen-terminated diamond (100) surface was investigated during a high temperature annealing process. The process of oxygen desorption was well illustrated with real-time photoelectron spectroscopy. It was shown that the oxygen adsorbates desorb significantly above 350℃. However, oxygen desorption was suspended between 610℃ and 700℃. It is proposed that this is associated with subsurface structure variation that occurrs at this stage in the near-surface region. Oxygen was totally removed from the surface at ~850℃. However, due to the existence of background hydrogen at high temperature in the vacuum chamber, the oxygen free surface was finally turned into a

hydrogenated (2×1) surface with a NEA, which was confirmed by UPS and LEED. Moreover, a surface photovoltage was found on the oxygenated semiconducting diamond (100) surface, which attenuated the band bending values by as much as 1.0 eV at room temperature. From measurements at fixed temperatures, the activation energy of desorbing oxygen from (100) diamond surface was estimated as 0.5 eV. This work reveals the mechanism of surface composition and electronic structure change of the (100) diamond surface during annealing process. In addition, recent studies have found that the subsurface effect could have a significant influence on the NV center, meaning this work has a relevance for the development of diamond-based spintronic and electric devices. However, more experimental and theoretical studies are still needed for a complete understanding of the subsurface chemical and physical changes during high temperature annealing.

CHAPTER 5 – 5FU ON DIAMOND SURFACES

5.1 Introduction

The chapter presents an investigation of using the diamond surface as the biochemical coating materials for drug transportation, especially for Fluorouracil (5-FU) which is a widely used drug in the treatment of conditions such as leukemia and bowel cancer[124, 125]. 5-FU ($C_4H_3N_2OF_2$) acts to inhibit thymidine, a nucleoside required for DNA replication and necessary for cancer cells to reproduce [126].

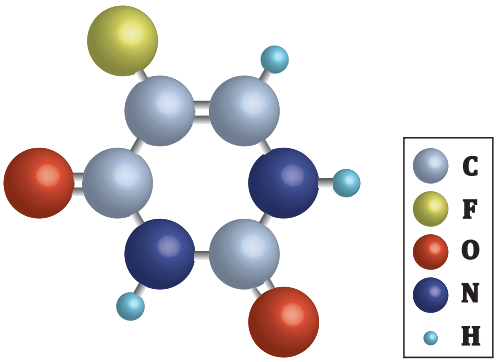

Figure 5.1 Shows structure of the 5-FU molecule, which is composed of C, H, F, N and O in a ratio 4 : 3: 1 : 2 : 2 ($C_4H_3FN_2O_2$).

During the cancer treatment process, it is usually delivered through catheters, which are made of polymeric materials such as polyurethane and silicone [127] and are prone to degradation when in contact with bodily fluids or aggressive drugs such as 5-FU [128]. Therefore the catheters are often coated with anti-bacterial protecting films to reduce the degradation of the polymers, for example noble metals (in particular silver and argentic alloys [129, 130]). However the interaction between the molecules and the

catheter surface is not normally considered, but it has recently been shown by x-ray photoelectron spectroscopy (XPS) that a silver surface can catalyse the dissociation of the 5-FU molecule to release HF, in a plausible reaction process: 5-FU→HF+$C_4H_2N_2O_2$. While the reaction is observed on the Ag surface it is not seen on a graphene substrate[131]. This may results as additional complications for patients and substantially-increased medical costs. Graphene and diamond-like carbon (DLC) coatings are studied and used in medical applications [131-133] , because their resistantance to chemical corrosion and biologically compatible. The process is illustrated schematically in Figure 5.2a and the chemical interaction is inferred from the XPS core level data presented in Figures 5.2b and 5.2c by F. Mazzola *el al[131]*. The molecular films were deposited *in vacuo* on cooled substrates and the XPS spectra monitored during heating to 55℃. For the silver surface (Figure 5.2b), a low binding energy component in the N1s spectrum and a preferential loss of F during heating indicates the catalytic release of HF and the formation of a new N environment. On graphene (Figure 1c), the molecule remains intact and desorbs entirely at 55℃ leaving a clean surface.

The properties of surface termination of the (100) facet diamond have been discussed in the last chapter. When the diamond surface is terminated by different elements, the surface geometry, electron affinity and surface dipole can be significantly different. In order to compare diamond as a coating material, the adsorption of 5-FU on the oxygen and hydrogen terminated diamond (100) surfaces has been studied in this investigation.

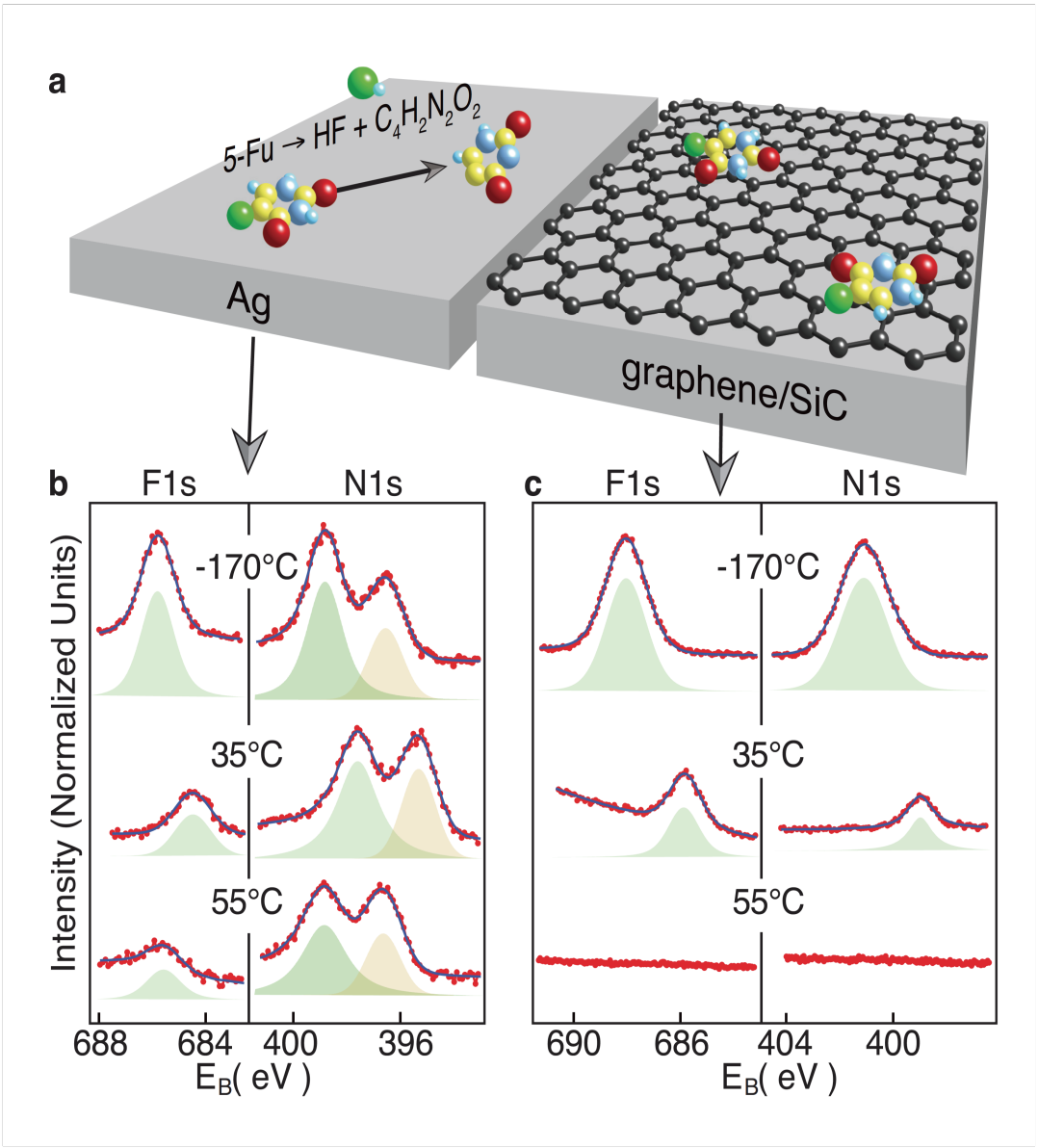

Figure 5.2 The interaction of 5-FU with graphene and silver: (a) Schematic representation of 5-FU in contact with Ag and graphene surfaces. (b) Temperature-dependent F1s and N1s XPS measurements of 5-FU on Ag. (c) Temperature-dependence for 5-FU on graphene. (Taken from reference [131])

5.2 Experimental

5.2.1 Surface Termination

The clean oxygen-terminated (100) surface was prepared with an oxidising acid etch

(same method as described in Chapter 4), followed by *in vacuo* annealing to 300℃ to remove surface contamination. Figure 5.3a shows a wide XPS survey of the oxygen-terminated surface. The quantification of XPS widecan shows an oxygen concentration at 6.1% on this surface. According to Eqn 4.3.1, it indicates that a monolayer coverage of oxygen has been obtained on the surface.

The hydrogen-terminated (100) surface has been described in the last chapter and this surface was produced by annealing to 1000℃ to remove oxygen, and then treated with an *in situ* exposure to a non-thermal H* plasma source (the details has been described in Chapter 3). Figure 5.3b shows a wide XPS survey of the hydrogen-terminated surface. With XPS measurement, it is impossible to detect the hydrogen in material due the single electron orbit in the hydrogen atom.

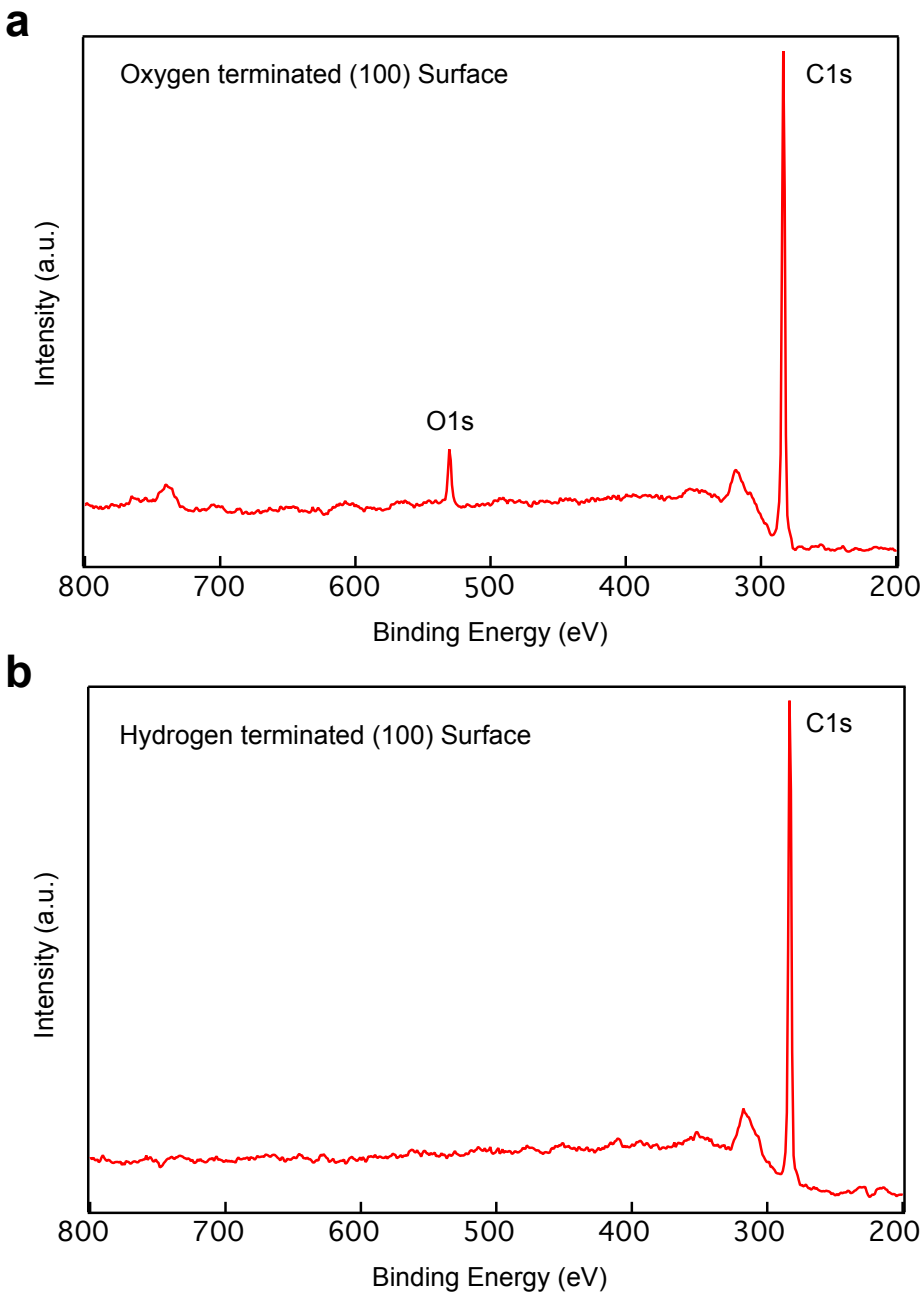

Figure 5.3 XPS wide survey on **(a)** the oxygen-terminated diamond (100) surface prepared by the acid etch method and annealed with 300 ℃; **(b)** the hydrogen-terminated diamond (100) surface prepared by the *in situ* non-thermal H* plasma treatment.

For the hydrogen terminated surface, UPS data shown in Figure 5.4 shows a Negative Electron Affinity (NEA), of -0.58 eV (secondary electron cut-off at 16.97 eV, VBM at 0.70

eV), presents on this surface.

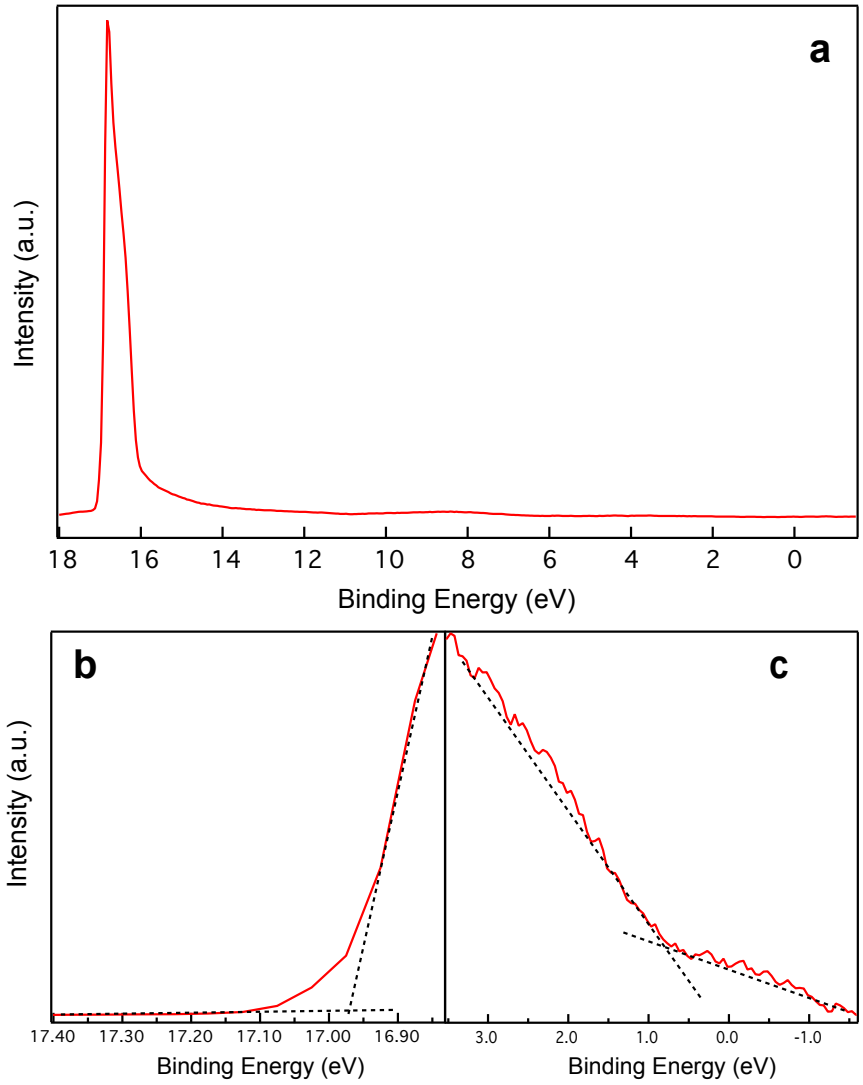

Figure 5.4 Valence band survey on the hydrogen-terminated diamond (100) surface prepared by the *in situ* non-thermal H* plasma treatment: **(a)** wide-scan UPS spectra of the surface; **(b)** High-resolution spectra of secondary electron cut-off of the surface; **(c)** High-resolution spectra of valence band maximum (VBM) for the surface.

	E_{Sec} (eV)	E_{VBM} (eV)	ϕ (eV)	χ (eV)
C:H	16.97±0.02	0.70±0.02	6.67±0.02	-0.58±0.02

Table 5.1 Calculated work function ϕ and electron affinity χ of the H-terminated diamond (100) surface.

5.3 Result and Discussion

5.3.1 Bulk 5-FU on Diamond Surface

Powder 5-FU was loaded in a home-made Knudsen-cell (K-cell) in an UHV system. A bulk layer of 5-FU was then deposited on the oxygen-terminated surface and hydrogen-terminated surface respectively at a very small evaporation temperature (due to the active chemical stability of 5-FU), followed by characterisation with x-ray photoelectron spectroscopy (XPS), near edge x-Ray absorption fine structure (NEXAFS).

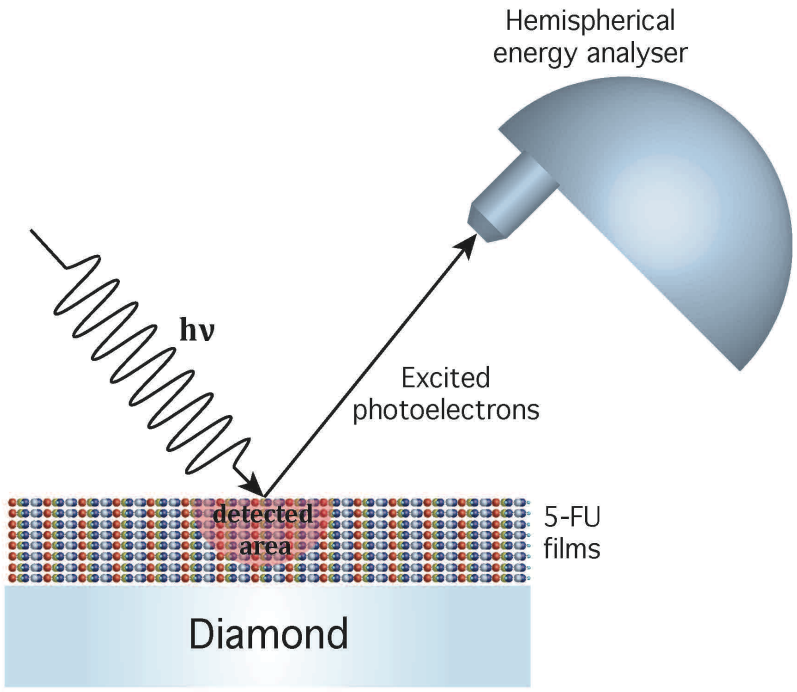

Figure 5.5 Schematic diagram of the XPS process, shown the depth sensitivity of the measurement.

The XPS wide survey of the bulk 5-FU layer deposited on the oxygen-terminated (100)

diamond surface is presented in Figure 5.6, which has a quantified concentration of C1s, F1s, N1s and O1s as 42.7%, 12.3%, 23.9% and 21.1%. This result is compatible with the 4:1:2:2 of C, F, N and O relative abundance in the moleculer structure of 5-FU. The core level profiles of F1s and N1s have been measured for further analysis which will be discussed later (shown in Figure 5.10).

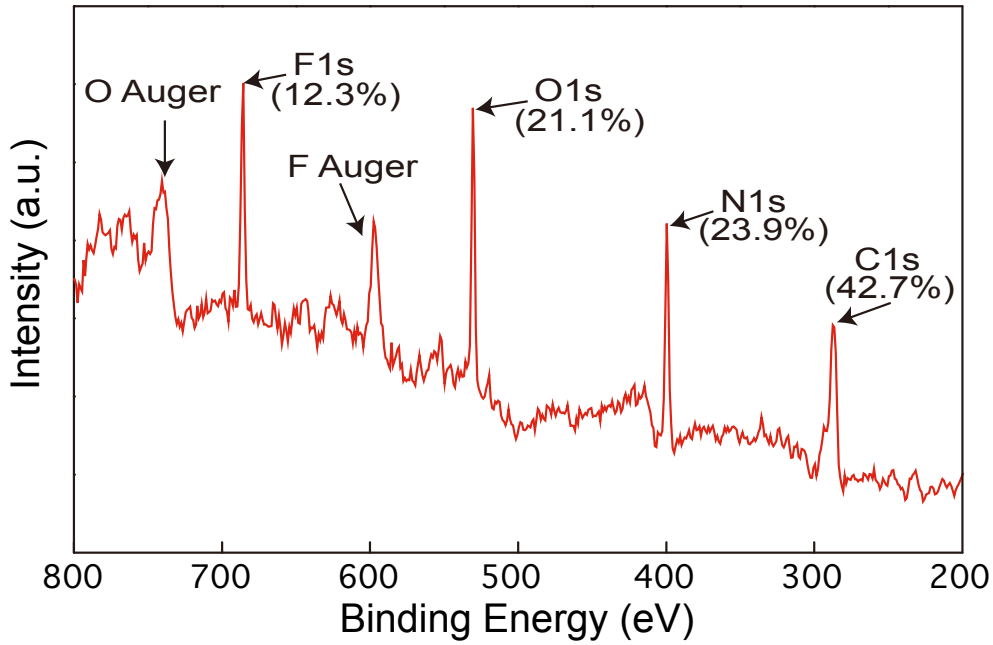

Figure 5.6 XPS wide survey of the 5-FU bulk film shortly after deposition on an oxygen-terminated (100) diamond, quantification of each core levels has been noted.

5.3.2 5-FU on Oxygen Terminated Surface

The same XPS wide survey (Figure 5.7) was measured on the diamond (100) surface after 90 minutes of the deposition, which shows a 5-FU bulk films as in Figure5.6. The quantification of the four core level has slightly changed but not obviously, which give a ratio of C1s: F1s: N1s: O1s as 45.4%: 11.7%: 21.6%: 21.3%. The concentrations of N1s and F1s have reduced in a small range indicating that more photoelectrons (C1s and O1s)

from the substrate (oxygen-terminated diamond) was detected and a small amount of the 5-FU film has desorbed during this period. In addition, a set of core level measurement was performed after the wide scan and the result will be discussed together with the bulk film data and hydrogen-terminated data later (shown in Figure 5.10).

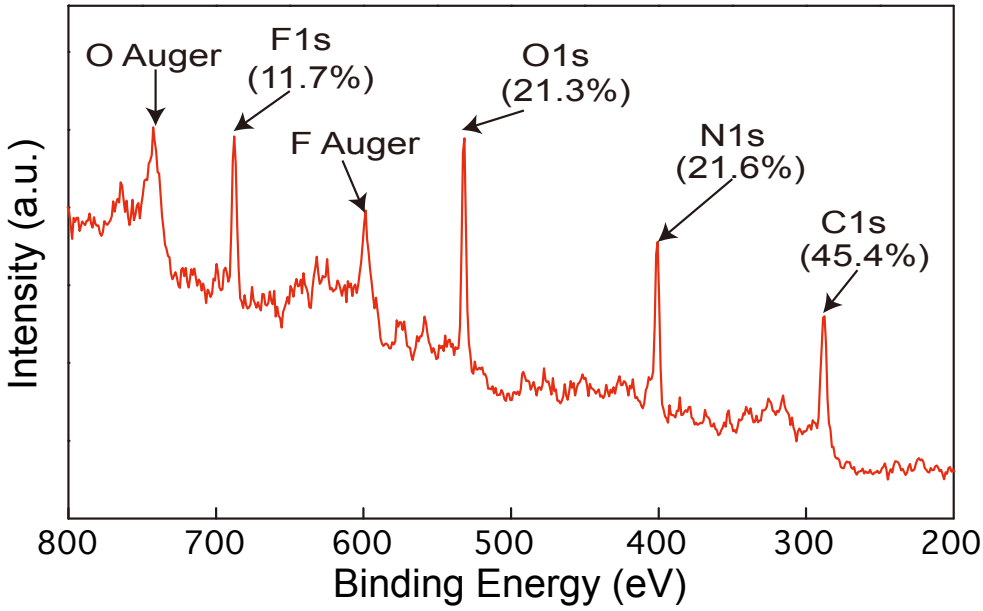

Figure 5.7 XPS wide survey of the 5-FU film measured at 90 minutes after deposited on an oxygen-terminated (100) diamond, quantification of each core levels has been noted respectively.

Meanwhile, the NEXAFS measurement of the nitrogen K-edge was performed with 5-FU films on O-terminated diamond, shown in Figure 5.8. To understand the XAS data, the dipole selection rules between an *s* electron in its initial state and a final state with *p*-like character; the outgoing electron-wave propagates in the direction of the light's

polarization vector. In a molecular picture, if the polarization of the light is (close to) coplanar with the plane of π-orbital, photo excitation cannot occur. Similarly, if the light's polarization vector is perpendicular to the plane of the π-orbital, the photo excitation occurs with highest probability. Since the delocalised π-orbitals are coplanar with respect to the 5-FU molecule's aromatic ring, angle-dependent XAS can be used to understand the orientation of well-ordered organic molecules on surfaces. The result in Figure 5.8 supports the notion of a change in the molecular π-bonding configuration of the molecule. The π^* absorption features are reduced at normal incidence relative to the measurement at 45° incidence, indicating that the molecules have a preference to lie flat on the substrate[131].

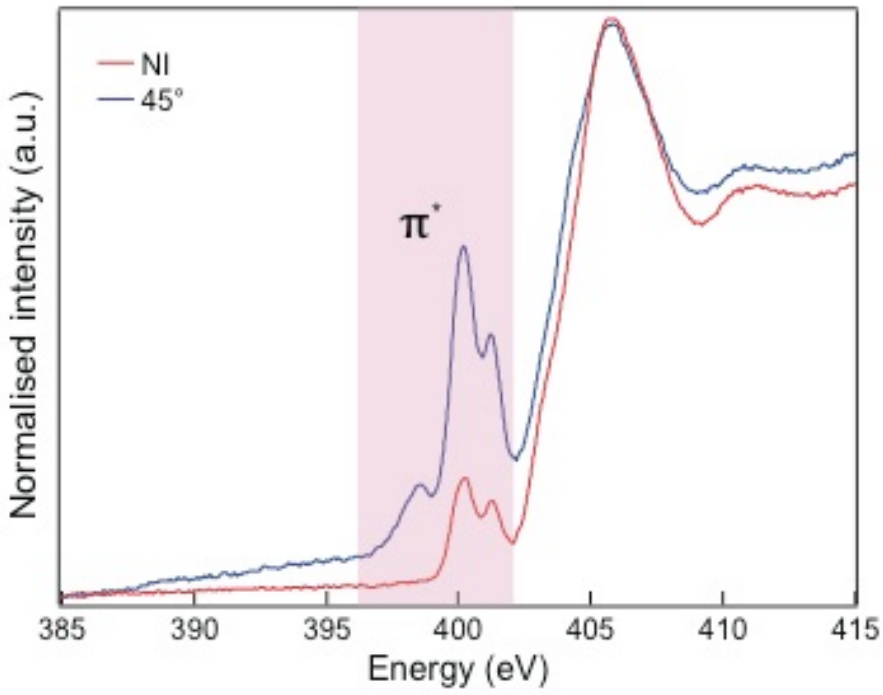

Figure 5.8 XAS measurement of Nitrogen K-edge at two different incidence angles for 5-FU films on oxygen-terminated (100) surface.

5.3.3 5-FU on Hydrogen Terminated Surface

A bulk film of 5-FU was deposited on the hydrogen-terminated diamond (100) surface. A XPS wide survey measured at 90 minutes after the deposition (shown in Figure 5.9) shows an extraordinary different result compared with the oxygen-terminated surface. The F1s peak has almost disappeared from the spectra and only left a small amount of O1s and N1s peaks as 3.2% and 2.2% respectively at 90 minutes after the deposition of 5-FU bulk film. Therefore it shows 5-FU films deposited at room temperature desorbed dramatically on H-terminated diamond (100) surface compared with the surface which is oxygen-terminated. The intensity reduction in the XPS wide scan is more pronounced on the H-terminated surface than the O-terminated surface, indicating a stronger adhesion of the film on the latter geometry of diamond surface.

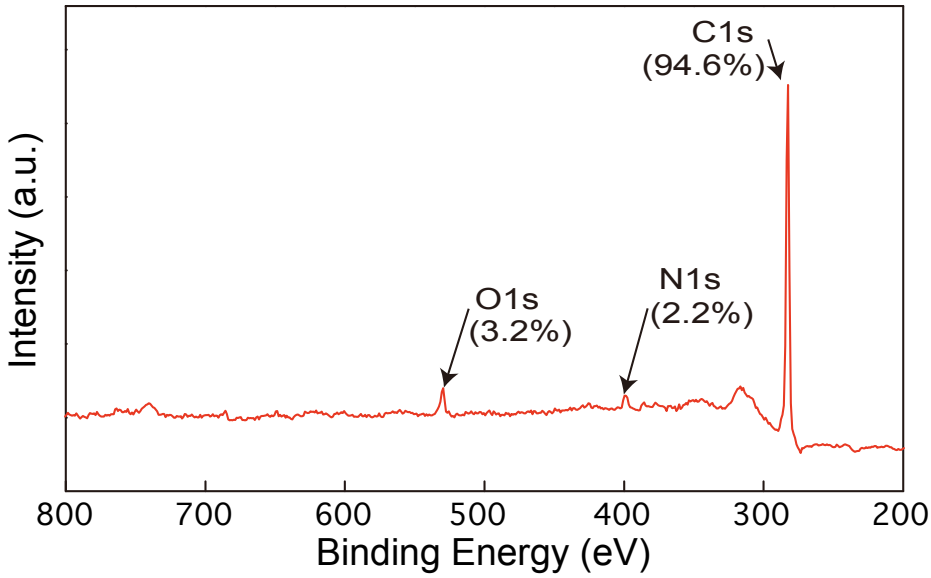

Figure 5.9 XPS wide survey of the 5-FU film measured at 90 minutes after deposited on an hydrogen-terminated (100) diamond, quantification of each core levels has been noted.

	F1s (%)	O1s (%)	N1s (%)	C1s (%)
Bulk 5-FU	12.3	21.1	23.9	42.7
5-FU on O:C	11.7	21.3	21.6	45.6
5-FU on H:C	0.00	3.2	2.2	94.6

Table 5.2 Concentration of F1s, O1s, N1s and C1s core levels of bulk 5-FU layer, 5-FU on O-terminated diamond (100) surface and 5-FU on H-terminated diamond (100) surface measured at 90mins after deposition.

Moreover the core level profiles of F1s and N1s have been monitored after wide survey on the hydrogen-terminated surface. Figure 5.10 shows the XPS measurements of the N1s and F1s core levels components for bulk 5-FU (upper panel), 5-FU on oxygen-terminated surface (middle panel) and 5-FU on hydrogen-terminated surface (lower panel). The raw data have been normalised to the photon flux, analyser transmission function and photoionisation cross-section, thus the area of each component gives a quantitative estimate of the molecular stoichiometry (shown in Table 5.1). The bulk 5-FU has a single N1s component, while the thinner films have a second component for both terminated surfaces. The F1s/N1s ratio on the O-terminated surface is in agreement with the composition of the 5-FU molecule (around 1:2). While on the H-terminated surface, the F1s/N1s ratio may not be reliable since the drug molecules were mostly desorbed (Figure 5.9). The peak position shifts are due to the charging effect on the B-doped diamond surface. However the second component can be attributed to interfacial bonding between the N of the 5-FU molecule and the diamond surface.

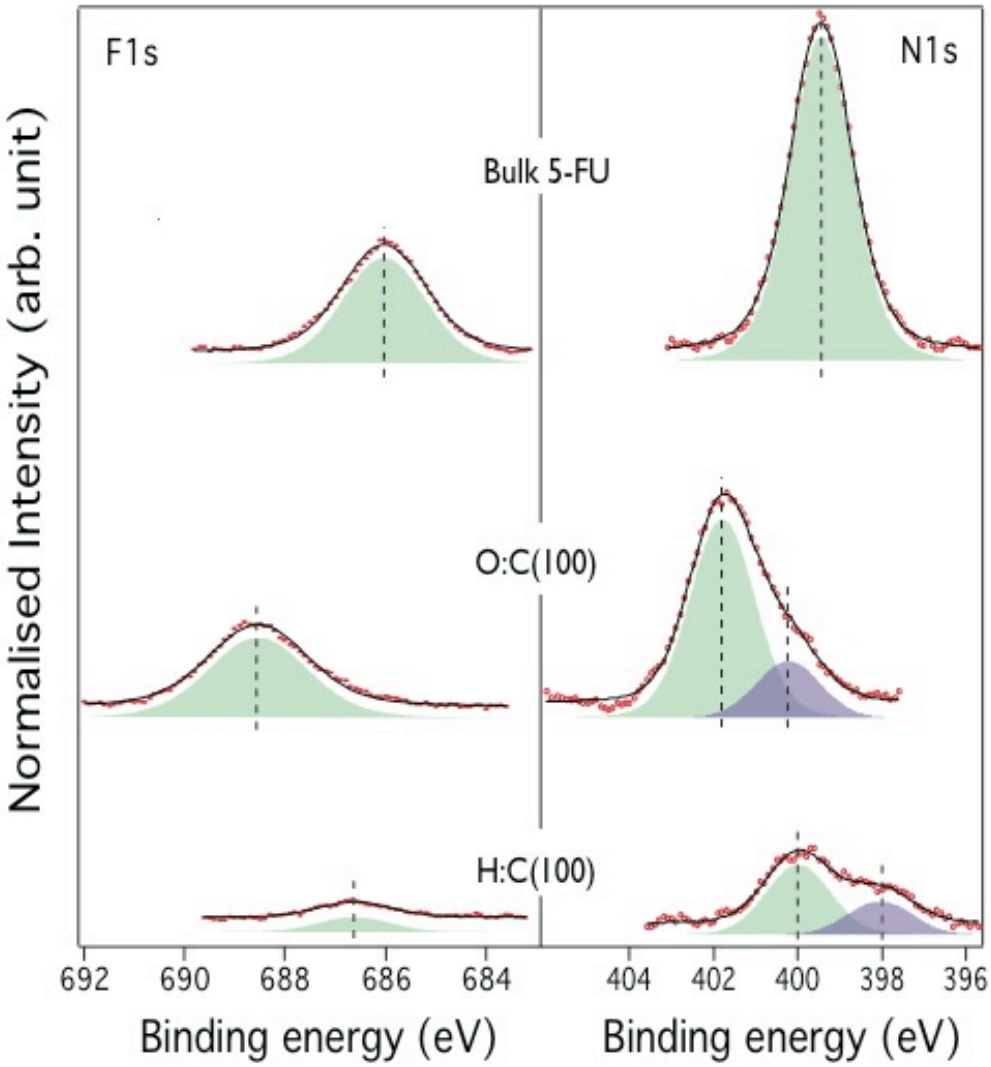

Figure 5.10 XPS measurements (N1s and F1s core levels) components for bulk 5-FU (upper panel), 5-FU on oxygen-terminated surface measured at 90 mins after deposition (middle panel) and 5-FU on hydrogen-terminated surface measured at 90 mins after deposition (lower panel). The green component indicates unreacted 5-FU. Raw data (red dots) and fits (black lines) are shown.

	Bulk 5-FU	**5-FU/O-terminated**	**5-FU/H-terminated**
F1s/N1s %	44.6%	49.0%	15.1%

Table 5.3 Quantified F1s/N1s ratio calculated from the core level spectrum in Figure 5.10.

5.4 Chapter Conclusion

In this chapter 5-FU/diamond interfaces have been investigated by XPS and XAS. Diamond thin films have great potential as protective coating materials in biomedicine due to their biochemical inert property. A bulk film of 5-FU was deposited on oxygen-terminated (100) diamond surface and hydrogen-terminated surface respectively. XPS wide surveys and core level scans were performed on each surface at 90 minutes after the deposition in comparing with the bulk structure of 5-FU. The results shows that 5-FU attaches to the oxygen-terminated diamond (100) and silver surfaces but not to the hydrogen-terminated diamond (100) surface, which indicates there is a surface termination effect with diamond which could relate to the surface properties, such as chemical bond, electron affinity and dipole, of the diamond surfaces. Therefore the interaction between drug molecules and inorganic materials involved in their delivery can have a significant effect on the molecular structure. Besides DFT structural optimisation calculations have confirmed that 5-FU decomposition on Ag substrate is an energy output process, on a graphene surface decomposition is an energy input process in reference [131]. In this case, a similar calculation on the 5-FU/diamond interfaces will be helpful for studying the structure and chemical process of this work.

CHAPTER 6 – IRON THIN FILMS

6.1 Introduction

In this chapter, the effect of the pure strain on the electronic structure of Fe thin film has been investigated through PES, theoretical calculation and magnetic measurements. The electronic structure in a material can be controlled by the lattice strain on the material, which may have a significant effects on the material properties physically or chemically [134], for example, a lattice deformation of 1% can change a semiconductor's band gap by up to 100 meV[135]. Therefore, in recent years, much research has been carried out on utilizing elastic strain to modulate the magnetic, electric, or transport properties of ferromagnetic materials [136-155]. Presently, the most effective strain engineering method to realize a continuous modulation is through electrically controlling ferroelectric/ferromagnetic heterostructures [136-141, 143-151]. The deformation in the ferroelectric substrate, which is induced by electric field mediated polarization, transfers to the lattice strain in the ferromagnetic layer. In such cases, the electronic structure and related properties of the ferromagnetic film are co-modulated by a strain-mediated magnetoelectric coupling effect (i.e. pure strain effect) and a charge-mediated magnetoelectric coupling effect (i.e. surface charge effect), as shown in Figure 6.1a. It is difficult to distinguish the strain effect and the surface charge effect since they are generated and exists simultaneously. However, it is possible to tune the relative magnitude of these two effects during the property modulation by adjusting the

ferromagnetic layer thickness[156] or by inserting a proper non-magnetic layer at the ferroelectric/ferromagnetic interface [140]. Shu *et al.* reported that the proportion of the surface charge effect to the strain effect in Ni/$BiTiO_3$ multiferroic heterostructure increased gradually as the Ni thickness was decreased [157]. Nan *et al.* found that the surface charge effect in the electrically controlled NiFe/ferroelectric composite could be reduced by inserting a 5nm Cu layer at the interfaces [140]. However, it is still impossible to entirely remove the surface charge effect from the modulation mechanism when using conventional electrically controlled strain manipulation methods. In this respect, it is difficult to study the modulation behaviors of electronic structure and related properties in pure strain treated ferromagnetic films which is significant for the developments of strain engineering in spintronic materials and strain-assisted spintronic devices.

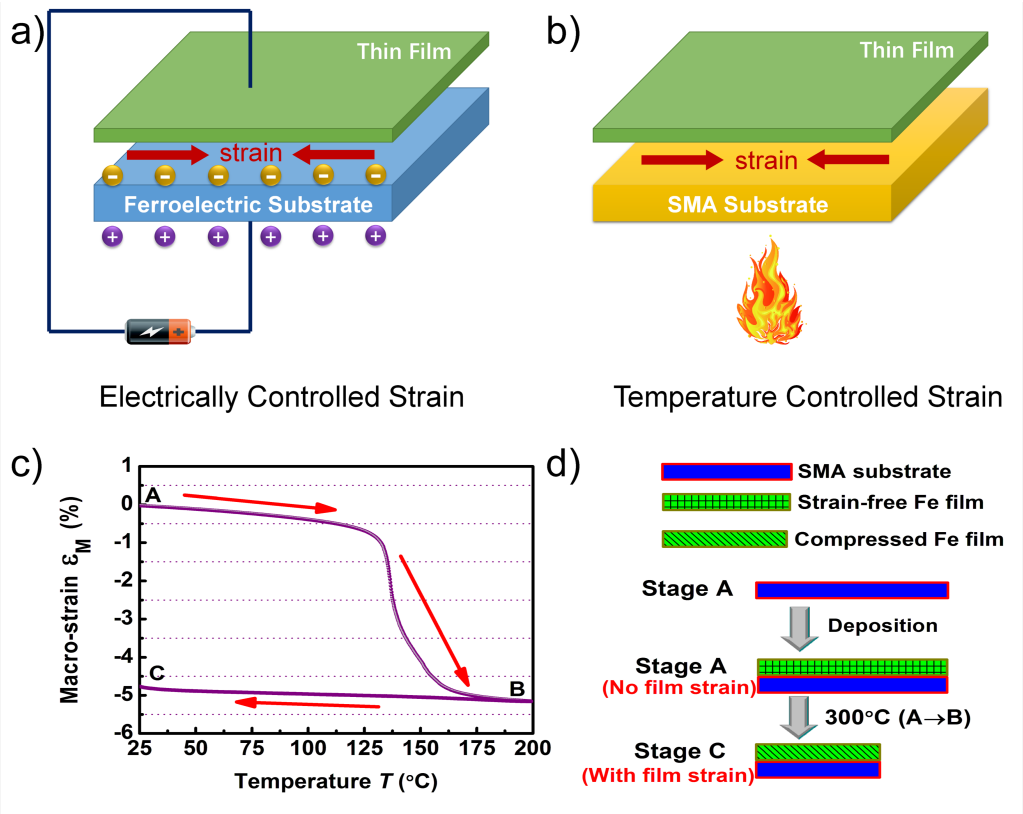

Figure 6.1 The top two schematic diagrams present two kinds of strain modification methods: (a) Electrically controlled strain effect from a ferroelectric substrate, where both strain effect and the surface charge effect coexist; (b) Temperature controlled strain effect from a SMA substrate, where only the strain effect exists. (c)Thermal expansion curve of the pre-stretched SMA substrate to show the thermal history dependency of the substrate's macro-strain; (d) Schematic diagram of the film deposition and the strain control process: an Fe film was deposited on the pre-stretched substrate at room temperature (state A). Then, the sample was heated up to 300℃ to induce the shrinkage deformation in the substrate (A→B), leading to the construction nonvolatile lattice strain in the film at room temperature (stage C).

In this investigation, a non-electrically controlled method to introduce purely strain mediated modulation has been designed by using NiTi(Nb) shape memory alloy (SMA) as the substrate material of the thin films. As shown in Figures 6.1b-6.1d, the substrate deformation, which is realized through a temperature-controlled phase transition from a martensite to an austenite structure, can transfer to the lattice strain in the attached

film. Since the strain modulation in this system derives from the temperature-controlled shape memory effect instead of the electricity-controlled effect, the conventional surface charge effect can be avoided. Moreover, NiTi-based SMA possesses a remarkable strain output as large as 6-8% [158, 159], providing a better chance to study in-depth the pure strain effect on the tunability of electronic structure and related property of the thin film. It is well known that Fe based composite materials are the critical magnetic layers in many important spintronic devices [156, 160-163], thus, Fe thin film was chosen as a representative ferromagnetic material in this work. With the deposition of Fe films on the SMA substrates and the control of the shape memory effect by temperature, a pure strain can be applied to the Fe films. Based on the subtle structure, the pure strain effect on electronic structure modulation in the Fe films were studied with *in situ* x-ray photoelectron spectroscopy (XPS) measurement and first-principle calculations. The results indicate that compressive strain strengthens the shielding effect from the overlaps of outer orbits, thus regulating the binding energy of the core electrons. Moreover, the lattice strain alters the electronic density of states (DOS) and spin distribution of the outer d orbitals, which results in the tunability of the bandwidth and spin-orbit coupling strength and consequent modulation of the magnetic anisotropy of the films.

6.2 Experimental

The film deposition and the strain control used in this work are shown in Figures 6.1c-6.1d. The NiTi(Nb) SMA substrate (composition $Ni_{45}Ti_{45}Nb_{10}$, thickness 0.5mm) was pre-stretched by heating with a 10% tensile deformation to induced reorientation of the martensite phase. The thermal expansion curve of the substrate, which presents the thermal history dependence of strain, is shown in the Figure 6.1c. After the pre-stretching process, the substrate was set as the initial state A in the Figure 6.1c. The substrate was polished by rough grinding and elaborate polishing processes, and then transferred into an ultra-high vacuum chamber for Fe film growth.

6.2.1 Fe Thin Film Growth

Layer b [43]y layer growth as observed in real-time photoemission studies can be seen as a linear attenuation of the intensity of substrate core levels when plotted on a semi-logarithmic plot of peak intensity against time, whereas as the persistence of the substrate core level during deposition indicates some form of clustering, as observed when monitoring C1s whilst depositing Al on diamond[14, 15]. The growth rate and the growth mode of Fe overlayers have been demonstrated with real-time x-ray photoelectron spectra of Ti 2p core level from the SMA substrate, as shown in Figure 6.2a. According to Eqn 2.3.11, the Fe thickness d was determined from the real-time spectral intensity I and the initial intensity I_0 of Ti 2p core level, and the electron

attenuation length of the photoelectron ($\lambda = 1.1\ \mathrm{nm}$ [43]), given as,

$$d = -\lambda \ln \frac{I}{I_0}$$

(Eqn 6.2.1)

Using Eqn 6.2.1 the growth rate was calculated to be approximately 0.0083 Å/s. The linear relationship in Fig. 6.2a indicates the Frank-van der Merwe growth mode, as shown in figure 6.2b. This also suggests the custom-made iron K-cell enables the growth of a strain-free and uniform Fe overlayer on the SMA substrate. A series of Fe films with thicknesses (*t*) of 1.5nm, 3.0nm, 5.2nm, 6.5nm, and 8.5nm were deposited on the substrate using the iron k-cell. The base pressure in UHV chamber was about 9.7×10^{-11} mbar.

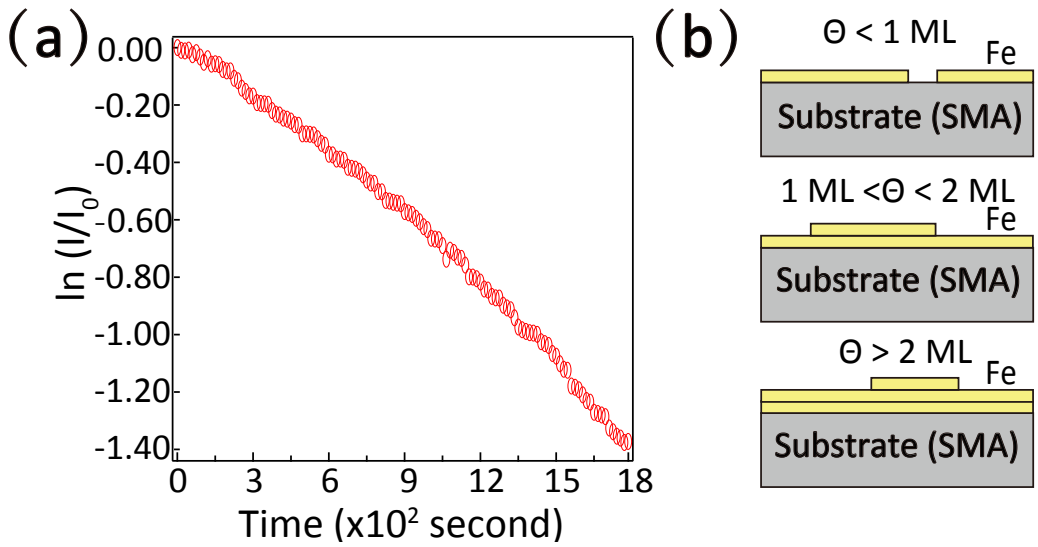

Figure 6.2 (a) The experimental Fe intensity plotting during a 30 mins growth procedure. (b) The Frank-van der Merwe layer-by-layer growth mode. Θ represents the layers of the Fe film growing on the SMA substrate.

6.2.2 Strain Induced Processing

The as-deposited films maintains a strain-free state because the substrate is still in state A,

shown in Figure 6.1. Then, the as-deposited samples went through thermal treatments *in vacuo* with a gradual increase of temperature up to 300℃, which induced the inverse martensitic phase transition and shrinkage deformation in the substrate (state A→state B). The heating rate was controlled to around 7-8 ℃/min. The heating process also transfers a compressive strain to the attached Fe film, which can be preserved even when the sample was cooled down to room temperature (state C). The maximally recoverable macro-strain in the substrate (ε_M) is around -5%.

The strain-induced electronic structure variation of inner orbits in the Fe films was systematically studied by *in situ* XPS measurements. A Mg K_α source was used during the XPS measurement with a photon energy of 1253.6 eV. The energy analyzer was operated at constant pass energy of 20 eV. The detection precision of the binding energy is 0.03 eV, measured on a calibration target. Meanwhile, the snapshots of Fe2p core levels were collected with REES to monitor the electronic structure evolution with temperature, especially during the whole phase transition process of the substrate and the subsequent process of exerting continuous strain on the Fe film. In addition, angle-resolved XPS (ARXPS) analysis was also conducted to detect the binding energy of Fe2p electrons at different depths in the strain-treated Fe film. This helps when analyzing the strain distribution along the film thickness. The detectable depth of XPS (d) can be estimated by the formula $d=3\lambda\cdot\sin\alpha$ [164], where λ and α are the electron attenuation length for photoelectrons and the take-off angle for photoelectrons with

respect to the sample surface plane, respectively. For Fe atoms, the maximal *d* is 3.1 nm (λ=1.03 nm [164], *α*=90º). After the XPS measurements, a 5nm protecting Ta layer was deposited on the Fe/NiTi(Nb) samples for subsequent magnetic property measurements. The hysteresis loops were measured using a physical property measurement system (PPMS) with in-plane (along the strain) or out-of-plane fields up to 20 kOe. Meanwhile, first principle calculations using Density Functional Theory (DFT) were carried out to simulate the strain-induced tunability effects on the DOS and spin distribution of the outer d electrons. The calculation was based on the projected augmented-wave (PAW) from the Vienna ab initio simulation package (VASP) [165, 166] and the Perdew-Burke-Ernzerhof (PBE) exchange-correlation functionals [167]. For simplicity, it includes 2 Fe atoms per unit cell. The lattice constants of the Fe cell are referenced from experimental data, a=b=c=2.86 Å, as shown in figure 6.7a. A fine K-mesh of 16×16×16 and energy cutoff at 500 eV were used to ensure numerical accuracy.

6.3 Results and Discussion

6.3.1 The Electronic Structure of Inner Orbits in Fe Films

6.3.1.1 Standard XPS Measurement

The electronic configuration of Fe atoms arranges as $1s^2\,2s^2\,2p^6\,3s^2\,3p^6\,4s^2\,3d^6$. The strain effect on the electronic structure of inner orbit (Fe2p) is investigated through *in situ* XPS measurements on the strain-free and the strain-treated Fe films. Figure 6.3 shows the

high resolution XPS spectra of Fe2p electrons from as-deposited samples (strain-free state) and 350 ℃ thermally treated samples (compressive strain state) for different Fe film thicknesses. The substrate finishes the phase transition and transfers the maximal strain to the film after heating to 300 ℃ thermal treatment. As shown in Figures 6.3a-6.3e, Fe atoms in both the strain-free and the strain-mediated samples show the elemental state, implying no obvious oxidation or alloying before or after the thermal treatment. However, the Fe $2p_{3/2}$ peak shifts towards the lower binding energy direction after applying the strain on the films, indicating that the compressive strain affects the electronic structure of the inner orbits of the Fe film significantly. For a crystalline material, the outer orbital electrons usually have a shielding effect on inner orbital electrons, which reduces the effective nuclear charge. When the Fe lattice is compressed, the overlaps of the outer electron orbitals between two neighboring Fe atoms will be increased whilst decreasing the interatomic distance, leading to the enhanced shielding effect and the lower nuclear charge. This will reduce the binding energy of inner electrons, resulting in the XPS peak shift towards the lower binding energy direction.

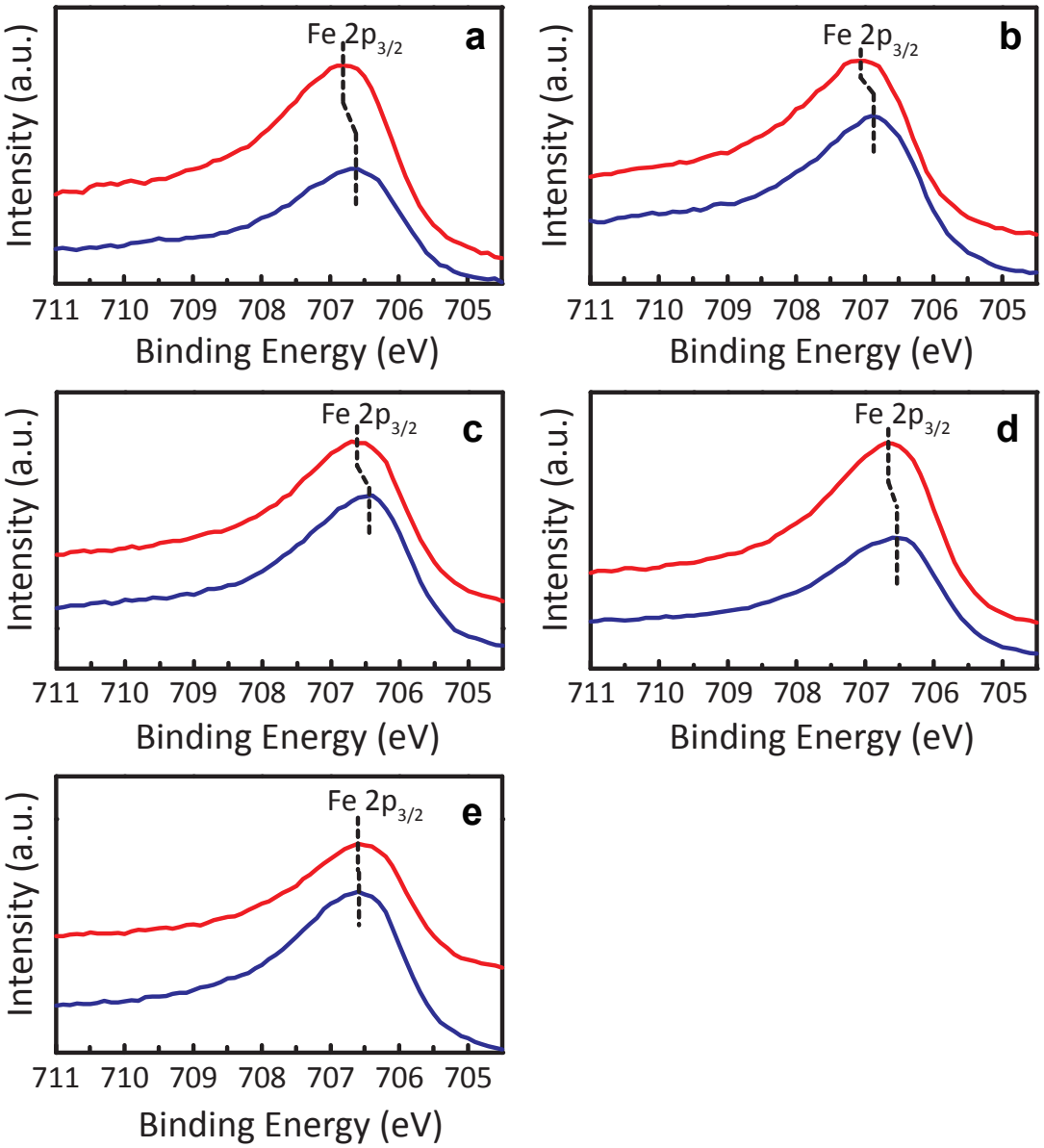

Figure 6.3 High resolution XPS spectra of the characteristic Fe2p electrons in the NiTi(Nb)/Fe samples with different film thickness *t*, before annealing (strain-free state as red line) and after annealing at 350℃ (strain-mediated state as blue line): (a) *t*=1.5 nm; (b) *t*=3.0 nm; (c) *t*=5.2 nm; (d) *t*=6.5 nm; (e) *t*=8.5 nm. All spectra were measured at normal emission angle (α=90º).

However, the binding energy variation of the $Fe2p_{3/2}$ electron between the as-deposited film and the annealed film ($\Delta BE=BE_{As\text{-}deposited}- BE_{Annealed}$) varies with the Fe thickness *t*, as shown in the figure 6.4. The thinner the film is, the larger the ΔBE is. ΔBE maintains a

large value (~ 0.16 eV) until *t* reaches 3.2 nm and then shows a sharp decrease for *t* greater than 3.2 nm. The peak shift almost disappears when *t* increases to 8.5 nm (Figure 6.3e). To explain the result, we assume the strain is non-uniform along the film thickness direction. The strain amount is a maximum at the NiTi(Nb)/Fe interface and attenuates towards the film surface, implying that the strain has an effective interaction depth in the Fe film. For the very thin films with thickness ranging between 1-3nm, the strain attenuation may be very small and negligible. Thus, the strain effect on electronic structure exists throughout the film thickness, leading to the apparent tunability effect on the binding energy of inner electrons and thereby a large ΔBE value. When the Fe film is thicker than 3nm, the strain effect starts to reduce exponentially with thickness, resulting in the rapid decrease of ΔBE. For the 8.5 nm film, the strain effect is almost undetectable within XPS detection depth due to serious decay of the strain magnitude. Since the XPS detection depth (d=3λ·sinα) is about 3.1 nm for normal emission (α=90º), XPS has an ability to collect information from film surface to 3.1 nm beneath the surface. In other words, the maximally detectable position is around 5.4nm above the NiTi(Nb)/Fe interfaces in the Fe film (8.5 nm). It is reasonable to infer from the results that the effective interaction depth of the strain effect is around 5-6 nm under a substrate deformation of 5%.

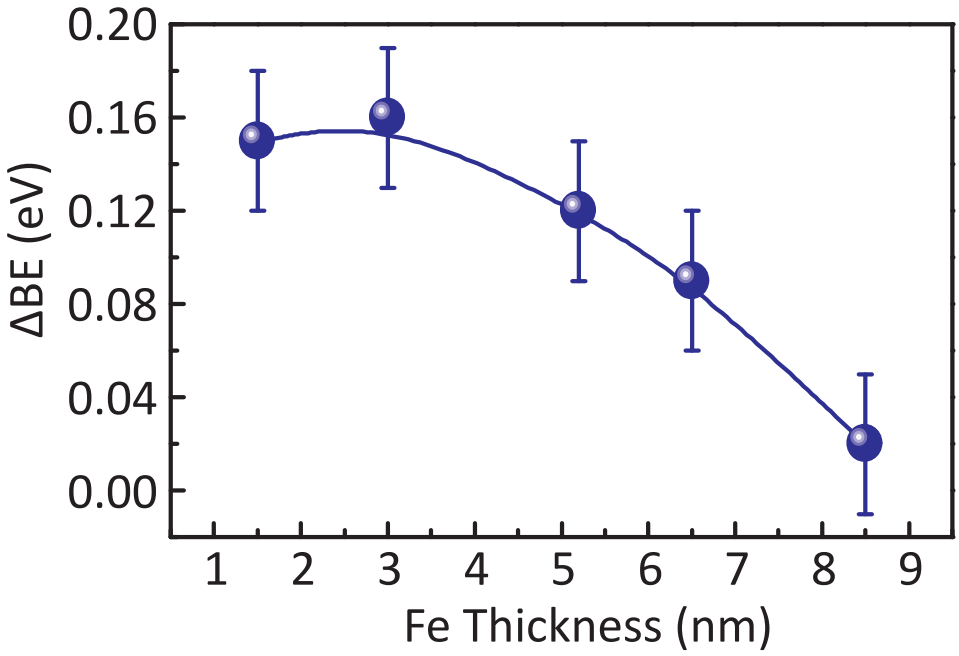

Figure 6.4 The dependence of binding energy variations of $Fe2p_{3/2}$ electrons (ΔBE) on *t*.

6.3.1.2 Real-time XPS Measurement

In order to further study the strain effect, the temperature dependence of the electronic structure evolution in the SMA/Fe (1.5 nm) sample was monitored by using REES. The subsequent process of exerting continuous strain on the Fe film during the whole phase transition process of the substrate has been demonstrated. The variation of the binding energy of $Fe2p_{3/2}$ electrons with temperature is summarized in Figure 6.5. The binding energy values fluctuate around 706.7±0.1 eV before the onset of a phase transition in the substrate (the temperature lower than the 130 ℃). When the temperature moves into the phase transition region (130-170 ℃), the substrate starts to shrink gradually and thereby transfer the continuously mediated strain into the Fe film, leading to the aforementioned strain effect on the electronic structure. Therefore, the binding energy

decreases at a certain rate accordingly. However, as the phase transition completes as the temperature surpasses 170 ℃, the transferred strain on the film reaches the maximum value, resulting in the lowest binding energy of Fe2p electrons. With further increase in temperature, the binding energy fluctuates around 706.5±0.1 eV.

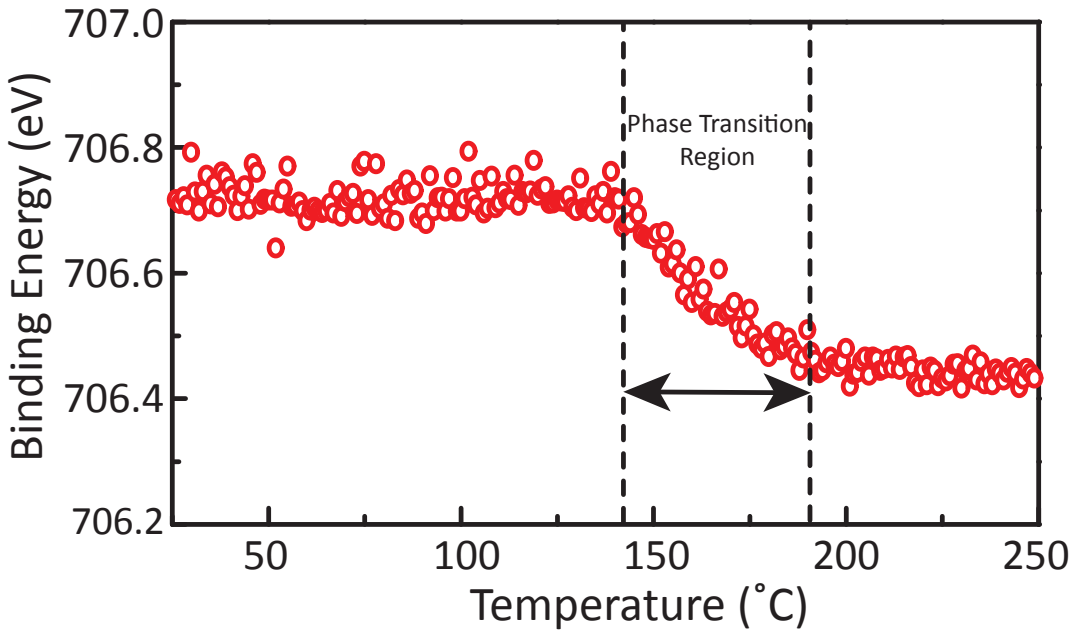

Figure 6.5 Variation of the binding energy of $Fe2p_{3/2}$ electrons with temperature, obtained from real-time XPS spectra of the NiTi(Nb)/Fe (1.5 nm) sample. The phase transition temperature region ranges between 130-170℃.

The depth-dependent strain effect on the electronic structure of the SMA/Fe (5.2nm) sample was also measured using ARXPS, as shown in Figure 6.6. The detection depth of XPS (d=3λ·sinα) is controllable by adjusting the take-off angle for photoelectrons α, allowing us to obtain information from different film depths. The strain attenuates from the NiTi(Nb)/Fe interface to the film surface, which makes the strain effect decay towards the film surface accordingly. Thus, the depth-dependent electronic structure

tunability can be studied by varying α. In Figure 6.6, when measured at α=90º, the binding energy of $Fe2p_{3/2}$ electrons drops by 0.16 eV from the as-deposited state to the annealed state. However, with decreasing α (i.e. detecting smaller strain region), the binding energy variation ΔBE reduces to 0.14 eV (α=60º) and 0.06 eV (α=30º), respectively. This confirms the strain effect on the electronic structure decays along the film thickness direction. All of the above XPS results convince that the strain induces a significant modulation effect on the electronic structure of inner orbits in the attached Fe films, leading to apparent decrease in the binding energy of Fe2p electrons. The effective interaction depth of strain effect is around 5-6 nm in the film.

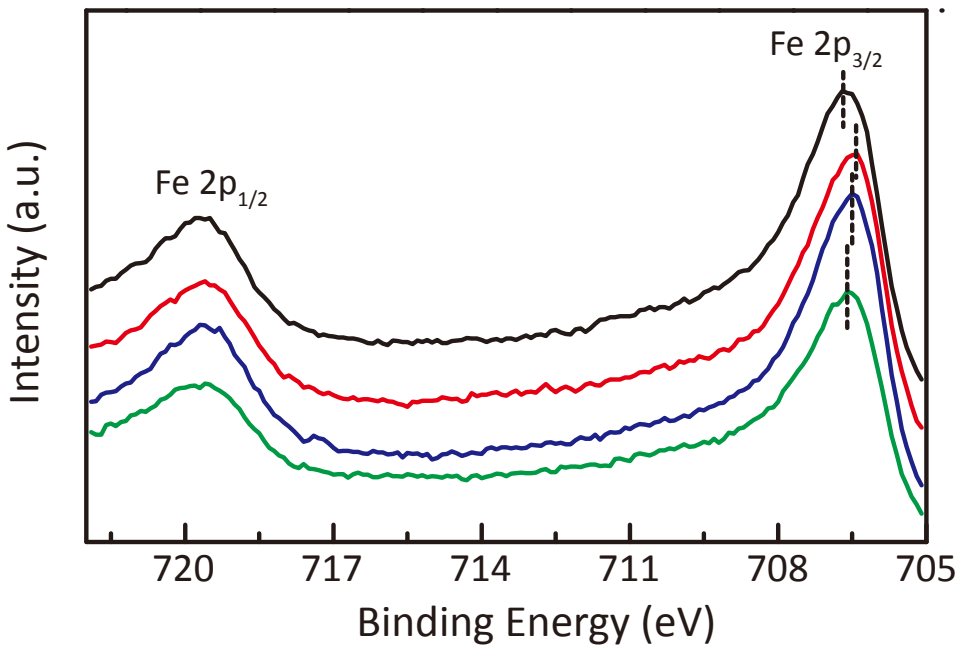

Figure 6.6 Angle-resolved XPS spectra of the NiTi(Nb)/Fe (5.2 nm) sample. Black data was measured before annealing with photoelectron take off angle a at 90°; the red, blue and green data were measured on the same sample after annealing with photoelectron take off angle a of 90°, 60° and 30°, respectively.

6.3.2 The Electronic Structure of Outer Orbits in Fe Films

6.3.2.1 DFT Calculations

To reveal the strain effect on the electronic structure of the outer orbits of the Fe films, first-principle calculations were conducted to simulate the strain-induced evolution of the density of states (DOS) and the spin distribution. Figure 6.7a shows the strain-free bcc-Fe unit cell with lattice constants **a**=**b**=**c**=2.86Å. In order to study the strain effect systematically, three lattice compression ratio (ε_L), 0%, -1%, -3%, along [010] or [100] direction were selected. The total DOS in the Fe lattice with ε_L is shown in Figure 6.7b. As the amount of strain increases, the spin distribution of spin-up electrons (↑) moves toward the Fermi level, while the spin distribution of spin-down electrons (↓) moves in the opposite direction. This indicates that the occupied states of spin-up electrons (spin-down electrons) will decrease (increase) when we increase the strain on the lattice. As a consequence, the magnetic moment of Fe crystal decreases when we increase the strain on the lattice.

Meanwhile, the partial density of state (PDOS) on different orbits was also computed for ε_L =0% (Figure 6.7c) and ε_L =-3% (Figure 6.7d). For simplicity, only the PDOS of d orbits are shown because they dominate the states near the Fermi level. For a strain-free bcc Fe crystal, the neighbour Fe atoms are along [111] direction as shown in Figure 6.7a, therefore d_{xz} or d_{yz} orbital will have the largest overlap, which leads to the maximum

states at Fermi level (indicated by the blue and red lines in the Figure 6.7c). However, when the Fe lattice is compressed along x axis or y axis, $d_{x^2-y^2}$ orbital will have the maximum overlap between neighboring Fe atoms. This leads to the largest bandwidth broadening and also the largest drop of in the PDOS intensity of the $d_{x^2-y^2}$ orbital (comparing Figure 6.7c with Figure 6.7d).

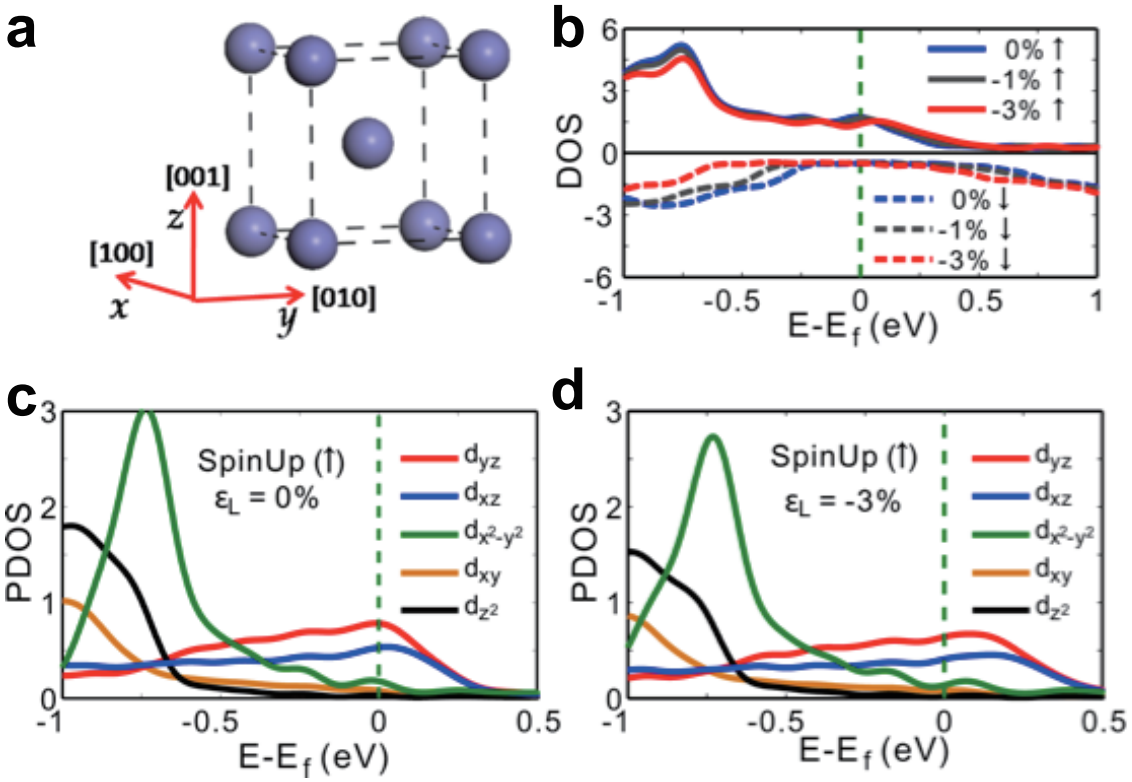

Figure 6.7 Strain effects on DOS and spin distribution of the Fe films: (a) ideal strain-free Fe unit cell with **a**=**b**=**c**=2.86 Å. (b) Total DOS evolution of spin-up (↑) and spin-down (↓) electrons when the unit cell is compressed by 0%, -1%, -3% along [010] or [100] direction. The dashed line represents the Fermi level. (c) (d) PDOS of different orbitals with lattice strain (ε_L) of 0% and -3%, respectively.

6.3.2.2 Magnetic Measurement

How does the bandwidth broadening affect the spin-orbit coupling (SOC) in the Fe

lattice? The Thomas Precession of SOC is expressed as [168],

$$H_{SO} \equiv \frac{\mu_B}{\hbar m_e e c^2} \frac{1}{r} \frac{dV(r)}{dr} \boldsymbol{L} \cdot \boldsymbol{S}$$

(*Eqn 6.3.1*)

where c is the speed of light, m_e is the mass of electron, e is the electron charge, V(r) is the electrostatic potential at a distance r, ***L*** *and* ***S*** are the orbital angular momentum and the spin angular momentum respectively. As previously mentioned, without any strain, the nearest Fe atoms have the largest d orbital overlap along [111] direction, thus the d orbital has the lowest localization along [111] direction, which leads to the smallest orbital angular momentum and spin-orbital coupling strength according to *Eqn 6.3.1*. As a consequence, the strain-free Fe crystal will have the smallest SOC energy splitting and hardest magnetization axis in [111] direction, while the easy magnetization axis of a bcc Fe crystal is along [001] direction. However, applying a compressive strain on the x-y plane, the d orbital overlap increases. This reduces the localization and decreases the orbital angular momentum ***L*** of d orbits, leading to the decrease of the SOC strength according to *Eqn 6.3.1*. Since the maximum overlap occurs on $d_{x^2-y^2}$ orbits in the x-y plane, the orbital angular momentum for the $d_{x^2-y^2}$ orbit, that is perpendicular to the x-y plane (i.e. along [001] direction), reduces the most. As a result, when the compressive strain is applied in the x-y plane, both the SOC strength and the energy level splitting in the [001] orientation have the largest decrease. Therefore, introduction of the compressive strain on the (001) plane will tilt the easy magnetization axis of the Fe film away from the [001] orientation, which results in a decrease of perpendicular magnetic

anisotropy of the films. This conclusion can be proved by our experimental results of the magnetic property measurement.

The hysteresis loops of the strain-free and strain-treated Fe films with different film thickness are plotted in Figure 6.8. The intersection of in-plane loop (blue curve) and out-of-plane loop (red curve), which is marked by an arrow, represents the anisotropy field (H_k) of the film. The effective magnetic anisotropy (K_{eff}) can be calculated by the formula $K_{eff}=M_S \times H_K/2$, where M_S is the saturation magnetization of the film. Positive K_{eff} usually stands for the perpendicular magnetic anisotropy of the film. Figure 6.9 compares the K_{eff} values of the strain-free and strain-treated Fe films for different thicknesses. All samples possess negative K_{eff} values, implying an in-plane magnetic anisotropy of the films. The H_k values of most films in Figure 6.8 increase after applying the compressive strain, representing the strain-induced harder magnetization of the films along out-of-plane [001] direction. Moreover, K_{eff} values of the strain-treated films are lower than those of the strain-free films with the same thickness, indicating that the compressive strain has the effect of tilting the easy magnetization axis of the film away from the [001] orientation. The result is consistent with the theoretical result of the aforementioned first principle calculations. However, the strain-induced K_{eff} modulation effect is more apparent in the thinner films than in the thicker films, which proves the strain effect is an interfacial tunability behavior with an effective interaction depth of around 5-6 nm.

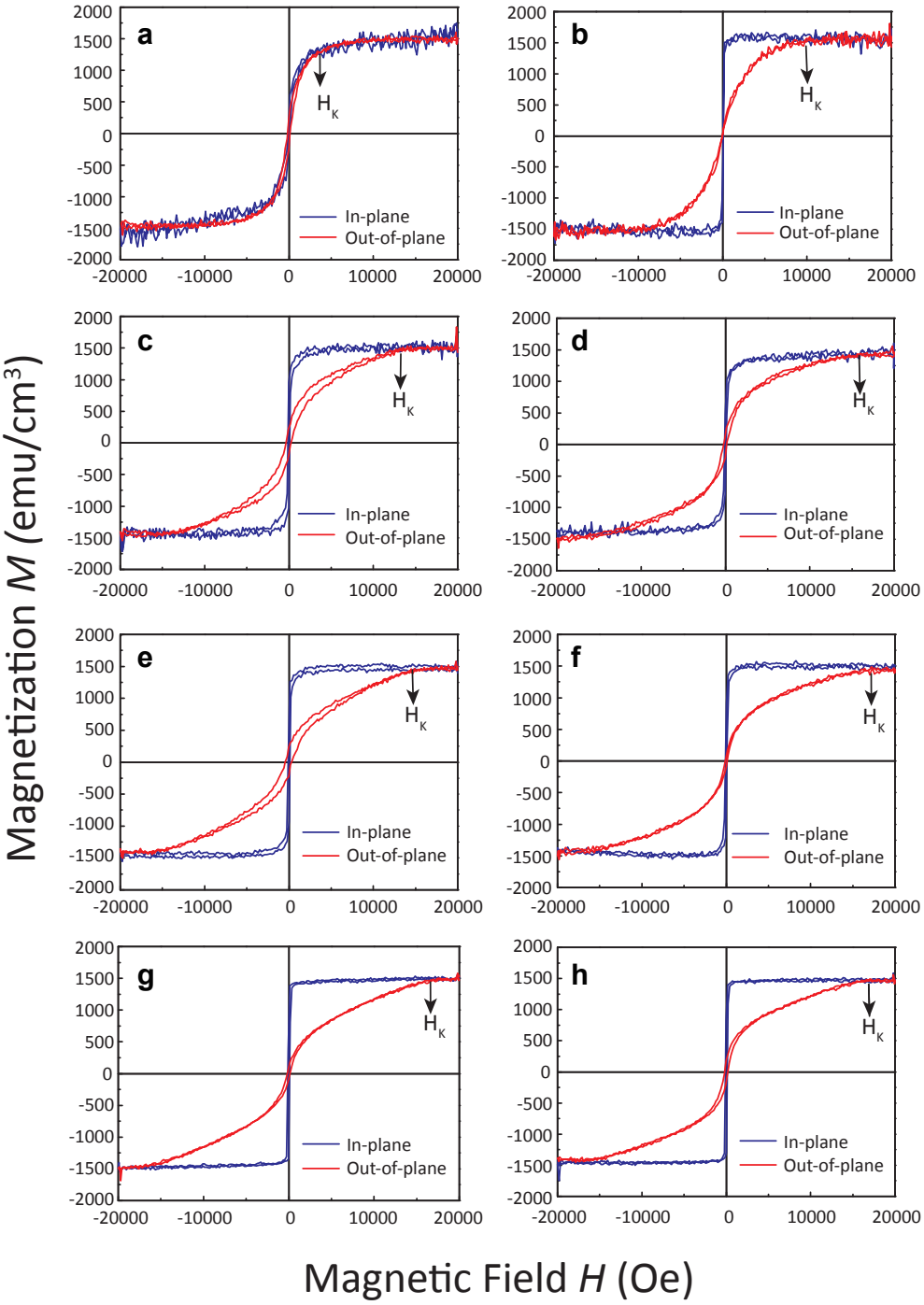

Figure 6.8 In-plane hysteresis loops (blue curves) and out-plane hysteresis loops (red curves) of the NiTi(Nb)/Fe (thickness *t*) samples before and after thermal treatments: (a),(b) *t*=1.5 nm; (c),(d) *t*=3.0 nm; (e),(f) *t*=5.2 nm; (g),(h) *t*=8.5 nm. (a), (c), (e), (g) are for the as-deposited films (strain-free state), and (b), (d), (f), (h) are for the annealed films (strain-treated state).

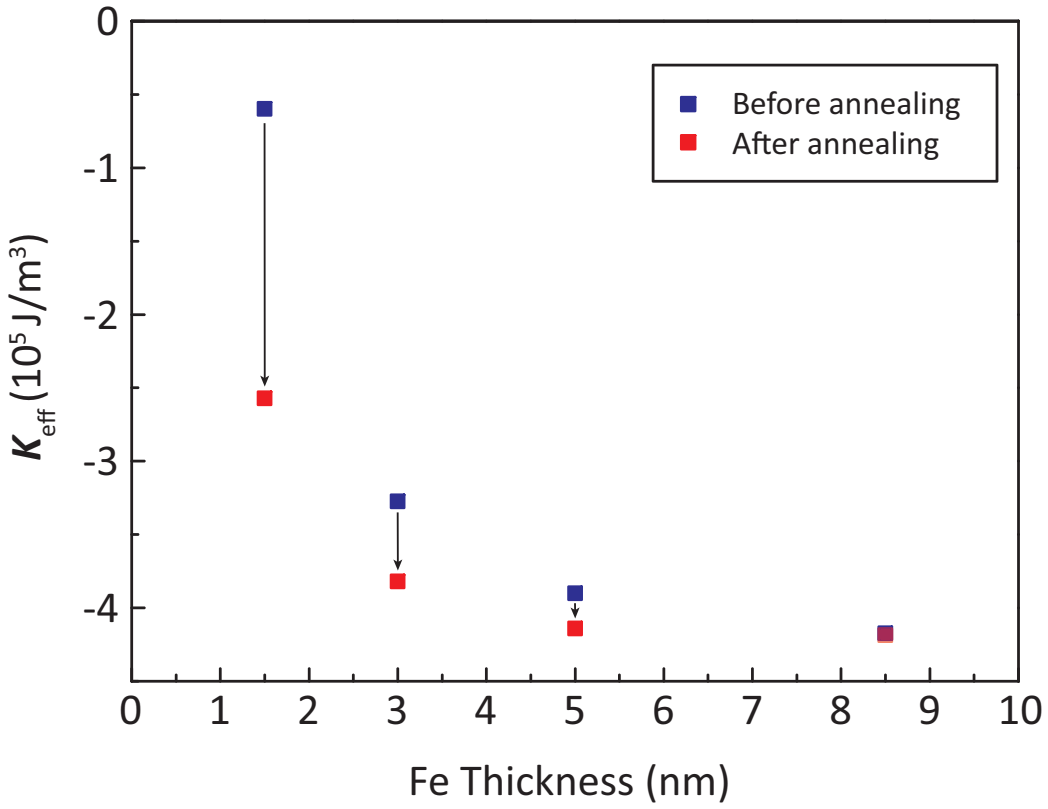

Figure 6.9 Variation of effective magnetic anisotropy (K_{eff}) of the strain-free and strain-treated Fe films with film thickness. Blue points and red points stand for the as-deposited samples and the annealed samples, respectively.

6.4 Chapter Conclusion

In this chapter, pure strain modulation effects on the electronic structure and magnetic anisotropy of ferromagnetic films were demonstrated by depositing Fe films on non-electrically controlled NiTi(Nb) SMA substrates. The compressive strain on the film modifies the electronic structure of the inner orbits significantly by enhancing the shielding effect from outer electrons, resulting in the decrease of binding energy of Fe2p core electrons. Meanwhile, based on first principle calculation, the compressive strain tunes the DOS and spin distribution of outer d orbits, leading to the evolution of

bandwidth, SOC strength, and related magnetic anisotropy. This work helps to reveal the mechanism of pure strain-induced electronic structure tunability, but also provides a strong basis for the development of strain-assisted spintronic devices.

CHAPTER 7 – THESIS SUMMARY

7.1 Thesis Summary

In this thesis, three different investigations have been performed with the Real-time Electron Spectroscopy (REES) system. As an extremely powerful technique, the REES system is capable of monitoring electronic structure and chemical composition of the surfaces during *in situ* processing such as annealing and thin film deposition. The boron-nitride heater allows annealing the sample from RT up to 1200 K; the homemade Knudsen cell (K-cell) enables the deposition of Fe thin film with very precise control of the thickness (on the nanometer scale). The position sensitive detector (PSD) placed at the exit slit of the hemispherical electron analyser (HSA) allows the measurement of real-time XPS. In this mode, snapshots of core level spectra can be recorded every few seconds, which provides information of sample surfaces during in situ processing. The ability to alternate between conventional XPS and real-time XPS without the need to move the sample, change the electron analyser settings or x-ray gun flux was found to be extremely important in terms of reliability and confidence in the data. The fitting routine used in CasaXPS, used to fit the hundreds of snapshots collected during an annealing cycle, was fast and easy to use. Collecting ancillary data during real-time monitoring (temperatures, pressure, heater voltage and current) was extremely useful in the data analysis.

For the oxygen terminated diamond (100) surface, the near-surface properties of diamond thin films have attracted much attention due to their interaction with the optical and spin properties of nitrogen vacancy (NV) centres vital for diamond-based spintronic and quantum devices [85, 86, 88-91]. The chemical composition and electronic structure of the oxygen-terminated diamond (100) surface was investigated during the high temperature annealing process from room temperature to 1000℃ in ultra-high vacuum (UHV). The mechanism of oxygen desorption has been revealed; four different stages are observed according to the oxygen concentration on the diamond (100) surface during the heating process. Meanwhile, a specific region between 600℃ and 700℃ linked to a subsurface structure variation. Interestingly, this is the first real-time experimental result that shows the displacement of the subsurface carbon layer has a strong influence on the oxygen desorption and surface band bending during high-temperature annealing. Moreover, the activation energy for desorption of the oxygen layer on the (100) diamond surface has been estimated as ~0.5 eV. This illustrates that a surface photo-induced voltage exists on the oxygenated semiconducting surface. Meanwhile, using low-energy electron diffraction (LEED) and ultra-violet photoelectron spectroscopy (UPS), we demonstrate the surface structure was converted from the initial C(100)-(1x1):O surface to a C(100)-(2x1):H surface during the annealing process. We believe this work provides strong evidence for the oxygen desorption process from the (100) diamond surface which is pertinent for the development of spintronic and quantum engineering.

Fluorouracil (5-FU) has shown to attach to the diamond and silver surfaces but not to graphene[131]. Its interaction is strongest with silver and there is a surface termination effect with diamond. In this study, two types of termination have been used to produce the desired diamond surfaces. The oxygen-terminated (100) surface was producing by the acid etching method; the hydrogen-terminated (100) surface was prepared with an *in situ* non-thermal microwave plasma. The two types of 5-FU/diamond interface show extremely different results after deposition as shown from the XPS data (including widescans and core level scans). The 5-FU overlayer sticks on the oxygen-terminated diamond (100) but not on the hydrogen-terminated surface, which indicates there is a surface termination effect with diamond which could relate to the surface properties, such as chemical bond, electron affinity and dipole of the diamond surface. Therefore, the interaction between drug molecules and inorganic materials involved in their delivery can have a significant effect on the molecular structure.

The last investigation in this thesis is about the pure-strain effect on the electronic structure of Fe thin film. The non-electronically controlled NiTi(Nb) shape memory alloy has been employed as substrate for the Fe thin film so that a pure-strain effect can be induced on the thin films. The continuously mediated strain was transferred from the substrate to the Fe films through a thermally controlled shape memory effect. Based on the structure, the pure strain modulated electronic structure in the Fe thin films was

studied by using *in situ* x-ray photoelectron spectroscopy and first-principle calculations. The results demonstrate that the compressive strain increases the overlap of outer orbits and enhances the shielding effect on the core electrons, resulting in significant tunability of the binding energy of core electrons. Meanwhile, the lattice strain modifies the density of state and spin distribution of outer d orbitals, leading to the evolution of bandwidth, spin-orbit coupling strength, and related magnetic anisotropy. This work provided an important basis for unveiling the modulation mechanism of pure strain and developing strain-assisted spintronic devices.

7.2 Further Work

The oxygen-terminated (100) diamond surface shows some interesting results at 650℃ which could be relevant with the NV properties in near surface region of diamond. To further explain the data in this work, photoluminescence and NEXAFS measurements could be performed on this surface. Meanwhile, DFT calculation could be helpful to investigated the variation of chemical composition and spin coherence time during the annealing process.

Meanwhile, the oxygen-terminated diamond surfaces produced by different oxidising methods may vary concentration of the oxidised groups. For instance, dry oxygen etching method and non-thermal oxygen plasma could produce a surface with less step

edges on diamond[169], which may reduce the concentration of ketone groups.

DFT calculation could be performed of the diamond surfaces to study the electronic structure of the drug/diamond systems.

REFERENCES

[1] A. Zangwill, *Physics at surfaces*: Cambridge University Press, 1988.

[2] J. B. Cui, J. Ristein, and L. Ley, "Electron affinity of the bare and hydrogen covered single crystal diamond (111) surface," *Physical Review Letters,* vol. 81, p. 429, 1998.

[3] J. Shirafuji, Y. Sakamoto, A. Furukawa, H. Shigeta, and T. Sugino, "X-ray photoelectron spectroscopy analysis of plasma-treated surfaces of diamond films," *Diamond and related materials,* vol. 4, pp. 984-988, 1995.

[4] W. Steckelmacher, "Modern techniques of surface science, 2nd edition," *Vacuum,* vol. 47, p. 95, 1996/01/01 1996.

[5] H. Hertz, "Ueber einen Einfluss des ultravioletten Lichtes auf die electrische Entladung," *Annalen der Physik,* vol. 267, pp. 983-1000, 1887.

[6] A. Einstein, *The collected papers of Albert Einstein* vol. 2: Princeton University Press, 1989.

[7] J. F. Watts and J. Wolstenholme, "An introduction to surface analysis by XPS and AES," *An Introduction to Surface Analysis by XPS and AES, by John F. Watts, John Wolstenholme, pp. 224. ISBN 0-470-84713-1. Wiley-VCH, May 2003.,* p. 224, 2003.

[8] P. P. Manning, N. J. Clague, I. W. Kirkman, F. M. Quinn, and P. J. Hicks, "A fast and flexible multichannel electron detector with parallel readout for photoelectron spectroscopy," *Nuclear Instruments and Methods in Physics Research Section A: Accelerators, Spectrometers, Detectors and Associated Equipment,* vol. 392, pp. 345-348, 1997.

[9] A. Oelsner, O. Schmidt, M. Schicketanz, M. Klais, G. Schönhense, V. Mergel*, et al.*, "Microspectroscopy and imaging using a delay line detector in time-of-flight photoemission microscopy," *Review of Scientific Instruments,* vol. 72, pp. 3968-3974, 2001.

[10] L. Gori, R. Tommasini, G. Cautero, D. Giuressi, M. Barnaba, A. Accardo*, et al.*, "An embedded control and acquisition system for multichannel detectors," *Nuclear Instruments and Methods in Physics Research Section A: Accelerators,*

Spectrometers, Detectors and Associated Equipment, vol. 431, pp. 338-346, 1999.

[11] D. P. Langstaff, A. Bushell, T. Chase, and D. A. Evans, "A fully integrated multi-channel detector for electron spectroscopy," *Nuclear Instruments and Methods in Physics Research Section B: Beam Interactions with Materials and Atoms,* vol. 238, pp. 219-223, 2005.

[12] D. P. Langstaff and T. Chase, "A multichannel detector array with 768 pixels developed for electron spectroscopy," *Nuclear Instruments and Methods in Physics Research Section A: Accelerators, Spectrometers, Detectors and Associated Equipment,* vol. 573, pp. 169-171, 2007.

[13] D. P. Langstaff, D. A. Evans, O. R. Roberts, and X. Zhu, "Progress on the Aberystwyth electron counting array," *Nuclear Instruments and Methods in Physics Research Section A: Accelerators, Spectrometers, Detectors and Associated Equipment,* vol. 604, pp. 133-135, 2009.

[14] A. Evans, O. Roberts, A. Vearey-Roberts, D. Langstaff, D. Twitchen, and M. Schwitters, "Direct observation of Schottky to Ohmic transition in Al-diamond contacts using real-time photoelectron spectroscopy," 2007.

[15] D. A. Evans, O. R. Roberts, G. T. Williams, A. R. Vearey-Roberts, F. Bain, S. Evans*, et al.*, "Diamond–metal contacts: interface barriers and real-time characterization," *Journal of Physics: Condensed Matter,* vol. 21, p. 364223, 2009.

[16] S. P. Cooil, J. W. Wells, D. Hu, Y. R. Niu, A. A. Zakharov, M. Bianchi*, et al.*, "Controlling the growth of epitaxial graphene on metalized diamond (111) surface," *Applied Physics Letters,* vol. 107, p. 181603, 2015.

[17] J. Isberg, J. Hammersberg, D. J. Twitchen, and A. J. Whitehead, "Single crystal diamond for electronic applications," *Diamond and Related Materials,* vol. 13, pp. 320-324, 2004.

[18] M. D. Fries and Y. K. Vohra, "Properties of nanocrystalline diamond thin films grown by MPCVD for biomedical implant purposes," *Diamond and Related Materials,* vol. 13, pp. 1740-1743, 2004.

[19] D. P. Woodruff and T. A. Delchar, *Modern techniques of surface science*: Cambridge university press, 1994.

[20] R. Heinhold, G. T. Williams, S. P. Cooil, D. A. Evans, and M. W. Allen, "Influence of polarity and hydroxyl termination on the band bending at ZnO surfaces," *Physical Review B,* vol. 88, p. 235315, 2013.

[21] K. K. Schuegraf, *Handbook of thin-film deposition processes and techniques: principles, methods, equipment, and applications*: Noyes Data Corporation/Noyes Publications, 1988.

[22] J. A. Venables, G. D. T. Spiller, and M. Hanbucken, "Nucleation and growth of thin films," *Reports on Progress in Physics,* vol. 47, p. 399, 1984.

[23] E. Bauer, "Phänomenologische theorie der kristallabscheidung an oberflächen. II," *Zeitschrift für Kristallographie-Crystalline Materials,* vol. 110, pp. 395-431, 1958.

[24] A. V. Hamza, G. D. Kubiak, and R. H. Stulen, "Hydrogen chemisorption and the structure of the diamond C(100)-(2 × 1) surface," *Surface Science,* vol. 237, pp. 35-52, 1990.

[25] L. Diederich, O. M. Küttel, P. Aebi, and L. Schlapbach, "Electron affinity and work function of differently oriented and doped diamond surfaces determined by photoelectron spectroscopy," *Surface Science,* vol. 418, pp. 219-239, 1998.

[26] O. M. Küttel, L. Diederich, E. Schaller, O. Carnal, and L. Schlapbach, "The preparation and characterization of low surface roughness (111) and (100) natural diamonds by hydrogen plasma," *Surface science,* vol. 337, pp. L812-L818, 1995.

[27] P. S. Nandhra, R. C. Newman, R. Murray, B. Pajot, J. Chevallier, R. B. Beall*, et al.*, "The passivation of Be acceptors in GaAs by exposure to a hydrogen plasma," *Semiconductor Science and Technology,* vol. 3, p. 356, 1988.

[28] B. J. Coppa, C. C. Fulton, S. M. Kiesel, R. F. Davis, C. Pandarinath, J. E. Burnette*, et al.*, "Structural, microstructural, and electrical properties of gold films and Schottky contacts on remote plasma-cleaned, n-type ZnO {0001} surfaces," *Journal of applied physics,* vol. 97, p. 103517, 2005.

[29] R. Klauser, J.-M. Chen, T. J. Chuang, L. M. Chen, M. C. Shih, and J. C. Lin, "The interaction of oxygen and hydrogen on a diamond C (111) surface: a synchrotron radiation photoemission, LEED and AES study," *Surface science,* vol. 356, pp. L410-L416, 1996.

[30] P. Cadman, J. D. Scott, and J. M. Thomas, "Identification of functional groups on the surface of a fluorinated diamond crystal by photoelectron spectroscopy," *Journal of the Chemical Society, Chemical Communications,* pp. 654-655, 1975.

[31] A. Denisenko, A. Romanyuk, C. Pietzka, J. Scharpf, and E. Kohn, "Surface structure and surface barrier characteristics of boron-doped diamond in electrolytes after CF 4 plasma treatment in RF-barrel reactor," *Diamond and Related Materials,* vol. 19, pp. 423-427, 2010.

[32] R. S. Balmer, J. R. Brandon, S. L. Clewes, H. K. Dhillon, J. M. Dodson, I. Friel*, et al.*, "Chemical vapour deposition synthetic diamond: materials, technology and applications," *Journal of Physics: Condensed Matter,* vol. 21, p. 364221, 2009.

[33] R. F. Davis, "III-V nitrides for electronic and optoelectronic applications," *Proceedings of the IEEE,* vol. 79, pp. 702-712, 1991.

[34] A. Fridman, *Plasma chemistry*: Cambridge University Press, 2008.

[35] K. Siegbahn, *ESCA; atomic, molecular and solid state structure studied by means of electron spectroscopy* vol. 20, 1967.

[36] K. Siegbahn, "Electron spectroscopy for chemical analysis," in *Atomic Physics 3*, ed: Springer, 1973, pp. 493-522.

[37] S. Hüfner, S. Schmidt, and F. Reinert, "Photoelectron spectroscopy—An overview," *Nuclear Instruments and Methods in Physics Research Section A: Accelerators, Spectrometers, Detectors and Associated Equipment,* vol. 547, pp. 8-23, 2005.

[38] S. Hüfner, *Photoelectron spectroscopy: principles and applications*: Springer Science & Business Media, 2013.

[39] C. N. Berglund and W. E. Spicer, "Photoemission studies of copper and silver: theory," *Physical Review,* vol. 136, p. A1030, 1964.

[40] D. Coster and R. d. L. Kronig, "New type of auger effect and its influence on the x-ray spectrum," *Physica,* vol. 2, pp. 13-24, 1935.

[41] R. A. Pollak, L. Ley, F. R. McFeely, S. P. Kowalczyk, and D. A. Shirley, "Characteristic energy loss structure of solids from x-ray photoemission spectra," *Journal of Electron Spectroscopy and Related Phenomena,* vol. 3, pp. 381-398, 1974.

[42] P. Steiner, H. Höchst, and S. Hüfner, "Analysis of the plasmon structure in XPS experiments of simple metals," *Physics Letters A,* vol. 61, pp. 410-412, 1977.

[43] C. J. Powell and A. Jablonski, "NIST Electron Effective-Attenuation-Length Database,"*https://www.nist.gov/sites/default/files/documents/srd/SRD82UsersGuideV1-3.pdf,* 2002.

[44] R. Hesse, P. Streubel, and R. Szargan, "Product or sum: comparative tests of Voigt, and product or sum of Gaussian and Lorentzian functions in the fitting of synthetic Voigt-based X-ray photoelectron spectra," *Surface and Interface Analysis,* vol. 39, pp. 381-391, 2007.

[45] G. D. Mahan, "Excitons in Metals: Infinite Hole Mass," *Phys. Rev.,* vol. 163, p. 6, 1967.

[46] S. Doniach and M. Sunjic, "Many-electron singularity in X-ray photoemission and X-ray line spectra from metals," *Journal of Physics C: Solid State Physics,* vol. 3, p. 285, 1970.

[47] E. B. Saloman, J. H. Hubbell, and J. H. Scofield, "X-ray attenuation cross sections for energies 100 eV to 100 keV and elements Z = 1 to Z = 92," *Atomic Data and Nuclear Data Tables,* vol. 38, pp. 1-196, 1988.

[48] J. H. Scofield, "Hartree-Slater subshell photoionization cross-sections at 1254 and 1487 eV," *Journal of Electron Spectroscopy and Related Phenomena,* vol. 8, pp. 129-137, 1976.

[49] D. A. Evans, T. P. Chen, T. Chassé, and K. Horn, "The interaction of platinum with GaP (110): band bending and surface photovoltage effects," *Applied surface science,* vol. 56, pp. 233-241, 1992.

[50] D. A. Evans, D. Wolfframm, D. Gnoth, J. Cairns, A. C. Wright, M. Evans*, et al.*, "Metal overlayers on the MBE-grown ZnSe (001) surface," *Applied surface science,* vol. 104, pp. 240-247, 1996.

[51] D. Wolfframm, D. A. Evans, G. Neuhold, and K. Horn, "Gold and silver Schottky barriers on ZnS (110)," *Journal of Applied Physics,* vol. 87, pp. 3905-3911, 2000.

[52] J. E. Demuth, W. J. Thompson, N. J. DiNardo, and R. Imbihl, "Photoemission-based photovoltage probe of semiconductor surface and interface electronic structure," *Physical review letters,* vol. 56, p. 1408, 1986.

[53] C. Bandis and B. B. Pate, "Room temperature photovoltaic charging in photoemission from diamond," *Surface science,* vol. 345, pp. L23-L27, 1996.

[54] J. P. Long and V. M. Bermudez, "Band bending and photoemission-induced surface photovoltages on clean n-and p-GaN (0001) surfaces," *Physical Review B,* vol. 66, p. 121308, 2002.

[55] S. Foner, "The vibrating sample magnetometer: Experiences of a volunteer (invited)," *Journal of Applied Physics,* vol. 79, pp. 4740-4745, 1996.

[56] Q. Design, "Physical Property Measurement System," http://www.qdusa.com/products/ppms.html.

[57] J. Stöhr, *NEXAFS spectroscopy* vol. 25: Springer Science & Business Media, 2013.

[58] S. P. Cooil, "Controlling the epitaxial growth of graphene on diamond surfaces," PhD thesis, Aberystwyth University, 2013.

[59] H. Lüth, "Solid surfaces, interfaces and thin films," *Springer London, Limited,* 2010.

[60] D. M. S. Hoffman, Bawa; Thomas, John H., "Handbook of vacuum science and technology," *Elsevier Science,* 1998.

[61] M. P. Seah and W. A. Dench, "Quantitative electron spectroscopy of surfaces: A standard data base for electron inelastic mean free paths in solids," *Surface and Interface Analysis,* vol. 1, pp. 2-11, 1979.

[62] A. Rousse, K. T. Phuoc, R. Shah, A. Pukhov, E. Lefebvre, V. Malka*, et al.*, "Production of a keV X-Ray Beam from Synchrotron Radiation in Relativistic Laser-Plasma Interaction," *Physical Review Letters,* vol. 93, p. 135005, 2004.

[63] B. Bowers, "X-rays: their discovery and applications," *Her Majesty's Stationery Office,* 1970.

[64] M. O. Krause and J. G. Ferreira, "K X-ray emission spectra of Mg and Al," *Journal of Physics B: Atomic and Molecular Physics,* vol. 8, p. 2007, 1975.

[65] S. Narioka, H. Ishii, D. Yoshimura, M. Sei, Y. Ouchi, K. Seki*, et al.*, "The electronic structure and energy level alignment of porphyrin/metal interfaces studied by ultraviolet photoelectron spectroscopy," *Applied Physics Letters,* vol. 67, pp.

1899-1901, 1995.

[66] SPECS, "Ultraviolet Source UVS 300," *Available from:* http://www.specs.de/cms/front_content.php?idcat=121, 2013.

[67] J. L. Vossen and W. Kern, *Thin film processes*: Academic Press, 1978.

[68] J. C. Swarbrick, J. B. Taylor, and J. N. O'Shea, "Electrospray deposition in vacuum," *Applied Surface Science,* vol. 252, pp. 5622-5626, 2006.

[69] D. M. Mattox, *Handbook of physical vapor deposition (PVD) processing : film formation, adhesion, surface preparation and contamination control*: Noyes Publications, 1998.

[70] S. R. Forrest, "Ultrathin Organic Films Grown by Organic Molecular Beam Deposition and Related Techniques," *Chemical Reviews,* vol. 97, pp. 1793-1896, 1997.

[71] J. D. Rancourt, *Optical thin films : user handbook*: SPIE Optical Engineering Press, 1996.

[72] S. Evans and J. M. Thomas, "The Chemical Nature of Ion-Bombarded Carbon: A Photoelectron Spectroscopic Study of "Cleaned" Surfaces of Diamond and Graphite," *Proceedings of the Royal Society of London. A. Mathematical and Physical Sciences,* vol. 353, pp. 103-120, 1977.

[73] D. Roy and D. Tremblay, "Design of electron spectrometers," *Reports on Progress in Physics,* vol. 53, p. 1621, 1990.

[74] S. D. Kevan, "Design of a high‐resolution angle‐resolving electron energy analyzer," *Review of Scientific Instruments,* vol. 54, pp. 1441-1445, 1983.

[75] SPECS, "Extended Range Channel Electron Multiplier (CEM)." *Available from:* http://www.specs.de/cms/front_content.php?idcat=181.

[76] J. R. Lee and W. Ho, "Position‐sensitive detector performance and relevance to time‐resolved electron energy loss spectroscopy," *Review of Scientific Instruments,* vol. 57, pp. 1469-1482, 1986.

[77] J. Ladislas Wiza, "Microchannel plate detectors," *Nuclear Instruments and Methods,* vol. 162, pp. 587-601, 1979.

[78] X. Zhu and D. P. Langstaff, "Reduction of multiple triggering in counting detectors," *Nuclear Instruments and Methods in Physics Research Section A: Accelerators, Spectrometers, Detectors and Associated Equipment,* vol. 604, pp. 400-403, 2009.

[79] C. A. Fairley, N. Fairly, " The casa cookbook." *Cheshire, UK: Acolyte science, 2005.*

[80] A. Härtl, E. Schmich, J. A. Garrido, J. Hernando, S. C. R. Catharino, S. Walter*, et al.*, "Protein-modified nanocrystalline diamond thin films for biosensor applications," *Nature materials,* vol. 3, pp. 736-742, 2004.

[81] C. Stampfer, E. Schurtenberger, F. Molitor, J. Guttinger, T. Ihn, and K. Ensslin, "Tunable graphene single electron transistor," *Nano letters,* vol. 8, pp. 2378-2383, 2008.

[82] A. Aleksov, M. Kubovic, N. Kaeb, U. Spitzberg, A. Bergmaier, G. Dollinger*, et al.*, "Diamond field effect transistors—concepts and challenges," *Diamond and Related Materials,* vol. 12, pp. 391-398, 2003.

[83] T. Ergin, N. Stenger, P. Brenner, J. B. Pendry, and M. Wegener, "Three-dimensional invisibility cloak at optical wavelengths," *Science,* vol. 328, pp. 337-339, 2010.

[84] T. Strother, T. Knickerbocker, J. N. Russell, J. E. Butler, L. M. Smith, and R. J. Hamers, "Photochemical functionalization of diamond films," *Langmuir,* vol. 18, pp. 968-971, 2002.

[85] R. Hanson and D. D. Awschalom, "Coherent manipulation of single spins in semiconductors," *Nature,* vol. 453, pp. 1043-1049, 2008.

[86] F. Jelezko and J. Wrachtrup, "Single defect centres in diamond: A review," *physica status solidi (a),* vol. 203, pp. 3207-3225, 2006.

[87] G. Balasubramanian, I. Y. Chan, R. Kolesov, M. Al-Hmoud, J. Tisler, C. Shin*, et al.*, "Nanoscale imaging magnetometry with diamond spins under ambient conditions," *Nature,* vol. 455, pp. 648-651, 2008.

[88] H. J. Mamin, M. Kim, M. H. Sherwood, C. T. Rettner, K. Ohno, D. D. Awschalom*, et al.*, "Nanoscale nuclear magnetic resonance with a nitrogen-vacancy spin sensor," *Science,* vol. 339, pp. 557-560, 2013.

[89] F. Dolde, H. Fedder, M. W. Doherty, T. Nöbauer, F. Rempp, G. Balasubramanian*, et*

al., "Electric-field sensing using single diamond spins," *Nature Physics,* vol. 7, pp. 459-463, 2011.

[90] L. Childress and R. Hanson, "Diamond NV centers for quantum computing and quantum networks," *MRS bulletin,* vol. 38, pp. 134-138, 2013.

[91] J. Wrachtrup and F. Jelezko, "Processing quantum information in diamond," *Journal of Physics: Condensed Matter,* vol. 18, p. S807, 2006.

[92] K. M. Fu, C. Santori, P. E. Barclay, and R. G. Beausoleil, "Conversion of neutral nitrogen-vacancy centers to negatively charged nitrogen-vacancy centers through selective oxidation," *Applied Physics Letters,* vol. 96, p. 121907, 2010.

[93] S. P. Cooil, F. Song, G. T. Williams, O. R. Roberts, D. P. Langstaff, B. Jørgensen*, et al.*, "Iron-mediated growth of epitaxial graphene on SiC and diamond," *Carbon,* vol. 50, pp. 5099-5105, 2012.

[94] J. Ristein, "Electronic properties of diamond surfaces—blessing or curse for devices?," *Diamond and Related Materials,* vol. 9, pp. 1129-1137, 2000.

[95] C. E. Nebel and J. Ristein, *Thin-film diamond* vol. v. 76, 77: Elsevier Academic Press, 2003.

[96] C. Y. Fong and B. M. Klein, "Electronic and Vibrational Properties of Bulk Diamond", *Diamond: Electronic Properties and Applications*, L. S. Pan and D. R. Kania, Eds., ed Boston, MA: Springer US, 1995, pp. 1-29.

[97] T. M. M. J.M. King, J.E. Shigley, Y. Liu, "Color Grading of Colored Diamonds in the GIA Gem Trade Laboratory.," *Gems & Gemology, Volume: 30 Issue: 4 pp 220 - 242.,* 1994.

[98] R. Robertson, J. J. Fox, and A. E. Martin, "Two Types of Diamond," *Philosophical Transactions of the Royal Society of London. Series A, Containing Papers of a Mathematical or Physical Character,* vol. 232, pp. 463-535, 1934.

[99] J. F. H. Custers, "Unusual phosphorescence of a diamond," *Physica,* vol. 18, pp. 489-496, 1952.

[100] F. P. Bundy, H. T. Hall, H. M. Strong, and R. H. Wentorf, "Man-Made Diamonds," *Nature,* vol. 176, pp. 51-55, 1955.

[101] J. E. a. D. G. G. Butler, "CVD growth of diamond, in Properties, growth and applications of diamond.," *Short run press: Exeter, UK.,* 2000.

[102] A. Kawano, H. Ishiwata, S. Iriyama, R. Okada, S. Kitagoh, M. Watanabe*, et al.*, "Critical concentrations of superconductor to insulator transition in (1 1 1) and (0 0 1) CVD boron-doped diamond," *Physica C: Superconductivity and its Applications,* vol. 470, Supplement 1, pp. S604-S607, 2010.

[103] N. Tokuda, T. Saito, H. Umezawa, H. Okushi, and S. Yamasaki, "The role of boron atoms in heavily boron-doped semiconducting homoepitaxial diamond growth — Study of surface morphology," *Diamond and Related Materials,* vol. 16, pp. 409-411, 2007.

[104] J. P. Lagrange, A. Deneuville, and E. Gheeraert, "Activation energy in low compensated homoepitaxial boron-doped diamond films," *Diamond and Related Materials,* vol. 7, pp. 1390-1393, 1998.

[105] G. Kern, J. Hafner, and G. Kresse, "Atomic and electronic structure of diamond (111) surfaces I. Reconstruction and hydrogen-induced de-reconstruction of the one dangling-bond surface," *Surface Science,* vol. 366, pp. 445-463, 1996.

[106] M. N. R. Ashfold, P. W. May, C. A. Rego, and N. M. Everitt, "Thin film diamond by chemical vapour deposition methods," *Chemical Society Reviews,* vol. 23, pp. 21-30, 1994.

[107] R. Graupner, M. Hollering, A. Ziegler, J. Ristein, L. Ley, and A. Stampfl, "Dispersions of surface states on diamond (100) and (111)," *Physical Review B,* vol. 55, p. 10841, 1997.

[108] F. Maier, J. Ristein, and L. Ley, "Electron affinity of plasma-hydrogenated and chemically oxidized diamond (100) surfaces," *Physical Review B,* vol. 64, p. 165411, 2001.

[109] M. Wang, N. Simon, C. Decorse-Pascanut, M. Bouttemy, A. Etcheberry, M. Li*, et al.*, "Comparison of the chemical composition of boron-doped diamond surfaces upon different oxidation processes," *Electrochimica Acta,* vol. 54, pp. 5818-5824, 2009.

[110] L. A. Hutton, J. G. Iacobini, E. Bitziou, R. B. Channon, M. E. Newton, and J. V. Macpherson, "Examination of the factors affecting the electrochemical performance of oxygen-terminated polycrystalline boron-doped diamond

electrodes," *Anal Chem,* vol. 85, pp. 7230-40, 2013.

[111] M. D. Hanwell, D. E. Curtis, D. C. Lonie, T. Vandermeersch, E. Zurek, and G. R. Hutchison, "Avogadro: an advanced semantic chemical editor, visualization, and analysis platform," *Journal of Cheminformatics,* vol. 4, p. 17, 2012.

[112] S. J. Sque, R. Jones, and P. R. Briddon, "Structure, electronics, and interaction of hydrogen and oxygen on diamond surfaces," *Physical Review B,* vol. 73, 2006.

[113] C. Bandis and B. B. Pate, "Electron Emission Due to Exciton Breakup from Negative Electron Affinity Diamond," *Physical Review Letters,* vol. 74, pp. 777-780, 1995.

[114] R. Graupner, F. Maier, J. Ristein, L. Ley, and C. Jung, "High-resolution surface-sensitive C 1 s core-level spectra of clean and hydrogen-terminated diamond (100) and (111) surfaces," *Physical Review B,* vol. 57, p. 12397, 1998.

[115] H. Girard, N. Simon, D. Ballutaud, M. Herlem, and A. Etcheberry, "Effect of anodic and cathodic treatments on the charge transfer of boron doped diamond electrodes," *Diamond and related materials,* vol. 16, pp. 316-325, 2007.

[116] H. Notsu, I. Yagi, T. Tatsuma, D. A. Tryk, and A. Fujishima, "Surface carbonyl groups on oxidized diamond electrodes," *Journal of Electroanalytical Chemistry,* vol. 492, pp. 31-37, 2000.

[117] F. Klauser, S. Ghodbane, R. Boukherroub, S. Szunerits, D. Steinmüller-Nethl, E. Bertel*, et al.*, "Comparison of different oxidation techniques on single-crystal and nanocrystalline diamond surfaces," *Diamond and Related Materials,* vol. 19, pp. 474-478, 2010.

[118] S. Ghodbane, D. Ballutaud, F. Omnès, and C. Agnès, "Comparison of the XPS spectra from homoepitaxial {111}, {100} and polycrystalline boron-doped diamond films," *Diamond and Related Materials,* vol. 19, pp. 630-636, 2010.

[119] K. P. Loh, X. N. Xie, S. W. Yang, and J. C. Zheng, "Oxygen adsorption on (111)-oriented diamond: a study with ultraviolet photoelectron spectroscopy, temperature-programmed desorption, and periodic density functional theory," *The Journal of Physical Chemistry B,* vol. 106, pp. 5230-5240, 2002.

[120] J. Robertson and M. J. Rutter, "Band diagram of diamond and diamond-like carbon surfaces," *Diamond and related materials,* vol. 7, pp. 620-625, 1998.

[121] M. H. Hecht, "Photovoltaic effects in photoemission studies of Schottky barrier formation," *Journal of Vacuum Science & Technology B,* vol. 8, pp. 1018-1024, 1990.

[122] G. T. Williams, S. P. Cooil, O. R. Roberts, S. Evans, D. P. Langstaff, and D. A. Evans, "High temperature photoelectron emission and surface photovoltage in semiconducting diamond," *Applied Physics Letters,* vol. 105, p. 061602, 2014.

[123] V. L. Kuznetsov, I. L. Zilberberg, Y. V. Butenko, A. L. Chuvilin, and B. Segall, "Theoretical study of the formation of closed curved graphite-like structures during annealing of diamond surface," *Journal of applied physics,* vol. 86, pp. 863-870, 1999.

[124] A. Sistigu, T. Yamazaki, E. Vacchelli, K. Chaba, D. P. Enot, J. Adam*, et al.*, "Cancer cell-autonomous contribution of type I interferon signaling to the efficacy of chemotherapy," *Nature medicine,* vol. 20, pp. 1301-1309, 2014.

[125] Lu, Z, Zhang, R, Diasio, and B. R, "Dihydropyrimidine dehydrogenase activity in human peripheral blood mononuclear cells and liver : population characteristics, newly identified deficient patients, and clinical implication in 5-fluorouracil chemotherapy", *Cancer Res,* vol. 53, 1993.

[126] D. B. Longley, D. P. Harkin, and P. G. Johnston, "5-Fluorouracil: mechanisms of action and clinical strategies," *Nat Rev Cancer,* vol. 3, pp. 330-338, 05//print 2003.

[127] B. A. O'leary R, " Future directions for ultrasound-guided central venous access[J]." *European Journal of Anaesthesiology (EJA).* vol. 2011, 28(5): 327-328., 2011.

[128] Ardalan, B, Flores, and R. M, "A new complication of chemotherapy administered via permanent indwelling central venous catheter"*, Cancer,* vol. 75, 1995.

[129] J.-F. Timsit, Y. Dubois, C. Minet, A. Bonadona, M. Lugosi, C. Ara-Somohano*,* R. Hamidfar-Roy, and C. Shcwebel, "New materials and devices for preventing catheter-related infections," *Annals of intensive care,* vol. 1, p. 34, 2011.

[130] I. Armentano, C. R. Arciola, E. Fortunati, D. Ferrari, S. Mattioli, C. F. Amoroso*,* J. Rizzo, J. M. Kenny, M. Imbriani, and L. Visai., "The Interaction of Bacteria with Engineered Nanostructured Polymeric Materials: A Review," *The Scientific World Journal,* vol. 2014, p. 410423, 2015

[131] F. Mazzola, T. Trinh, S. Cooil, E. R. Østli, K. Høydalsvik, E. T. B. Skjønsfjell*, et al.*, "Graphene coatings for chemotherapy: avoiding silver-mediated degradation," *2D Materials,* vol. 2, p. 025004, 2015.

[132] G. Dearnaley and J. H. Arps, "Biomedical applications of diamond-like carbon (DLC) coatings: A review," *Surface and Coatings Technology,* vol. 200, pp. 2518-2524, 2005.

[133] T. Hallam, M. J. Butcher, K. E. J. Goh, F. J. Ruess, and M. Y. Simmons, "Use of a scanning electron microscope to pattern large areas of a hydrogen resist for electrical contacts," *Journal of Applied Physics,* vol. 102, p. 034308, 2007.

[134] J. Li, Z. Shan, and E. Ma, "Elastic strain engineering for unprecedented materials properties," *MRS Bulletin,* vol. 39, pp. 108-114, 2014.

[135] J. Feng, X. Qian, C.-W. Huang, and J. Li, "Strain-engineered artificial atom as a broad-spectrum solar energy funnel," *Nat Photon,* vol. 6, pp. 866-872, 2012.

[136] M. Weisheit, S. Fähler, A. Marty, Y. Souche, C. Poinsignon, and D. Givord, "Electric Field-Induced Modification of Magnetism in Thin-Film Ferromagnets," *Science,* vol. 315, pp. 349-351, 2007.

[137] L. H. Diez, A. Bernand-Mantel, O. Michele, L. Vila, P. Warin, A. Marty, L. Ranno, and D.Givord, "Electric-field effect on coercivity distributions in FePt magneto-electric devices," *Applied Physics Letters,* vol. 102, p. 012409, 2013.

[138] S. Takeshi, K. Makoto, N. Junsaku, and T. Koki, "Coercivity change in an FePt thin layer in a Hall device by voltage application," *Applied Physics Letters,* vol. 98, p. 212505, 2011.

[139] S. Zhang, Y. G. Zhao, P. S. Li, J. J. Yang, S. Rizwan, J. X. Zhang*, et al.*, "Electric-Field Control of Nonvolatile Magnetization in Co_{40} $Fe_{40}B_{20}$/$Pb(Mg1/3Nb2/3)_{0.7}Ti_{0.3}O_3$ Structure at Room Temperature," *Physical Review Letters,* vol. 108, p. 137203, 2012.

[140] T. Nan, Z. Zhou, M. Liu, X. Yang, Y. Gao, B. A. Assaf*, et al.*, "Quantification of strain and charge co-mediated magnetoelectric coupling on ultra-thin Permalloy/PMN-PT interface," *Scientific Reports,* vol. 4, p. 3688, 2014.

[141] Y.-Y. Zhao, J. Wang, H. Kuang, F.-X. Hu, Y. Liu, R.-R. Wu*, et al.*, "Anisotropic

modulation of magnetic properties and the memory effect in a wide-band (011)-Pr0.7Sr0.3MnO3/PMN-PT heterostructure," *Scientific Reports,* vol. 5, p. 9668, 2015.

[142] C. Feng, J. Zhao, F. Yang, K. Gong, S. Hao, Y. Cao*, et al.*, "Corrigendum: Nonvolatile modulation of electronic structure and correlative magnetism of L10-FePt films using significant strain induced by shape memory substrates," *Scientific Reports,* vol. 6, p. 23878, 2016.

[143] A. Mardana, S. Ducharme, and S. Adenwalla, "Ferroelectric Control of Magnetic Anisotropy," *Nano Letters,* vol. 11, pp. 3862-3867, 2011.

[144] Y. Zhou, Z. Wang, P. Yang, X. Zu, L. Yang, X. Sun*, et al.*, "Tensile Strain Switched Ferromagnetism in Layered NbS2 and NbSe2," *ACS Nano,* vol. 6, pp. 9727-9736, 2012.

[145] L. M. Loong, X. Qiu, Z. P. Neo, P. Deorani, Y. Wu, C. S. Bhatia*, et al.*, "Strain-enhanced tunneling magnetoresistance in MgO magnetic tunnel junctions," *Scientific Reports,* vol. 4, p. 6505, 2014.

[146] T. Alexander, K. Andreas, B. Felix, J. Gerhard, E. Stefan, and K. Mathias, "Electric field modification of magnetotransport in Ni thin films on (011) PMN-PT piezosubstrates," *Applied Physics Letters,* vol. 106, p. 062404, 2015.

[147] M. S. Ajeesh, K. T. Ravi, K. Gopinadhan, S. B. Charanjit, S. Mark, and Y. Hyunsoo, "Biaxial strain effect of spin dependent tunneling in MgO magnetic tunnel junctions," *Applied Physics Letters,* vol. 101, p. 042407, 2012.

[148] H. Xin, G. Li, T. Ning, D. Junxi, X. Fujun, W. Xinqiang*, et al.*, "Shear strain induced modulation to the transport properties of graphene," *Applied Physics Letters,* vol. 105, p. 083108, 2014.

[149] J. Changjun, Z. Chao, D. Chunhui, G. Dangwei, and X. Desheng, "Electric field tuning of non-volatile three-state magnetoelectric memory in FeCo-NiFe2O4/Pb(Mg1/3Nb2/3)0.7Ti0.3O3 heterostructures," *Applied Physics Letters,* vol. 106, p. 122406, 2015.

[150] J. S. Chen, B. C. Lim, Y. F. Ding, and G. M. Chow, "Low-temperature deposition of L10 FePt films for ultra-high density magnetic recording," *Journal of Magnetism and Magnetic Materials,* vol. 303, pp. 309-317, 2006.

[151] R. S. Jacobsen, K. N. Andersen, P. I. Borel, J. Fage-Pedersen, L. H. Frandsen, O. Hansen*, et al.*, "Strained silicon as a new electro-optic material", *Nature,* vol. 441, pp. 199-202, 2006.

[152] R. J. Zeches, M. D. Rossell, J. X. Zhang, A. J. Hatt, Q. He, C. H. Yang*, et al.*, "A Strain-Driven Morphotropic Phase Boundary in $BiFeO_3$", *Science,* vol. 326, pp. 977-980, 2009.

[153] T. Zhenhua, W. Baomin, Y. Huali, X. Xinyu, L. Yiwei, S. Dandan*, et al.*, "Magneto-mechanical coupling effect in amorphous Co40Fe40B20 films grown on flexible substrates," *Applied Physics Letters,* vol. 105, p. 103504, 2014.

[154] D. Guohong, Z. Qingfeng, L. Yiwei, Y. Huali, Z. Xiaoshan, C. Bin*, et al.*, "Mechanically tunable magnetic properties of Fe81Ga19 films grown on flexible substrates," *Applied Physics Letters,* vol. 100, p. 122407, 2012.

[155] C. Feng, J. Zhao, F. Yang, S. Hao, K. Gong, D. Hu*, et al.*, "Reversible and Nonvolatile Modulations of Magnetization Switching Characteristic and Domain Configuration in L10-FePt Films via Nonelectrically Controlled Strain Engineering," *ACS Applied Materials & Interfaces,* vol. 8, pp. 7545-7552, 2016.

[156] N. Nagaosa, J. Sinova, S. Onoda, A. H. MacDonald, and N. P. Ong, "Anomalous Hall effect," *Reviews of Modern Physics,* vol. 82, pp. 1539-1592, 2010.

[157] S. Li, L. Zheng, M. Jing, G. Ya, G. Lin, S. Yang*, et al.*, "Thickness-dependent voltage-modulated magnetism in multiferroic heterostructures," *Applied Physics Letters,* vol. 100, p. 022405, 2012.

[158] K. Otsuka, "Physical metallurgy of Ti-Ni-based shape memory alloys," *Prog. Mater. Sci.,* vol. 50, pp. 511-678, 2005 2005.

[159] S. Hao, L. Cui, D. Jiang, X. Han, Y. Ren, J. Jiang*, et al.*, "A Transforming Metal Nanocomposite with Large Elastic Strain, Low Modulus, and High Strength," *Science,* vol. 339, pp. 1191-1194, 2013.

[160] X. Qiu, K. Narayanapillai, Y. Wu, P. Deorani, D.-H. Yang, W.-S. Noh*, et al.*, "Spin–orbit-torque engineering via oxygen manipulation," *Nat Nano,* vol. 10, pp. 333-338, 2015.

[161] Seemann, M. K, Mokrousov, Y, Aziz, A*, et al.*, "Spin-Orbit Strength Driven Crossover between Intrinsic and Extrinsic Mechanisms of the Anomalous Hall

Effect in the Epitaxial L1[0]-Ordered Ferromagnets FePd and FePt," Physical Review Letters, vol. 104, 2010.

[162] X. Fan, J. Wu, Y. Chen, M. J. Jerry, H. Zhang, and J. Q. Xiao, "Observation of the nonlocal spin-orbital effective field," *Nature Communications,* vol. 4, p. 1799, 2013.

[163] T. Jungwirth, J. Wunderlich, and K. Olejnik, "Spin Hall effect devices," *Nat Mater,* vol. 11, pp. 382-390, 2012.

[164] S. Tanuma, C. J. Powell, and D. R. Penn, "Calculations of electron inelastic mean free paths for 31 materials," *Surface and Interface Analysis,* vol. 11, pp. 577-589, 1988.

[165] Kresse, G, Hafner, and J, "Ab initio molecular dynamics for liquid metal.", Physical Review B, vol. 47, 1993.

[166] Blochl and E. P, "Projector augmented-wave method," Physical Review B, vol. 50, 1994.

[167] Perdew, P. J, Burke, K, Ernzerhof, and M, "Generalized gradient approximation made simple," Physical Review Letters, vol. 77, 1996.

[168] S. Ben‐Menahem, "The Thomas precession and velocity‐space curvature," *Journal of Mathematical Physics,* vol. 27, pp. 1284-1286, 1986.

[169] F. De Theije, O. Roy, N. Van der Laag, and W. Van Enckevort, "Oxidative etching of diamond," *Diamond and Related Materials,* vol. 9, pp. 929-934, 2000.